

UNIVERSITY OF SOUTHAMPTON

NATIONAL OCEANOGRAPHY CENTRE

Diabatic eddies in idealised channel models

THESIS FOR THE DEGREE OF DOCTOR OF PHILOSOPHY

Author:

Helen Burns

Supervisors:

Sybren Drijfhout and
Alberto Naveira Garabato

23rd July 2017

ABSTRACT

UNIVERSITY OF SOUTHAMPTON

FACULTY OF NATURAL AND ENVIRONMENTAL SCIENCES

NATIONAL OCEANOGRAPHY CENTRE

DOCTOR OF PHILOSOPHY

Diabatic eddies in idealised channel models

by Helen Burns

ACKNOWLEDGEMENTS

Academic Thesis: Declaration Of Authorship

I, Helen Burns, declare that this thesis and the work presented in it are my own and has been generated by me as the result of my own original research.

I confirm that:

1. This work was done wholly or mainly while in candidature for a research degree at this University;
2. Where any part of this thesis has previously been submitted for a degree or any other qualification at this University or any other institution, this has been clearly stated;
3. Where I have consulted the published work of others, this is always clearly attributed;
4. Where I have quoted from the work of others, the source is always given. With the exception of such quotations, this thesis is entirely my own work;
5. I have acknowledged all main sources of help;
6. Where the thesis is based on work done by myself jointly with others, I have made clear exactly what was done by others and what I have contributed myself;
7. Either none of this work has been published before submission, or parts of this work have been published as:

Signed: _____

Date: _____

Contents

| | |
|--|-----|
| Abstract | i |
| Acknowledgements | ii |
| Declaration of authorship | iii |
| Contents | iv |
| List of Tables | vii |
| List of Figures | vii |
| 1 Introduction | 1 |
| 1.1 Introduction to Southern Ocean dynamics | 2 |
| 1.1.1 Eddies in the the Southern Ocean | 3 |
| 1.1.2 Meridional Overturning Circulation | 4 |
| 1.1.3 ACC | 5 |
| 1.1.4 Eddy saturation. | 6 |
| 1.2 Residual Mean and Transformed Eulerian Mean Theory | 7 |
| 1.2.1 Assumptions and approximations: | 7 |
| 1.2.2 Eliassen-Palm theorem | 10 |
| 1.2.3 Transformed Eulerian Mean theory | 11 |
| 1.3 TEM in The Surface Layers | 16 |
| 1.4 Motivation | 17 |
| 1.5 Outline of model | 18 |
| 1.5.1 MITgcm overview | 18 |
| 1.5.2 Considering model set up | 20 |
| 1.6 Channel model set up | 28 |
| 2 Diabatic eddies | 33 |
| 2.1 Introduction | 33 |
| 2.2 Theory | 35 |
| 2.3 Model Setup | 41 |
| 2.4 Overturning response | 43 |

| | | |
|--------------------|---|------------|
| 2.5 | Heat budget | 48 |
| 2.6 | Controls on diabatic eddies | 54 |
| 2.7 | Conclusions | 57 |
| 3 | Surface Conditions | 61 |
| 3.1 | The influence of the surface forcing formulation. | 61 |
| 3.1.1 | Set up | 62 |
| 3.1.2 | Influence on overturning and diabatic eddies | 63 |
| 3.1.3 | Summary | 68 |
| 3.2 | Varying the surface forcing | 69 |
| 3.2.1 | Model set up | 71 |
| 3.2.2 | Overturning | 74 |
| 3.2.3 | Conclusions on varying the surface boundary condition | 90 |
| 4 | Northern stratification | 95 |
| 4.0.1 | Set up | 96 |
| 4.0.2 | Preliminary experiments | 98 |
| 4.0.3 | Direct alteration of northern boundary stratification | 101 |
| 4.0.4 | Overturning response | 102 |
| 4.0.5 | Energetics | 113 |
| 4.0.6 | Conclusions altered boundary conditions | 115 |
| 5 | Other Considerations | 117 |
| 5.1 | Including topography | 117 |
| 5.1.1 | Set up | 118 |
| 5.1.2 | Overturning | 120 |
| 5.1.3 | Dynamics | 124 |
| 5.2 | ACC | 128 |
| 5.2.1 | The ACC response to altered northern boundary conditions | 129 |
| 6 | Discussion | 133 |
| 6.0.1 | Closing the Northern Boundary | 133 |
| 6.1 | The Surface Heat Forcing | 136 |
| 6.2 | Effects of Topography | 138 |
| 6.3 | Summary and Future Work | 138 |
| Acronyms | | 145 |
| Symbolslist | | 149 |
| Glossary | | 151 |

| | |
|-------------------------------|------------|
| Bibliography | 153 |
|-------------------------------|------------|

| | |
|-----------------------------|------------|
| Appendices | 161 |
|-----------------------------|------------|

| | |
|---|-----|
| A Advective assumptions on model grid | 163 |
| B Eaxmple datafile | 165 |

List of Tables

| | | |
|-----|--|-----|
| 2.1 | Model Setup for flat bottom fixed-surface flux experiments | 42 |
| 3.1 | Model Setup parameters for the flat bottom surface restoring experiments | 71 |
| 3.2 | Outline of runs with differing surface forcing. | 74 |
| 5.1 | Model Setup for fixed-flux runs with topography. | 119 |

List of Figures

| | | |
|-----|---|----|
| 1.1 | Southern Ocean’s role in the global overturning schematic from <i>Marshall and Speer</i> (2012), with blues and purples representing denser water masses and reds and yellows less dense water masses. | 1 |
| 1.2 | Southern Ocean circulation schematic from <i>Speer et al.</i> (2000). Showing the main water masses and overturning circulations with the buoyancy forcing. Acronyms are defined in the glossary section for reference. | 4 |
| 1.3 | Southern Ocean Overturning Circulation directed along isopycnals related to surface forcing and outside diabatic processes. Adapted from <i>Marshall and Radko</i> (2003) schematic. | 18 |
| 1.4 | A illustration of the horizontal and vertical grid spacing. a) Arakawa C grid and b) Lorenz vertical grid. <i>Adapted from</i> (<i>Collins et al.</i> , 2013) | 20 |
| 1.5 | a) Taken from <i>Abernathay et al.</i> (2011) the net surface wind from CORE 2 (<i>Large and Yeager</i> , 2009). b) A simplified version of the observed surface wind stress used in our model. | 29 |

| | |
|---|----|
| 1.6 a) Taken from <i>Cerovečki et al.</i> (2011) the net surface heat flux from various estimates b) A simplified version of the LY09 line (<i>Large and Yeager</i> , 2009) to force our model in a simple cooling, heating, cooling pattern. | 30 |
| 2.1 An illustration of the channel model configuration, showing the surface forcing and the sponge layer at the northern boundary, with the expected residual circulation from the surface forcing at short sponge relaxation time scales depicted. The SO ROC in coloured arrows is determined in the surface mixed layer, which in this configuration can be several hundred meters deep, and directed along mean isopycnals in the interior. | 34 |
| 2.2 Mean isotherms in a hypothetical mixed layer (grey) showing a) assumed no vertical temperature gradient with purely horizontal diabatic fluxes and b) assumes isotherms are not vertical and an artificial thin layer where there is no along isothermal flow. adapted from <i>Plumb and Ferrari</i> (2005) | 39 |
| 2.3 The Eulerian mean streamfunction ($\bar{\Psi}$), calculated from 100 years averaged velocities. | 43 |
| 2.4 The isothermal stream function $\Psi_{res}(y, \theta)$ remapped onto depth coordinates, to give $\Psi_{res}(y, z)$ for a) $\tau_R = 3$ day and b) no relaxation. Isotherms in multiples of 1°C are overlaid as solid black contours. The surface heat forcing is displayed above. | 45 |
| 2.5 The isothermal stream function $\Psi_{res}(y, T)$ for a) $\tau_R = 3$ day and b) no relaxation. | 46 |
| 2.6 The isothermal stream function $\Psi_{res}(y, \theta)$ remapped onto depth coordinates, to give $\Psi_{res}(y, z)$ for a sponge layer relaxing to the closed boundary profile with a relaxation time scales of 300 days. Isotherms in multiples of 1°C are overlaid as solid black contours. | 47 |
| 2.7 The components of the full depth buoyancy budget evaluated in as in Eq. 2.5. The advective transport component is show in black and diapycnal transport in blue, surface heat forcing in red and the total in thin black line. | 49 |
| 2.8 Zonal mean diapycnal heat divergence for relaxation timescale 3, 300, 3000 days and no relaxation. | 51 |
| 2.9 Zonal mean Adiabatic heat divergence for relaxation timescale 3, 300, 3000 days and no relaxation. | 53 |

| | |
|--|----|
| 2.10 EKE $\frac{1}{2}(u^2 + v^2)$ for relaxation time scales of 3, 300, 3000 days and no relaxation. Isotherms in multiples of 1°C are overlaid as solid black contours. The light grey contour indicates the mixed layer depth. Above the surface heat forcing is displayed. | 55 |
| 2.11 EPE = $g'T'^2dT^*/dz$ for relaxation time scales of 3 days and no relaxation. Isotherms in multiples of 1°C are overlaid as solid black contours. Above the surface heat forcing is displayed. | 56 |
| 2.12 Change in kinetic energy | 56 |
| (a) EKE | 56 |
| (b) KE | 56 |
| 3.1 The isothermal stream function $\Psi_{res}(y, \theta)$ remapped onto depth coordinates, to give $\Psi_{res}(y, z)$. Isotherms in multiples of 1°C are overlaid as solid black contours. | 64 |
| 3.2 The isothermal stream function $\Psi_{res}(y, \theta)$ remapped onto depth coordinates, to give $\Psi_{res}(y, z)$. Isotherms in multiples of 1°C are overlaid as solid black contours. | 65 |
| 3.3 Zonal mean diapycnal heat divergence for varying surface forcing in flat bottom closed northern boundary runs. a) Surface restoring from AC14, b) Equivalent heat fluxes, c) Original heat fluxes. | 67 |
| 3.4 The isothermal stream function $\Psi_{res}(y, \theta)$ remapped onto depth coordinates, to give $\Psi_{res}(y, z)$ for a-b) $\tau_R = 3$ day and c-d) no relaxation. Isotherms in multiples of 1°C are overlaid as solid black contours. Note: AC14 runs b and d have rescaled colour bars to account for weaker circulation | 70 |
| 3.5 The surface temperature restoration profile calculated from eq. 3.3. Varying λ from 1 month to 6 months (30 - 300 days) | 73 |
| 3.6 The isothermal stream function $\Psi_{res}(y, T)$ for a) $\tau_R = 3$ day and b) no relaxation. | 75 |
| 3.7 The isothermal stream function $\Psi_{res}(y, T)$ for a) $\tau_R = 3$ day and b) no relaxation, remapped into depth space. | 76 |
| 3.8 The isothermal stream function $\Psi_{res}(y, T)$ for no surface heat forcing runs: a) $\tau_R = 3$ day and b) no relaxation. | 76 |
| 3.9 The isothermal stream function $\Psi_{res}(y, T)$ for surface restoring runs: a) $\tau_R = 3$ day and b) no relaxation, remapped into depth space. | 78 |
| 3.10 The isothermal stream function $\Psi_{res}(y, T)$ for surface restoring runs: a) $\tau_R = 3$ day and b) no relaxation. | 79 |
| 3.11 The isothermal stream function $\Psi_{res}(y, T)$ for a) $\tau_R = 3$ day and b) no relaxation, remapped into depth space. | 80 |

| | |
|---|----|
| 3.12 The isothermal stream function $\Psi_{res}(y, T)$ for mixed surface restoring and fixed-flux runs: a) $\tau_R = 3$ day and b) no relaxation. | 81 |
| 3.13 The components of the full depth heat budget of the no surface heat forcing runs evaluated in as in Eq. 2.5. | 82 |
| 3.14 Zonal mean diapycnal eddy heat flux divergence for runs with no surface heat forcing for a) Strong sponge b) Closed northern Boundary. . | 83 |
| 3.15 The components of the full depth buoyancy budget for mixed surface forcing runs evaluated in as in Eq. 2.5. | 84 |
| 3.16 Zonal mean diapycnal eddy heat flux divergence in surface restoring runs with closed northern boundary. | 86 |
| 3.17 Zonal mean EKE for no surface forcing runs. a) Strong sponge, b) Closed northern boundary. | 87 |
| 3.18 Zonal mean EKE for surface restoring runs. a) Strong sponge, b) Closed northern boundary c) Closed northern boundary and closed restoring profile. | 88 |
| 3.19 Zonal EPE for surface restoring runs. a) Strong sponge, b) Closed northern boundary c) Closed northern boundary and closed restoring profile. | 89 |
| 3.20 Zonal mean advective heat flux divergence for various surface heat forcing scenarios with closed northern boundary. a) Surface restoring, b) Surface restoring with closed restoration profile c) AC14 surface restoring and d) fixed surface fluxes. | 91 |
| 3.21 Zonal mean diapycnal eddy heat flux divergence for various surface heat forcing scenarios with closed northern boundary. a) Surface restoring, b) Surface restoring with closed restoration profile c) AC14 surface restoring and d) fixed surface fluxes. | 92 |
| 3.22 Meridional temperature gradient for various surface heat forcing scenarios with closed northern boundary. a) Surface restoring, b) Surface restoring with closed restoration profile c) AC14 surface restoring and d) fixed surface fluxes. | 93 |
| 3.23 Meridional eddy heat fluxes for various surface heat forcing scenarios with closed northern boundary. a) Surface restoring, b) Surface restoring with closed restoration profile c) AC14 surface restoring and d) fixed surface fluxes. | 94 |
| 4.1 Sponge layer temperature profiles altering N in Eq. (1.66). | 98 |

| | | |
|------|---|-----|
| 4.2 | The isothermal stream function $\Psi_{res}(y, \theta)$ remapped onto depth coordinates, to give $\Psi_{res}(y, z)$ for various values of N in the sponge layer relaxation profile . Isotherms in multiples of 1°C are overlaid as solid black contours. (Preliminary experiment.) | 100 |
| 4.3 | New temperature profiles for Sponge layer relaxation for update equations a)Varying N (Eq. (4.1)) and b) Varying ΔT (Eq. (4.3)). | 102 |
| 4.4 | The isothermal stream function $\Psi_{res}(y, \theta)$ remapped onto depth coordinates, to give $\Psi_{res}(y, z)$ for a) N = 500 m b) N=750 m, c) N=1000m and d)N= 3000m. Isotherms in multiples of 1°C are overlaid as solid black contours. | 103 |
| 4.5 | The isothermal stream function $\Psi_{res}(y, \theta)$ for a) N = 500 m b) N=750 m, c) N=1000m and d)N= 3000m. | 104 |
| 4.6 | Eulerian overturning ($\bar{\Psi}$) for various values of ΔT . Isotherms in multiples of 1°C are overlaid as solid black contours. | 105 |
| 4.7 | The isothermal stream function $\Psi_{res}(y, \theta)$. For various values of ΔT | 107 |
| 4.8 | The components of the full depth buoyancy budget evaluated in as in Eq. 2.5 for altered sponge layer stratification varying with N. The advective transport component is show in black and diapycnal transport in blue, surface heat forcing in red and the total in thin black line. | 108 |
| 4.9 | Zonal mean diapycnal eddy heat flux divergence for altered sponge layer stratification varying with N. | 109 |
| 4.10 | he components of the full depth buoyancy budget evaluated in as in Eq. 2.5 for altered sponge layer top-to-bottom temperature difference (ΔT).The advective transport component is show in black and diapycnal transport in blue, surface heat forcing in red and the total in thin black line. | 110 |
| 4.11 | Zonal mean diabatic eddy heat flux divergence for altered sponge layer top-to-bottom temperature differences (ΔT). | 112 |
| 4.12 | Zonal mean EKE, for altered sponge layer stratification varying with N. | 113 |
| 4.13 | Zonal mean EKE altered sponge layer top-to-bottom temperature difference (ΔT). | 114 |
| 5.1 | Topography included in non-flat bottom runs. | 118 |
| 5.2 | Instantaneous temperature field for a) and b) Topography runs. c) and d) flat bottom runs. | 120 |
| 5.3 | The Eulerian mean streamfunction ($\bar{\Psi}$) for Flat bottom runs a) and c) and for Topography runs b) and d). | 121 |

| | | |
|------|---|-----|
| 5.4 | The isothermal stream function $\Psi_{res}(y, \theta)$ for relaxation time scales of 3 and infinite days for flat bottom a) and c) runs and topography runs b) and d). | 122 |
| 5.5 | The isothermal stream function $\Psi_{res}(y, \theta)$ remapped onto depth coordinates, to give $\Psi_{res}(y, z)$ for relaxation time scales of 3 and infinite days for flat bottom a) and c) runs and topography runs b) and d). Isotherms in intervals of 1°C are overlaid as solid black contours. Above the surface heat forcing is displayed. | 123 |
| 5.6 | Vertical eddy heat flux (PW) for flat bottom runs a) and c) and topography runs b) and d). Mean vertical heat flux ($\bar{w}\bar{T}$) is show in red, Eddy($\bar{w}'\bar{T}'$) in blue and Total ($\bar{w}\bar{T}$). | 125 |
| 5.7 | Vertical integrated diapycnal eddy heat flux divergence, for flat bottom runs a) and c) and topography runs b) and d). | 126 |
| 5.8 | EKE $\frac{1}{2}(u^2 + v^2)$ sections for relaxation time scales of 3 and infinite days for flat bottom a) and c) runs and topography runs b) and d). Isotherms in intervals of 1°C are overlaid as solid black contours. | 127 |
| 5.9 | Vertically integrated EKE $\frac{1}{2}(u^2 + v^2)$ for relaxation time scales of 3 and infinite days for flat bottom a) and c) runs and topography runs b) and d). | 128 |
| 5.10 | Zonal mean zonal velocity \bar{u} m/s for a) Surface restoring with strong sponge layer, b) fixed heat fluxes and strong sponge layer, c) Surface restoring with Closed northern boundary and d) fixed heat fluxes with a closed northern boundary. | 130 |
| 5.11 | Zonal mean barotropic component of zonal velocity for a) Surface restoring with strong sponge layer, b) fixed heat fluxes and strong sponge layer, c) Surface restoring with Closed northern boundary and d) fixed heat fluxes with a closed northern boundary. | 131 |
| 5.12 | Zonal mean baroclinic component of zonal velocity for a) Surface restoring with strong sponge layer, b) fixed heat fluxes and strong sponge layer, c) Surface restoring with Closed northern boundary and d) fixed heat fluxes with a closed northern boundary. | 132 |
| 6.1 | Linear regression line of best fit for % increase in integrated absolute ROC strength with natural logarithm of % increase in N^2 . $y = mx + c$, $m = -27$, $c = -2$, R value of -0.95 and a P value = 7×10^{-6} | 135 |
| 6.2 | Linear regression line of best fit for % increase in EKE with % increase in N^2 . $y = mx + c$, $m = 15$, $c = 15$, R = 0.99, p value = 10^{-8} | 136 |

Chapter 1

Introduction

Overview

The Southern Ocean is unique, containing a band of latitudes of no continuous topography above 1800m below sea level (*Hallberg and Gnanadesikan*, 2006). Strong polar Westerlies allow for a strong zonal Antarctic Circumpolar Current (ACC) that flows Eastwards around the continent between 56° & 62° S (*Johnson and Bryden*, 1989). This lack of topography and zonal flow results in unique dynamics that play an important role in connecting all the ocean basins as well as completing the global Meridional Overturning Circulation (MOC) (*Marshall and Speer*, 2012) as seen in Fig. 1.1. The Southern Ocean is an important sink of CO_2 with the ACC accounting for around 40% of the global uptake (*Mignone et al.*, 2006).

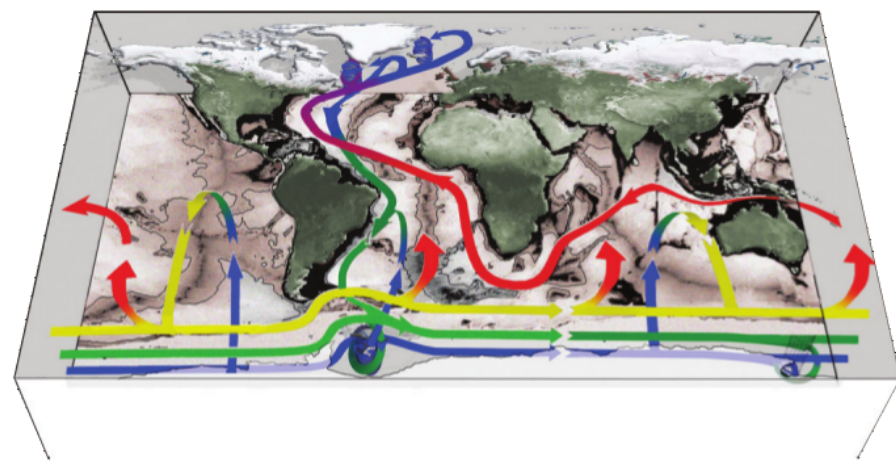


Figure 1.1: Southern Ocean's role in the global overturning schematic from *Marshall and Speer* (2012), with blues and purples representing denser water masses and reds and yellows less dense water masses.

Changes in the Southern Ocean overturning would alter the Southern Ocean

carbon sink changing the upwelling of deep waters rich in Dissolved Inorganic Carbon (DIC), and altering the partial pressure of CO₂ in the ocean. Between 1981 and 2004 the Southern Ocean sink has decreased by 0.08 petagrams of C per year due to increased wind stress showing that the CO₂ sink cannot be assumed to stay constant (*Le Quéré et al.*, 2007).

However the dynamics of the Southern Ocean are complex and poorly understood, with sparse observations in time and space, it is therefore of great interest to fully understand the dynamics of the Southern Ocean and the response to future climate change. Of particular interest in this thesis is how changes in the northern Hemisphere might alter the Southern Ocean. Inter-hemispheric links between the SO ROC and Northern Hemisphere circulation were demonstrated in a number of studies (*Gnanadesikan and Hallberg*, 2000; *Wolfe and Cessi*, 2011). We wish to identify the SO processes involved in this connection. First, we give a basic overview of Southern Ocean dynamics and theory to give context for our investigations before outlining modelling techniques used to investigate them.

1.1 Introduction to Southern Ocean dynamics

As the Southern Ocean plays such a vital role in heat and carbon transport and the global overturning circulation there has been much interest over the years to understand its complex dynamics and how the circulation might change in response to a changing climate. The SO is weakly stratified with very strongly tilted isopycnals across the ACC due to a lack of continental boundaries. This large isopycnal tilt supports a large geostrophic flow in the ACC and provides a route for deep water to move along isopycnals towards the surface. Many isopycnals outcrop and this allows for many density classes to feel direct buoyancy and momentum forcing from the atmosphere, allowing forcing of density classes well below the thermocline.

Strong winds generate sloping isopycnals which are maintained by a lack of continental boundaries. Wind stress is around a maximum at 50°S, which corresponds to a change in sign of wind stress curl ($\nabla \times \tau$). The Southern Hemisphere westerly τ is associated with equatorward Ekman transport, this leads to a surface divergence where the $\nabla \times \tau < 0$ and convergence where $\nabla \times \tau > 0$. Thus a weak vertical velocity shoals isopycnals to the South and depresses them to the North critical for the ACC and the overturning circulation. In the Northern Hemisphere mid-latitudes this is balanced by the development of a mean meridional velocity supported by a zonal pressure gradient, that relaxes isopycnal tilt. In the SO, there is no zonal

pressure gradient to force a mean meridional flow. However some local anomalies in the zonal pressure gradient do arise and are crucial for the ACC.

1.1.1 Eddies in the the Southern Ocean

Eddies play a significant and vital role in the Southern Ocean. In this thesis turbulent flows on spatial scales greater than or equal the Rossby radius ($O 10\text{km}$ in the SO) are referred to as mesoscale eddies, distinct from the mean flow by spatial and temporal perturbations rather than coherent eddies alone. Often referred to as a deviation from the time mean, denoted by a prime ('') symbol.

Oceanic eddies derive their energy primarily from baroclinic and barotropic instability which has an important impact on the large scale circulation. In principle, energy exchange between waves and mean flow can take place in both directions (to and from the mean flow). The energy exchange related to the Reynolds stress ($u'v'$) takes both signs, whereas the term related to the horizontal eddy density flux ($v'\rho'$) is predominantly positive so that energy is transferred from the mean flow to the waves, meaning that the mean flow is unstable to small perturbations. Two physically different mechanisms can be distinguished, corresponding to energy transfer, namely barotropic and baroclinic instability, both of which are important. Sloping isopycnals act as a source of potential energy which can be released as kinetic energy. If two fluid parcels are exchanged and a denser fluid parcel sinks to be replaced with less dense fluid then kinetic energy is released through a vertical exchange or fluid parcels can move along a sloping path between isopycnals maximising at a slope of half that of the isopycnal slope in a slantwise exchange. The slantwise exchange normally transfers heat poleward. This occurs through baroclinic instability.

Eddies can also be generated through horizontal shear in the horizontal velocity though barotropic instability. Barotropic instability is associated with the transport term:

$$-\frac{\partial U}{\partial y} < u'v' >$$

and can only occur if there is a horizontal shear of the background velocity i.e.

$$-\frac{\partial U}{\partial y} \neq 0.$$

Since no vertical shear of U is needed (in contrast to baroclinic instability) a barotropic background current can produce the instability. Analysis of the energetics of the mean current shows that the energy is exchanged with the kinetic energy of

the mean flow.

One of the important consequences of barotropic instability is that flows with small length scales are likely to be unstable. In fact, it can be shown that interacting short Rossby waves are unstable (*Gill et al.*, 1974), which helps to explain the turbulent nature of mesoscale motions in the ocean.

With both sloping isopycnals and strong barotropic flows, there is a very large amount of eddy activity in the SO playing an important role in both the ACC and the Southern Ocean overturning.

1.1.2 Meridional Overturning Circulation

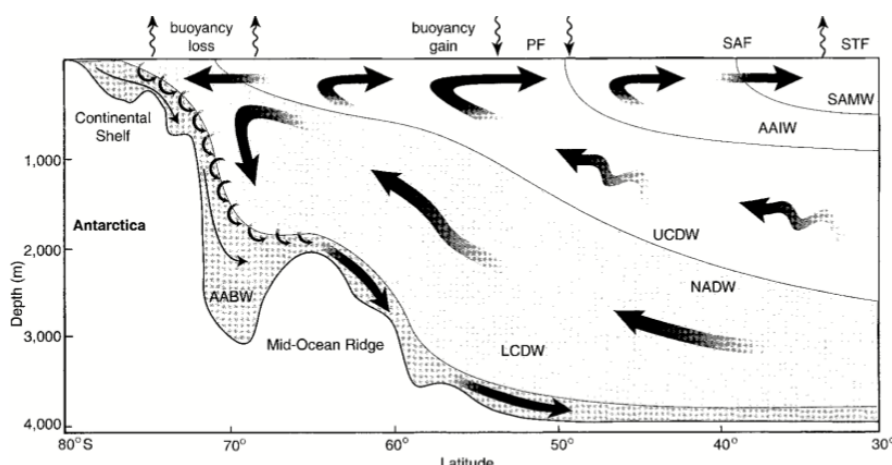


Figure 1.2: Southern Ocean circulation schematic from *Speer et al.* (2000). Showing the main water masses and overturning circulations with the buoyancy forcing. Acronyms are defined in the glossary section for reference.

One of the motivations of this work is understanding the overturning response to altered ocean physics to begin to understand how this might change in future climates. A general schematic is shown in Fig. 1.2 consisting of an upper and lower cell that is counter rotating (*Meredith et al.*, 2012). In the lower cell North Atlantic Deep Water (NADW) upwells near Antarctica and is converted to Antarctic Bottom Water (AABW) that sinks to the deep ocean. In the upper cell, the upwelling water is converted into Antarctic Intermediate Water (AAIW) and Sub Antarctic Mode Water (SAMW) through the addition of heat and fresh water in the surface waters, which have a northward Ekman flow. The Upper cell is controlled by eddy and air-sea forcing (*Rintoul et al.*, 2012) and this upper cell the main focus of the overturning in this thesis.

Strong polar westerlies drive a mean Ekman overturning circulation ($\bar{\Psi}$) that

steepens isopycnals while baroclinic instability drives an opposing eddy-induced circulation (Ψ^*) (*Marshall and Radko*, 2003) and shown in eddy permitting and resolving models *Hallberg and Gnanadesikan* (2006). This partly compensates the ekman circulation leading to a small residual circulation that acts to advect tracers along mean isopycnals (*Speer et al.*, 2000):

$$\psi_{res} = \underbrace{\bar{\psi}}_{mean} + \underbrace{\psi^*}_{eddy}. \quad (1.1)$$

Exactly how eddies interact to contribute to the mean flow is outlined in section 1.2.3. Due to this residual nature of the Southern Ocean overturning the Meridional Overturning Circulation is referred to as the Southern Ocean Residual Overturning Circulation (SOROC). *Toggweiler and Russell* (2008), *Marshall and Radko* (2003) and *Speer et al.* (2000) showed that in the limit of weak interior diapycnal mixing the SO ROC transport must be along mean isopycnal surfaces and can only cross isopycnals in the surface diabatic layer and by deep convective mixing outside the Southern Ocean to connect the surface branch with the deep branch Fig. 1.2. This limit does not apply to the deep cell of the SO ROC, associated with Antarctic Bottom Water formation, but is relevant for the pole-to-pole overturning circulation associated with North Atlantic Deep Water formation (*Wolfe and Cessi*, 2011). This simple residual-mean decomposition allows for the parameterisation of eddies combining Gent-McWilliams and Green and Stone schemes (*Visbeck et al.*, 1997). These parametrisations which have been refined over the years (*Jansen et al.*, 2015, e.g.), but all assume largely adiabatic eddy fluxes.

Some models show up to a 70% disparity in models using full eddy compensation or no eddy compensation, which would have major implications for future anthropogenic CO₂ uptake (*Le Quéré et al.*, 2007). Making it of great interest

1.1.3 ACC

In contrast to gyre circulations strong zonal flows are parallel to wind forcing $\mathbf{u} \cdot \boldsymbol{\tau}_s$ generating the ACC, the Worlds longest and strongest current system, extending 24,000 km long and around 130 ± 10 Sv (*Whitworth and Peterson*, 1985). Like much of Southern Ocean dynamics the ACC is also unique, barotropically flowing Eastward at almost all depths ¹. Although the ACC is actually composed of filaments of jet streams bound by fronts, the ACC is often simplified to one flow

¹Surface pressure gradient and stratification yields a positive shear to reduce the velocity with depth but, rarely enough to lead to a reversal.

that can be approximated in a model by channel domain with periodic flow in the zonal direction. From a momentum balance, Eq. (1.2), it can be seen that wind stress is balanced by bottom form stress that arises from correlation between zonal gradients in bottom topography and pressure anomalies.

$$\bar{\tau}_{wind}^x = p_b \frac{\overline{\partial \eta_b}}{\partial x}, \quad (1.2)$$

where τ_{wind}^x is the zonal wind stress, P_b is bottom pressure and η_b is the bottom topography. High pressure anomalies in SSH and are found upstream of bathymetric features and low pressure anomalies are found in lee of topography. The bottom form stress transfers momentum directly from the ocean into the solid earth. If topography is removed the ACC is seen to be roughly an order of magnitude larger than the observed values as first pointed out in *Munk and Palmén* (1951).

1.1.4 Eddy saturation.

In recent years there has been much debate on the response of the ACC and SO ROC to increasing wind stress due a strong positive trend in the Southern Annular Mode (SAM) index (*Thompson and Solomon*, 2002), this was one of the strongest observed climatic trends *Sallée et al.* (2010). However with longer time series of the SAM index and the inclusion of satellite observations show large inter annual and decadal variability suggest this trend is not as dramatic as it first appeared in the late 1990s (*Hogg et al.*, 2015). None the less variations in response between the the ACC and the SO overturning to intensification of the polar westerlies allowed for a long of research into the mechanisms of eddies in the Southern Ocean and their role in Southern Ocean dynamics. With increasing wind stress there has been little response observed in isopycnal slope (*Böning et al.*, 2008). It is thought there is a near linear response in Eddy Kinetic Energy (EKE) to increased τ_s . Rather than accelerating the ACC transport, the momentum imparted by the wind is transferred to the bottom via interfacial form stress *Meredith and Hogg* (2006). *Morrison and McC. Hogg* (2013) showed a marked difference between eddy saturation and eddy compensation (ekman cancelling), indicating the differing depth scales for eddy driving of ACC and overturning can lead to differing responses to changing momentum forcing. Making the ACC response to altered forcing a worth while investigation as it may not have a similar response to the the SO ROC.

1.2 Residual Mean and Transformed Eulerian Mean Theory

Due to the unique dynamics of the Southern Ocean the large scale mean circulation is influenced by the small scale time-varying components. Therefore time varying eddies need to be taken into account to establish the residual circulation rather than the fictitious deacon cell (*Döös and Webb, 1994*). Thus tend to approach SO dynamics in terms of residuals. This approach will be used throughout this thesis and the background theory is outlined here.

1.2.1 Assumptions and approximations:

Insert better justification here First we outline the major assumptions and approximations used in order to simplify the equations used.

Boussinesq approximation

We assume a Boussinesq fluid (Volume is conserved) as variations in density with depth are just 2-3 % , $\rho_0(z)$ becomes ρ_0 allowing the Boussinesq equations:

$$\rho_0 \frac{Du}{Dt} = -2\rho_0 \Omega \times u - \nabla \tilde{p} - \tilde{p} \nabla \Phi + \mathcal{F}, \quad (1.3)$$

$$\nabla \cdot u = 0, \quad (1.4)$$

$$\rho_0 \frac{D(\theta, S)}{Dt} = (\mathcal{G}_S, \mathcal{G}_\theta), \quad (1.5)$$

$$\tilde{\rho} = F(S, \theta, \rho_0) + F(S_0, \theta_0, \rho_0(z)), \quad (1.6)$$

where 1.4 is the Incompressibility equation in an adiabatic system. The symbols are defined in the list of symbols section in the glossary.

Small Rossby number

Rossby number is small meaning the Coriolis frequency is important.

$$R_o = \frac{U}{f_o L} \ll 1, \quad (1.7)$$

where R_o is the Rossby number.

F-plane:

The β effect is small so that:

$$\frac{\beta L}{f} \leq R_o \quad (1.8)$$

Static stability

Brunt Väisälä frequency (N^2) is a function of depth (z) only so

$$N^2(z) = \frac{\partial b}{\partial z} \quad (1.9)$$

where b is buoyancy.

Hydrostatic balance

$$\frac{\partial \psi}{\partial z} = \frac{b}{f_o} \quad (1.10)$$

Quasi-Geostrophy

Assume Quasi-Geostrophic (QG) so there is no mean advection and no vertical component of eddy Potential Vorticity (PV) flux. QG assumes small Rossby number, which we already assume along side:

- **Small aspect ratio:** Isopycnals have small slope as horizontal dimensions of ocean basins are much larger than vertical dimensions. Gives small vertical motions:

$$\frac{\partial_x b}{\partial_z b} \& \frac{\partial_y b}{\partial_z b} \leq R_o \quad (1.11)$$

- **Small Ek number:** $E_k \ll 1$.
- stratified background state
- all effects of compressibility neglected

These assumptions allow us to write a geostrophic streamfunction:

The horizontal velocity divergence is 0.

$$\frac{\partial u}{\partial x} + \frac{\partial v}{\partial y} = 0. \quad (1.12)$$

We can write:

$$u = -\frac{\partial \psi}{\partial y}, \quad v = \frac{\partial \psi}{\partial x}, \quad w = o, \quad (1.13)$$

where ψ is the geostrophic stream function:

$$\psi = \frac{\rho - \rho_o(z)}{\rho_o f_o} \quad (1.14)$$

Now starting from the QG equations:

$$\underbrace{D_g}_{\text{time derivative}} u - \beta y v - \underbrace{f_o v_a}_{\text{ageostrophic velocities}} = \underbrace{\mathcal{G}_x}_{\text{External forcing on momentum}}, \quad (1.15)$$

$$D_g v - \beta y u - f_o u_a = \mathcal{G}_y, \quad (1.16)$$

$$\frac{\partial u_a}{\partial x} + \frac{\partial v_a}{\partial y} + \frac{\partial w_a}{\partial z} = 0, \quad (1.17)$$

$$D_g + N^2 w_a = \underbrace{\mathcal{B}}_{\text{nonconservative buoyancy forces}} - \frac{\partial \bar{v}' b'}{\partial y}. \quad (1.18)$$

Where D_g is the material derivative: (

$$D_g = \frac{\partial}{\partial t} + u \frac{\partial}{\partial x} + v \frac{\partial}{\partial y}. \quad (1.19)$$

Other symbols are define in the list of symbols). The ageostrophic velocity is the difference between the actual velocity and the geostrophic one. The external forcing (\mathcal{G}) arises from wind, stress and friction etc. The non-conservative buoyancy forcing (\mathcal{B}) is from small scale mixing, and surface heat fluxes etc.

Combining this using PV:

$$q = f_o + \beta y + \frac{\partial v}{\partial x} - \frac{\partial u}{\partial y} + f_o \frac{\partial \frac{b}{N^2}}{\partial z} \quad (1.20)$$

and substituting the QG equations into:

$$\chi = \frac{\partial \mathcal{G}_y}{\partial x} - \frac{\partial \mathcal{G}_x}{\partial y} + \frac{\partial u}{\partial y} + f_o \frac{\partial \mathcal{B}}{N^2} \partial z \quad (1.21)$$

This gives the equation for Quasi-geostrophic Potential Vorticity (QGPV). If $\mathcal{G} = 0$ and $\mathcal{B} = 0$ then q is conserved (conservative flow). If flow is not conserved

then χ represents local sources and sinks of q (viscous and diabatic effects).

$$D_g q = \chi \quad (1.22)$$

1.2.2 Eliassen-Palm theorem

For small amplitude motions we can use:

$$\bar{u}(y, t) = \partial_y \bar{\psi} \quad (1.23)$$

$$\partial_y \bar{b} = -f_o \partial_z \bar{u}, \quad (1.24)$$

then substituting into Eq. (1.20). We get the mean PV in terms of the geostrophic streamfunction:

$$\bar{q} = f_o + \beta y + \frac{\partial^2 \psi}{\partial y^2} + \frac{\partial^2 \psi}{\partial z^2} \frac{\partial \frac{f_o^2}{N^2}}{\partial z}. \quad (1.25)$$

As ψ can be decomposed into eddy and mean contributions:

$$\psi' = \psi - \bar{\psi}$$

The eddy vorticity (q') can be described as:

$$q' = f_o + \beta y + \frac{\partial^2 \psi'}{\partial y^2} + f \frac{\partial^2 \psi}{\partial z^2} \frac{\partial \frac{f_o^2}{N^2}}{\partial z} \quad (1.26)$$

and the eddy velocity as:

$$v' = \frac{\partial \psi'}{\partial x}. \quad (1.27)$$

So the eddy PV flux can be described by:

$$\overline{v' q'} = \frac{\partial(-\overline{u' v'})}{\partial y} + \frac{\partial \frac{f_o}{N^2} (\overline{v' b'})}{\partial z}. \quad (1.28)$$

This can be simplified defining the Eliassen-Palms flux \mathbf{F} as:

$$\mathbf{F} = \begin{pmatrix} -\overline{u' v'} \\ \frac{f_o}{N^2} \overline{v' b'} \end{pmatrix}, \quad (1.29)$$

where the meridional component is the negative of the zonal eddy momentum and the vertical is proportional to the meridional eddy buoyancy flux.

So the eddy PV flux can be written simply as:

$$\overline{v'q'} = \nabla \cdot \mathbf{F}. \quad (1.30)$$

Now linearising the QGPV Eq. (1.22) we get:

$$\frac{\partial q'}{\partial t} + \bar{u} \frac{\partial q'}{\partial x} + \bar{v} \frac{\partial \bar{q}}{\partial y} = \chi. \quad (1.31)$$

Then we rearrange by multiplying by q' and averaging we get:

$$\underbrace{\frac{\partial q'^2}{\partial t} + \underbrace{\bar{u}q' \frac{\partial q'}{\partial x}}_{\substack{\text{time av removes} \\ =0 \text{ when waves are steady}}} + \underbrace{\bar{v}'q' \frac{\partial \bar{q}}{\partial y}}_{\substack{=0 \text{ if waves are conservative}}} = \overline{\psi'q'}}_{\substack{=0 \text{ when waves are steady}}} \quad (1.32)$$

which is the eddy enstrophy equation. If waves are non divergent then $\nabla \cdot F = 0$, meaning there is no eddy PV flux ($\overline{v'q'} = 0$).

This allows us to show eddies impacting the mean zonal circulation in the QGPV budget²:

$$\frac{\partial \bar{q}}{\partial t} + \frac{\partial \overline{v'q'}}{\partial y} = \bar{\psi}. \quad (1.33)$$

To simplify the problem we introduce Transformed Eulerian Mean (TEM) theory.

1.2.3 Transformed Eulerian Mean theory

Most of this theory is outlined in *Marshall and Radko* (2003). Starting from the QG equations outlined in section 1.2.1. Eddy buoyancy and momentum fluxes change the mean zonal state through the terms $\frac{\partial(\bar{v}'b')}{\partial y}$ and $\frac{\partial(\bar{u}'v')}{\partial y}$ in equations Eq. (1.18) and Eq. (1.15).³

²For small, steady and conservative waves the eddy flux doesn't impact the mean flow (non acceleration theorem).

³Sometimes there is no eddy momentum fluxes but thermal wind balance insists both momentum and buoyancy fluxes are required to change the mean flow so eddies will drive the ageostrophic terms as well inducing an ageostrophic mean motion.

If we redefine a mean meridional ageostrophic circulation.

Using Eq. (2.8) and Eq. (1.17) defining the ageostrophic streamfunction as:

$$(\bar{v}_a, \bar{w}_a) = \left(\frac{\partial \bar{\psi}}{\partial y}, \frac{\partial \bar{\psi}}{\partial z} \right). \quad (1.34)$$

And putting back into the mean buoyancy budget Eq. (1.18)

$$\frac{\partial \bar{b}}{\partial t} + \frac{\partial \bar{\psi}}{\partial z} N^2 + \frac{\partial (\bar{v}' b')}{\partial y} = \bar{\mathcal{B}},$$

assuming static stratification so that $N^2 = N^2(z)$ and that $\frac{\partial \bar{v}_a}{\partial y} = -\frac{\partial \bar{w}_a}{\partial z} = \frac{\partial \bar{\psi}}{\partial y}$

Gives:

$$\frac{\partial \bar{b}}{\partial t} + \frac{\partial (\bar{\psi} N^2 + \bar{v}' b')}{\partial y} = \bar{\mathcal{B}} \quad (1.35)$$

Moving N^2 out of brackets as it doesn't vary with latitude (static stability assumption):

$$\frac{\partial \bar{b}}{\partial t} + \frac{\partial (\bar{\psi} + \frac{\bar{v}' b'}{N^2})}{\partial y} N^2 = \bar{\mathcal{B}}. \quad (1.36)$$

Here the term $\frac{\bar{v}' b'}{N^2}$ is the eddy flux term (giving a mean advection) so we can define ψ^* as the eddy induced mean stream function:

$$\psi^* = \frac{\bar{v}' b'}{N^2} \quad (1.37)$$

And the residual stream function is defined as:

$$\underbrace{\psi_{res}}_{\text{residual}} = \underbrace{\bar{\psi}}_{\text{ageostrophic}} + \underbrace{\psi^*}_{\text{eddy}} \quad (1.38)$$

Now we can define a residual circulation:

$$(\bar{v}_{res}, \bar{w}_{res}) = \left(\frac{\partial \psi_{res}}{\partial y}, \frac{\partial \psi_{res}}{\partial z} \right) \quad (1.39)$$

So if we now put ψ_{res} back into the mean buoyancy budget Eq. (1.18), the eddy

terms fall out:

$$\frac{\partial \bar{b}}{\partial t} + \overline{w_a} N^2 = \bar{\mathcal{B}} - \underbrace{\frac{\partial \psi^*}{\partial y}}_{\psi_{res} - \bar{\psi}} N^2$$

$$\frac{\partial \bar{b}}{\partial t} + \overline{w_a} N^2 = \bar{\mathcal{B}} - \underbrace{\frac{\partial \psi_{res}}{\partial y}}_{\overline{w^*}} N^2 - \underbrace{\frac{\partial \bar{\psi}}{\partial y}}_{\overline{w_a}} N^2$$

$$\frac{\partial \bar{b}}{\partial t} + \overline{w_a} N^2 = \bar{\mathcal{B}} - \overline{w_{res}} N^2 - \overline{w_a} N^2$$

Which removes the eddy terms in the mean buoyancy budget:

$$\frac{\partial \bar{b}}{\partial t} + \overline{w_{res}} N^2 = \bar{\mathcal{B}} \quad (1.40)$$

The equations of momentum “transformed” :

$$\frac{\partial \bar{u}}{\partial t} - f_o \overline{v^*} = \overline{\mathcal{G}_x} + \underbrace{\overline{v'q'}}_{\nabla \cdot \mathbf{F} \text{ eddy forcing}} \quad (1.41)$$

$$f_o \frac{\partial \bar{u}}{\partial z} = - \frac{\bar{b}}{\partial y} \quad (1.42)$$

$$\frac{\partial \overline{v^*}}{\partial y} + \frac{\partial \overline{w^*}}{\partial z} = 0 \quad (1.43)$$

and the mean buoyancy budget

$$\frac{\partial \bar{b}}{\partial t} + \overline{w^*} N^2 = \bar{\mathcal{B}}.$$

So from the term $\nabla \cdot \mathbf{F}$ in Eq. (1.41) showing that if the flow is conservative (non accelerational then there are no eddy influences!).

Momentum and buoyancy balances

The mean buoyancy budget ⁴

$$\frac{\bar{v}\partial\bar{b}}{\partial y} + \frac{\bar{w}\partial\bar{b}}{\partial z} + \underbrace{\frac{\partial v'b'}{\partial y}}_{\text{EP flux}} + \underbrace{\frac{\partial w'b'}{\partial y}}_{\cdot \text{Buoyancy forcing due to air-sea interactions and small scale mixing}} = \frac{\partial B}{\partial z} \quad (1.44)$$

In terms of a residual circulation:

$$\psi_{res} = \bar{\psi} + \psi^* \quad (1.45)$$

$$\psi^* = \underbrace{\frac{-w'b'}{b_y}}_{\text{mean meridional buoyancy gradient}} \quad (1.46)$$

Assuming that $\bar{v}'b'$ is in the \bar{b} surface (assume all the eddy fluxes are along isopycnals) so that $\nabla \cdot \bar{v}'b'$ can be written as fluxes along isopycnals as advective transport $\mathbf{v}^* \nabla \bar{b}$:

$$u' \frac{\partial \bar{b}}{\partial x} + v' \frac{\partial \bar{b}}{\partial y} + w' \frac{\partial \bar{b}}{\partial z} \quad (1.47)$$

And replacing \bar{v} and \bar{w} with:

$$\begin{aligned} \bar{w} &= \frac{-\partial \psi_{res}}{\partial z} + \frac{-\partial \psi^*}{\partial z} \\ \bar{v} &= \frac{-\partial \psi_{res}}{\partial y} + \frac{-\partial \psi^*}{\partial y} \end{aligned}$$

Then decomposing the eddy flux $(v'b', w'b')$ into along \bar{b} components: $(\frac{w'b'}{S_p}, \frac{w'b'}{S_p})$ and horizontal components $(\bar{v}'b' - \frac{w'b'}{S_p}, 0)$ where:

$$S_p = \frac{-\bar{b}_y}{\bar{b}_z}. \quad (1.48)$$

The buoyancy budget can be written in terms of a residual flux:

$$\left(\frac{\partial \psi_{res}}{\partial y} \right) + \left(\frac{\partial \psi^*}{\partial z} \right) \frac{\partial \bar{b}}{\partial y} + \left(\frac{\partial \psi^*}{\partial z} - \frac{\partial \psi_{res}}{\partial z} \right) \frac{\partial \bar{b}}{\partial z} + \frac{\partial (\bar{v}'b' - \frac{w'b'}{S_p}, \frac{w'b'}{S_p})}{\partial y} + \frac{\partial (\bar{w}'b', 0)}{\partial z} = \frac{\partial B}{\partial z}$$

If we define μ as:

$$\mu = \left(\frac{\bar{w}'b'}{\bar{v}'b'} \right) \left(\frac{1}{S_p} \right)$$

⁴Zonal average refer to stream wise averages in the presence of topography, so that eddy fluxes are transient.

We get:

$$\underbrace{\left(\frac{\partial \psi_{res}}{\partial y} \right) \frac{\partial \bar{b}}{\partial y} + \left(\frac{\partial \psi_{res}}{\partial z} \right) \frac{\partial \bar{b}}{\partial z}}_{\text{Jacobian } J(\psi_{res}, \bar{b})} = \frac{\partial B}{\partial z} - \frac{\partial (\bar{v}' \bar{b}')}{\partial y}$$

And substituting in μ

$$J(\psi_{res}, \bar{b}) = \frac{\partial B}{\partial z} - \frac{\partial (1 - \mu) \bar{v}' \bar{b}'}{\partial y} \quad (1.49)$$

When $\mu = 1$ then $\frac{\partial(0)}{\partial y}$ then the eddy flux is solely along \bar{b} surfaces and there are no diapycnal fluxes (pure advection). (The interior = adiabatic so $\mu = 1$).

When $\mu = 0$ then diapycnal fluxes are important (e.g. in the mixed layer) so eddy fluxes are across buoyancy surfaces $\bar{w}' \bar{b}' = 0$. Mostly these surface fluxes are taken to be negligible and the adiabatic components are assumed to be the significant components. In the limit of adiabatic eddies, vanishingly small mixing and air-sea buoyancy fluxes ($\mu = B = 0$) so that:

$$\psi^* = \frac{\bar{w}' \bar{b}'}{\bar{b}_y} \quad (1.50)$$

to give:

$$\frac{\partial \psi_{res}}{\partial y} \frac{\partial \bar{b}}{\partial z} - \frac{\partial \psi_{res}}{\partial z} \frac{\partial \bar{b}}{\partial y} = 0 \quad (1.51)$$

So \bar{b} is advected by ψ_{res} .

Evaluating Eq. (1.49) at the base of the mixed layer *Marshall and Radko* (2003) devised a well used diagnostic. Assuming that $\frac{\partial b}{\partial z} = 0$ (vertical isopycnals) we can remove a term from the LHS:

$$\cancel{\frac{\partial \psi_{res}}{\partial z} \frac{\partial \bar{b}}{\partial z}} - \frac{\partial \psi_{res}}{\partial z} \frac{\partial b_0}{\partial y} = \frac{\partial B}{\partial z} - (1 - \mu) \frac{\partial}{\partial y} (\bar{v}' \bar{b}'),$$

and integrate over the mixed layer to give:

$$\int_{-h_{ml}}^0 -\frac{\partial \psi_{res}}{\partial z} \frac{\partial b_0}{\partial y} dz = \int_{h_{ml}}^0 \frac{\partial B}{\partial z} - (1 - \mu) \frac{\partial}{\partial y} (\bar{v}' \bar{b}') dz.$$

Evaluating at the base of the mixed layer; ψ_{res} goes to zero at the surface. This allows us to write the LHS as the $\psi_{res}|_{z=0} - \psi_{res}|_{z=h_{ml}}$

$$0 - \psi_{res}|_{z=h_{ml}} \frac{\partial b_0}{\partial y} = B_0 - (1 - \mu) \int_{h_{ml}}^0 \frac{\partial}{\partial y} (\bar{v}' \bar{b}') dz$$

which is often condensed to:

$$\psi_{res}|_{z=h_{ml}} \frac{\partial b_0}{\partial y} = \underbrace{\tilde{B}_0}_{\text{net buoyancy supplied to the mixed layer by air-sea fluxes and lateral adiabatic eddy fluxes}} \quad (1.52)$$

This allows for a simple diagnostic tool: If $\tilde{B} > 0$ (Buoyancy gain (heating)) then $\frac{\partial b_0}{\partial y} > 0$ so $\psi_{res}|_{z=h_{ml}} > 0$. Relating surface buoyancy gain/loss to the sign of the SO ROC. Often we see this buoyancy gain/loss to be taken as simply the surface heat fluxes where the diabatic eddy contribution is assumed to be negligible.

1.3 TEM in The Surface Layers

This original framework presented in *Marshall and Radko* (2003) does not allow for real irreversible diapycnal eddy fluxes as Quasi-Geostrophy approximations are used. Which requires assumptions such as a small aspect ratio which ceases to be true in the surface mixed layer. When trying to establish the components of eddy fluxes we must consider how the surface mixed layer is handled in order to truly remove the along isopycnal component. In section 1.2.3 we use Eq. (1.37) which is taken from a Q-G case in *Andrews and McIntyre* (1976) which is inconsistent with Fig. 1.3 where we expect very steep isopycnals in the diabatic layer. Eq. (1.37) would only be sufficient in the interior where $|\bar{b}_z| \gg |\bar{b}_y|$ (strongly stratified). If there is any surface buoyancy gradient there will be diapycnal eddy fluxes and therefore vertical residual flux through the surface. To circumnavigate this issue *Held and Schneider* (1999); *Trégouier et al.* (1997) introduce a vanishingly thin surface layer in which the residual flow transitions to zero at the surface as used in the mixed layer diagnostic Eq. (1.52) where the residual flux is assumed zero at the surface and only the base of the mixed layer is considered.

In the mixed layer $|\bar{b}_y| \gg |\bar{b}_z|$ the eddy streamfunction becomes:

$$\Psi = \frac{\overline{w' \bar{b}'}}{\bar{b}_y}, \quad (1.53)$$

from *Held and Schneider* (1999). This gives horizontal fluxes in the mixed layers so no residual flux through the surface. However in this definition is not applicable in the interior where both the denominator and numerator in Eq. (1.53) may be

very small leading to large errors. Thus it would be suggested to use Eq. (1.37) in the interior and Eq. (1.53) in the mixed layer with the surface mass flux spread over the transition region.

Plumb and Ferrari (2005) suggest an alternative definition of Ψ :

$$\Psi = -|\nabla \bar{b}|^{-1}(\mathbf{s} \cdot \overline{\mathbf{u}' b'}), \quad (1.54)$$

and a residual diapycnal eddy buoyancy flux:

$$\mathbf{F}(b) = \mathbf{n}(\mathbf{n} \cdot \overline{\mathbf{u}' b'}), \quad (1.55)$$

directed along mean buoyancy gradient. Where vector \mathbf{n} is the mean buoyancy gradient ($\nabla \bar{b}/|\bar{b}|$) and vector \mathbf{s} is along mean buoyancy surfaces ($\mathbf{n} \times \mathbf{i}$), which was implemented in *Kuo et al.* (2005). Where the buoyancy budget is rewritten:

$$\frac{\partial \bar{b}}{\partial t} + \overline{\mathbf{u}_{res} \cdot \nabla \bar{b}} = -\mathbf{n}(\mathbf{n} \cdot \overline{\mathbf{u}' b'}) - \overline{B}_z. \quad (1.56)$$

Once again to evaluate such a budget the diabatic eddy heat flux is take as 0 at the base of the mixed layer .

$$\int_{z_i}^{z_0} (\nabla \cdot (\chi_{res} \mathbf{j} \times \nabla \bar{b}) + \int_{z_i}^{z_0} \nabla \cdot \mathbf{F}(b) dz = -B_0 \quad (1.57)$$

From below the surface mixed layer the residual buoyancy transport and diabatic residual eddy buoyancy flux (χ_{res} and $\mathbf{F}(b)$ respectively) are negligible in an adiabatic interior. The surface buoyancy budged in a balance between the surface fluxes and horizontal buoyancy transports:

$$\frac{1}{y} \frac{\partial}{\partial y} \left[y \int_{z_i}^{z_0} (\mathbf{F}(b) + \chi_{res} \bar{b}_z) \right] = -B_0 \quad (1.58)$$

here *Kuo et al.* (2005) assumes a non-zero vertical buoyancy gradient. Allowing residual eddy buoyancy fluxes to play a role in the surface heat budget alongside the residual buoyancy advection.

1.4 Motivation

The resolution of current climate models is restricted by computational limitations, the average resolutions of coupled climate models is 1 deg , so they require parameterization of eddies. Thus the complex interaction of eddy processes in the Southern Ocean may not be fully captured in those models. These parameterization schemes do not represent diabatic eddy fluxes well, which could lead to missing feedbacks

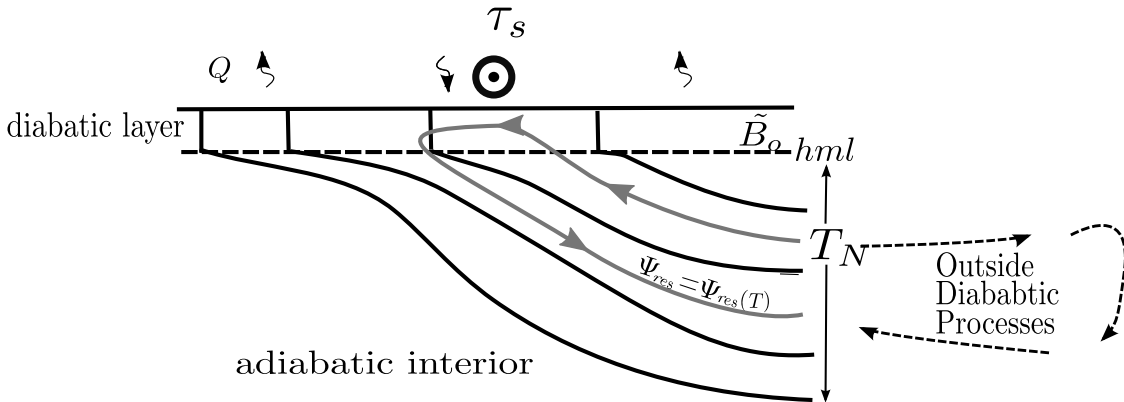


Figure 1.3: Southern Ocean Overturning Circulation directed along isopycnals related to surface forcing and outside diabatic processes. Adapted from *Marshall and Radko* (2003) schematic.

in global climate models. As a result, the debate is still open as to whether eddy parametrisations should be purely adiabatic or have additional diapycnal mixing terms (*Gent*, 2011). It is of great interest to understand what possible feedbacks are being neglected in climate models and what the physical processes behind them are, thus we use idealised models to gain a better understanding of processes that are important when we consider the future response of the Southern Ocean.

Marshall and Radko (2003) showed that in most realistic cases the diabatic eddy contribution is often small compared to the surface forcing and that the SO ROC can be predicted from the surface forcing using Eq. (1.52). Many studies, however, show an interhemispheric connection via the Atlantic meridional overturning circulation (AMOC) and North Atlantic Deep Water (NADW) formation, which acts as a control on the SO ROC (e.g. *Wolfe and Cessi* (2009), *Nikurashin and Vallis* (2012), and from the *Marshall and Radko* (2003) schematic). This suggests that the interhemispheric control on the SO ROC occurs via changes in the budget of Eq. 1.49. When investigating the SO ROC in a channel model the rest of the worlds ocean must be represented via a northern boundary condition, i.e. the stratification north of the channel, impacting the isopycnal slope in the interior of the channel. We wish to investigate the effects of that northern boundary condition on setting the SO ROC in a channel model and dynamics set by the northern boundary.

Within the *Marshall and Radko* (2003) framework we can see that the Southern Ocean is not disconnected from the rest of the worlds oceans, and must rely on outside diabatic processes to close the SO ROC see Fig. 1.3. We wish to investigate in a very idealised, theoretical, way the possible mechanisms and controls on the SO ROC. This will allow us to illuminate possible considerations that may be overlooked when setting up channel models and glimpse possible interactions with

boundary conditions that may have been previously unconsidered.

1.5 Outline of model

1.5.1 MITgcm overview

The model code used is the Massachusetts Institute of Technology general circulation model (MITgcm) (*Marshall et al.*, 1997). The MITgcm is a finite difference primitive equation model solver rooted in the incompressible Navier-Stokes equations. Assuming the flow is incompressible:

$$D_t \rho \ll \rho \nabla \cdot v, \quad (1.59)$$

to filter the acoustic modes. Density perturbations are assumed to be smaller compared to the reference density:

$$\rho' = (\rho - \rho_0) \ll \rho_0. \quad (1.60)$$

This allows the use of the Boussinesq approximation to make the momentum equations more linear. Therefore the incompressible Boussinesq equations are:

$$\begin{aligned} \rho_0 D_t \mathbf{v} + 2\Omega \times \rho_0 \mathbf{v} + g \rho \hat{k} + \nabla \rho &= \mathbf{F} \\ \rho_0 \nabla \cdot \mathbf{v} &= 0 \\ \partial_t \eta + \nabla \cdot (H + \eta) \mathbf{v} &= P - E \\ D_t \theta &= Q_\theta \\ D_t s &= Q_s \\ \rho &= \rho(s, \theta, p) \end{aligned} \quad (1.61)$$

where \mathbf{v} is velocity, p is pressure ρ is density, η is the displacement of free surface from resting sea-level, θ is potential temperature, s is salinity, ρ_0 is the reference density, g is gravitational acceleration, H is bottom depth, \mathbf{F} , $P-E$, Q_θ , Q_s are forcing fields (*Adcroft et al.*, 2004). The hydrostatic approximation is also made for horizontal resolutions coarser than 1km (*Adcroft et al.*, 2004). Many of these approximations were discussed and used in 1.2.3.

The model is then discretized using finite volume methodology (*Adcroft et al.*, 1997). Where the governing equations are integrated over finite volumes and applying the Guass-divergence theorem to give a continuity in the form:

$$A_{east}^u u_{east} - A_{west}^u u_{west} + A_{north}^v v_{north} - A_{south}^v v_{south} + A_{up}^w w_{up} - A_{down}^w w_{down} = 0, \quad (1.62)$$

written in terms of the normal flow across cell faces. With no normal flow at rigid boundaries (volume flux though a rigid boundary is set to zero). The components of velocity are staggered on an Arakawa C grid (*Chang et al.*, 1977) in the horizontal and a Lorenz grid in the vertical (*Lorenz*, 1960) see Fig. 1.4.

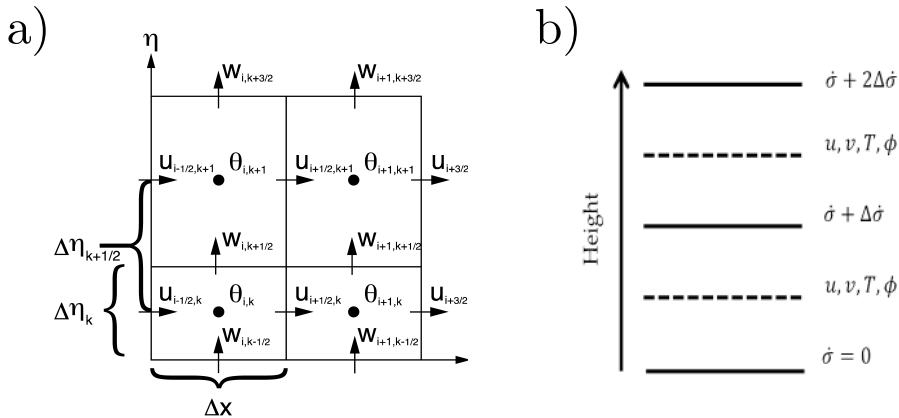


Figure 1.4: A illustration of the horizontal and vertical grid spacing. a) Arakawa C grid and b) Lorenz vertical grid. *Adapted from (Collins et al., 2013)*

The model then discretizes the momentum equations between time levels and substitutes then into the discrete continuity equation to obtain an elliptic equation for pressure, refer to *Marshall et al.* (1997) for detailed explanation of Algorithms used. Information referring to finite volume advection is discussed in appendix A. In the following section we outline the parameters and boundary conditions applied to set up the MITgcm for our purpose.

1.5.2 Considering model set up

First we have to consider the best to approach modelling this problem within temporal and computational limits. It is not feasible to run a high resolution eddy resolving coupled climate model altering NADW formations and analysing the SOROC and diabatic eddy response. This would also be too complex to fully understand the important factors controlling the diabatic eddy response and the underlying physics. In order to reduce computational costs, we can run an idealised channel model with periodic flow, applying boundary conditions to mimic the processes outside of the southern ocean. We then have to apply surface and bottom boundary conditions and forcing to generate the appropriate flow and circulation. A simple box ocean can then be used to run a high resolution simulation to enable us to examine the basic physics controlling southern ocean diabatic eddies.

Here we outline the rational for the most basic parameters, before going on to give a full overview of the generalised set up that all the simulations will be based

off.

Fundamental parameters

A few fundamental parameters must be decided to establish a trade off between computational cost, most appropriate physics and ease of analysis to test the basic theory. In order to gain a better understanding we require a model setup that can be run many times with altered boundary conditions.

Domain size: Minimised for computational efficiency. Depth 3000 m (if no topography), but must be 4000 m if ridges are included. In absence of topography width need only be 1000 km as no meanders in the ACC to consider. The meridional length must allow space for boundary conditions and forcing variation so we have chosen 2000 km.

Resolution: To achieve the most appropriate results we have chosen a standard horizontal resolution of 5 km, this is just about eddy resolving. Considering the Rossby radius of deformation is:

$$L_d = \frac{NH}{f}, \quad (1.63)$$

where N is the buoyancy frequency typically $3 \times 10^{-3} \text{ s}^{-1}$, H is thickness scale (typically 1000 m) and f is the Coriolis parameter ($1 \times 10^{-4} \text{ s}^{-1}$ - $1.3 \times 10^{-4} \text{ s}^{-1}$). Giving values of 10-30 km. Allowing for a minimum of 2 grid spacing per radius.

Diffusion: Set to zero for an adiabatic interior

EOS: For simplistic idealised models only a linear equation of state can be used to establish qualitative results ideal for starting to understand a poorly understood mechanism. In more complex models this would not suffice.

Time Step: Set to 450s, depending on resolution to satisfy the CourantFriedrichsLowy (CFL) condition.

Other run time parameters are outlined in appendix B, where we include an example data file. Next, with these constraints in mind, the next most fundamental aspects of the model set up are the boundary conditions applied.

Northern boundary conditions

In order to begin to understand how the diabatic eddies might respond to an altered northern boundary condition. We must decide how to represent the rest

of the World Oceans in the model, as the SO is not disconnected from the rest of the world and the SO ROC requires diabatic processes to the north of the ACC in order to close. To this end we considered 3 ways of dealing with the outside of the SO:

1. Another additional basin representing the northern hemisphere
 2. Enhanced vertical diffusion
 3. Sponge layer
1. Similar to *Saenz et al.* (2012), which to be run at a high enough resolution would be far to computationally expensive, when considering the number of model runs to be performed. The *Saenz et al.* (2012) model was run at a resolution of $1/4^\circ$ and at least $1/12^\circ$ would be required to investigate the eddy dynamics in the SO. These factors ruled out the additional basin method.
2. With no heat flux through the northern boundary a shallow thermocline will be generated. Therefore excess vertical diffusion can be applied near the northern edge of the domain to increase the thermocline depth, north of the most northernmost front. Enhanced diffusion in the north of the domain represents the overturning circulation, wind-driven circulation and vertical mixing acting throughout the global ocean. Changes in stratification due to variations in surface buoyancy are felt very quickly compared with slow (millennia) equilibration times in the real ocean *Allison et al.* (2010). Preliminary experiments using enhanced vertical diffusion, following variations of the model set up used in *Hogg* (2010), were unsuccessful in generating a sensible overturning (*not shown here*). The average EKE of these tests were too low and generated little eddy compensation (overturning was not the focus of the *Hogg* (2010) experiments). Therefore enhanced diffusion is not suitable for investigating changes in the SO ROC and diabatic eddies.
3. Sponge layer models where temperature/density is relaxed to a prescribed profile have shown promising results in a number of other studies (*Abernathay et al.*, 2011; *Abernathay and Cessi*, 2014; *Zhai and Munday*, 2014)[etc]. Preliminary experiments using a Sponge layer to relax to a set temperature profile as in

Abernathay et al. (2011) were able to generate a sensible SOROC by mimicking diabatic processes outside the southern ocean.⁵

Preliminary experiments helped us to establish the most appropriate northern boundary condition as a sponge layer relaxing to a set temperature profile. Outlined later in detail in section 1.6.

Surface boundary conditions

Considerations:

1. Atmosphere

2. Free surface

3. Heat

4. Wind

1. To reduce complexity and computational cost we chose an ocean only model noting that coupling to an atmosphere would perhaps be an interesting addition for future work.

2. The MITgcm allows a free surface or rigid lid surface boundary condition, the only additional complication with a free surface boundary condition is the additional requirement of a free surface correction in vertically integrated tracer budgets⁶. The upper surface of the ocean is a free surface which is driven by the divergence of volume flux in the interior. We chose a linear free-surface which permits surface gravity waves with finite phase speed and introduces a Helmholtz term in the surface pressure equation. This is a very good approximation for deep water where $\eta \ll H$ (*Campin et al.*, 2004) such as in our channel model setup. Using a non-linear free surface has many additional complications and extra computational cost with no benefits, so is not considered appropriate here.

⁵NB: A very small amount of random noise: $O10^{-5}$ must be added to the temperature layers to prevent laminar flow (*Abernathay Pers coms*)

⁶On calculation this is very small and can be neglected. This correction term is outlined later in budget analysis when applied in the relevant chapters.

3. Buoyancy forcing in the absence of an atmosphere for heat exchange can be achieved via a number of methods in the MITgcm. As we are using an equation of state linear in temperature only, we only consider buoyancy forcing from heat forcing and not from evaporation and precipitation/ freshwater forcing. The simplest buoyancy forcing would be a fixed surface heat flux Q (W/m^2) varying only in x and/or y . Time varying heat fluxes to generate seasonal cycles is not appropriate in such an idealised set up. Another method is surface restoring where temperature/density is restored to a set profile in the uppermost layer. The initial set up will be using fixed surface heat fluxes, discussed in section 1.6. Buoyancy forcing will be discussed in much greater detail in chapter 3.

4. Wind forcing can be applied in a zonal and/or meridional direction. Again we have chosen to apply a fixed surface wind stress rather than time varying due the idealised nature of our model and for ease of interpretation. We use a fixed wind stress in order to generate an ACC to be described in section 1.6.

Bottom boundary conditions

As the Southern boundary will be a fixed wall and the zonal boundaries will be periodic. The last set of boundary conditions to be applied are those at the bottom of the domain.

1. Slip
2. Topography
3. Linear drag

1. The sides and bottom of the model must have a boundary condition defining the flow at these boundaries. Usually this is either: no slip or free slip. As the computational cost is not severely constrained, we use a no slip boundary condition which maintains zero flow at the boundary by adding in an additional source term in the cells next to the boundary.
2. The Southern Ocean has a continental shelf that helps maintain deep water formation and ridges that slow the zonal flow and enhance eddy activity. Topo-

graphy steers the ACC flow and generates standing eddies (steady-state meanders). The importance of these standing eddies is a topic sparking a lot of interest. If zonal means are used in the decomposition then it would appear the standing eddy component dominates in both idealised and realistic eddy-permitting models *Tréguier et al.* (2007). However observational studies *de Szoeke and Levine* (1981) suggest that there is no mean flow heat flux across depth averaged contours of temperature, this is only achieved by transient eddies suggesting the large scale dynamics in flat bottom models closely resemble the stream wise averaged models with topography. This would suggest the approach of stream-wise averaging should be used instead of zonal averaging in models with topography, but this a more complex framework to use so was often neglected in earlier studies: *Hallberg and Gnanadesikan* (2006); *Farneti and Delworth* (2010) leading to different results on the importance of standing eddies and as to whether they alter the stratification of the ACC, or just the path *Abernathay et al.* (2013). Studies that have investigated the effect of topography using a stream-wise framework *Viebahn and Eden* (2012) and (*Abernathay et al.*, 2013), investigating heat fluxes across the ACC, suggest the standing eddy component is not negligible and qualitatively effects the generation and distribution of transient eddies. For initial runs we use a flat bottom to reduce computational cost, as little zonal variation arises in the ACC. It should be noted that some topography runs must be used to validate the flat bottom runs and the possible missing effects must be considered. We also note the the lowermost overturning cell in our experiments with flat bottoms should not be interpreted as meaningful.

3. In the absence of topography, Hidaka's Dilemma must be considered (*Hidaka and Tsuchiya*, 1953). For a flat bottom scenario with zero bottom friction, zonal transport would scale only with viscosity, channel width and wind stress would generate an unrealistically large ACC. *Hidaka and Tsuchiya* (1953) showed the only way to generate a sensible sized ACC was either to alter viscosity or diffusivity to unreasonable values, or they found that that this can be mitigated by a no-slip

boundary condition and a linear bottom drag, which is the approach we use.

Advection schemes

There are many different options for advection schemes in the MITgcm for a variety of setups. These vary in computational cost and spurious numerical mixing (*Ilcak et al., 2012; Hill et al., 2012*). In preliminary experiments we investigated the most appropriate advection scheme. In general there are some schemes more appropriate for high resolution than for coarse resolution set ups and vice versa, with a higher order scheme being more appropriate for higher resolution. For propagating fronts, a flux limiting scheme must be employed. When the time step is limited by advection, then multi-dimensional non-linear schemes offer the most stability, however they reduce the ability to calculate accurately diffusion/dissipation. We investigated schemes 33; as in *Hogg (2010)*, 81 as in *Abernathay et al. (2011)* and advection scheme 7 as used in *Zhai and Munday (2014)*.

Advection scheme 33: A third order direct space time flux corrected scheme, for 5 km resolution this produced a slightly noisy tracer field and is perhaps not of high enough order for the increased resolution required in our experiments (twice the resolution used in *Hogg (2010)*). This scheme was considered when running the preliminary experiments to establish the most suitable northern boundary condition, as *Hogg (2010)* formed the basis of our enhanced diffusion experiments, the scheme was later checked in the sponge layer experiments as well.

Advection scheme 81: A Second order moment scheme based off ?. Has a significant increase (20%) in computational cost. This scheme is favoured in many studies of the southern ocean such as (*Abernathay et al., 2011; Abernathay and Cessi, 2014; Wolfe, 2014*) after *Hill et al. (2012)* showed a reduction in spurious diapycnal mixing.

Advection scheme 7: Seventh-order one-step method with monotonicity-preserving limiter OS7MP, *Daru and Tenaud (2004)* with modifications from Adcroft and Campin, (MITgcm support mailing list communications 2010), in many cases com-

pares adequately with the more computationally expensive scheme 81 *Ilcak et al.* (2012).

With diffusion set to zero in the interior and at high resolution the effects of spurious diapycnal mixing between OSMP7 and a Prather advection scheme are negligible for this study. Preliminary experiments not shown here showed no noticeable difference other than computational cost between advection scheme 7 and 81, motivating us to use scheme 7.

Mixing parameterisation

Some sub grid mixing must be included in order to maintain a stable mixed layer. In the MITgcm this can be achieved through a number of methods of varying complexity: Turbulent Kinetic Energy (TKE) , K-profile parameterization (KPP) and Convective adjustment. Many models employ the widely used KPP mixing scheme (*Large et al.*, 1994), which greatly enhances vertical diffusion in the upper 50 m as well as introducing a non-local transport term to represent convective transport, as all other convection parametrisations must be disabled in the model. KPP requires additional terms to be introduced into buoyancy budgets, in order estimate the diffusion term as well as careful and considered adjustment to ensure a sensible mixing. Convective adjustment (*Cox and Bryan*, 1984) is the most basic method of maintaining a stable mixed layer as it simply re stratifies statically unstable density configurations, convective adjustment is simpler to analyse than using KPP and requires little consideration on overall impact on the physics of the model. It can only be used in idealised models with reasonably coarse vertical resolution otherwise the computational cost of the iterative method of stabilisation would be too high and the mixing not sufficient. Studies comparing convective adjustment and KPP, such as *Boccaletti et al.* (2007), show only slight differences in EKE, which is the same order of magnitude for both, suggesting convective adjustment is adequate for the physics of an idealised model and offers the advantage of sim-

plicity. Although convective adjustment is a sensible choice for a highly idealised model, with finer vertical resolution or in a less idealised case such as the inclusion of topography, this method may not be suitable as evaluated in *Griffies et al.* (2000). The turbulent kinetic energy (TKE) scheme, described in *Gaspar et al.* (1990); *Madec and Delecluse* (1998), is another method, favoured in runs such as the NEMO ORCA models (*Kazantsev*, 2013). TKE requires no explicit convective scheme so allows for a more flexible model set up, offering an alternative to KPP where convective adjustment alone will not suffice. Given these considerations, for our starting model set up with a flat bottom we use the least complex mixing parameterisation: convective adjustment.

1.6 Channel model set up

Here we outline the basic model set up for a flat bottom channel to test the initial effects of closing the northern boundary. All subsequent models will be variants of the model outlined here and the specifics described in detail in the relevant chapters. An example python script generating the model grid and forcing is given in appendix. The initial channel domain is 1000km by 2000km and 2985m deep with a horizontal resolution of 5km with 30 geopotential layers ranging in thickness from 10m at the surface to 250m at the bottom. To allow for a small domain size and reduce computational cost the channel was setup with no topography as rationalised in *Abernathay et al.* (2011) (see section 1.5.2). To reduce spurious diapycnal mixing advection scheme 7 was chosen (*Hill et al.*, 2012; *Ilcak et al.*, 2012) which is a Seventh-order one-step method with monotonicity-preserving limiter scheme outline in *Daru and Tenaud* (2004). Convective adjustment was employed to maintain a stable mixed layer.

The model was forced using similar zonal wind stress sine bell, to *Abernathay et al.* (2011) to generate an appropriate ACC in a flat bottomed channel model to

generate an ACC.

$$\tau_s(y) = \tau_0 \sin\left(\frac{\pi y}{L_y}\right), \quad (1.64)$$

where L_y is the meridional width, $Q_0 = 10 \text{ W m}^{-2}$ and $\tau_0 = 0.2 \text{ N m}^{-2}$. The size roughly approximates observed surface wind stress *Large and Yeager* (2009). We

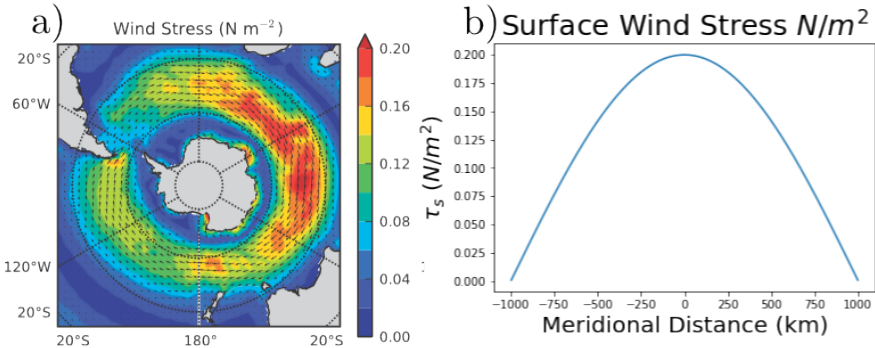


Figure 1.5: a) Taken from *Abernathay et al.* (2011) the net surface wind from CORE 2 (*Large and Yeager*, 2009). b) A simplified version of the observed surface wind stress used in our model.

also employed a similar heat forcing (fixed surface flux), however as the northern boundary is be fully closed so the surface heat flux has been adjusted so that there is no net cooling at the surface:

$$Q(y) = \begin{cases} -Q_0 \cos\left(\frac{18\pi y}{5L_y}\right) & \text{for } y \leq \frac{5L_y}{36} \text{ and } \frac{22L_y}{36} \geq y \geq \frac{30L_y}{36}, \\ -Q_0 \cos\left(\frac{18\pi y}{5L_y} - \frac{\pi}{2}\right) & \text{for } \frac{5L_y}{36} \geq y \geq \frac{20L_y}{36}, \\ 0 & \text{for } y \geq \frac{5L_y}{6}, \end{cases} \quad (1.65)$$

Surface buoyancy forcing in the southern ocean is poorly constrained, *Cerovečki et al.* (2011) so the buoyancy forcing applied is a simplification of the buoyancy loss/gains associated with AABW , the ACC and AAIW, roughly matching the CORE2 estimates from *Large and Yeager* (2009) Fig. 1.6.

Previous idealised channel models such as *Cerovečki et al.* (2009); *Cessi et al.* (2006) tried to model the Southern Ocean without representation of the rest of the global basins, which leads to a vanishingly small deep residual overturning circulation. *Abernathay et al.* (2011) used a sponge layer to relax the northern

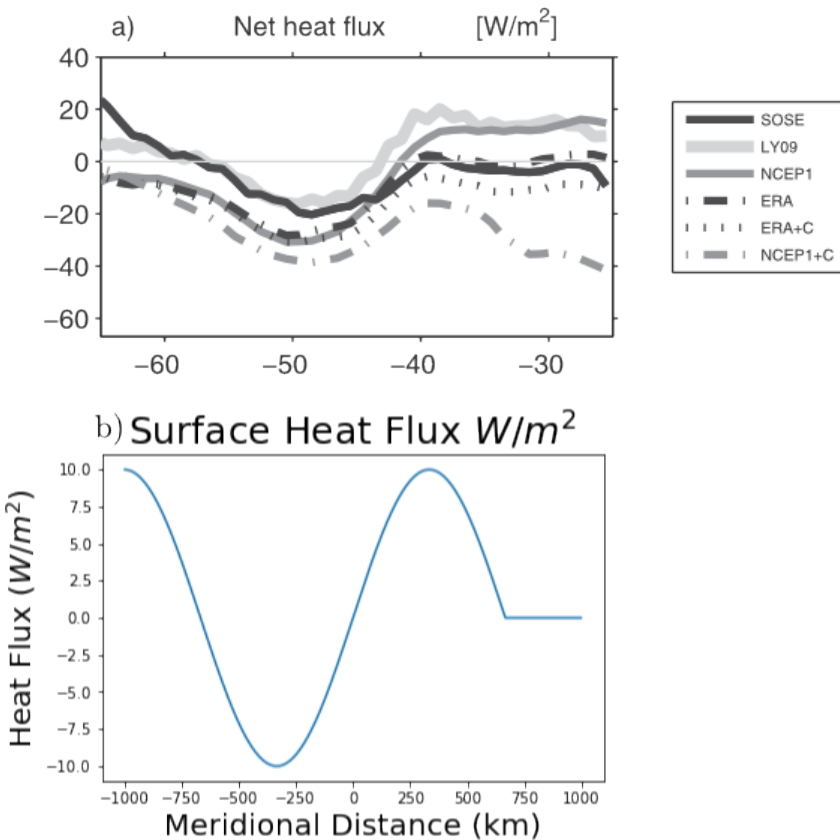


Figure 1.6: a) Taken from Cerovečki *et al.* (2011) the net surface heat flux from various estimates b) A simplified version of the LY09 line (*Large and Yeager*, 2009) to force our model in a simple cooling, heating, cooling pattern.

boundary temperature (T) profile to a prescribed temperature profile:

$$T^*(z) = \Delta T \frac{(e^{z/N} - e^{-H/N})}{1 - e^{-H/N}}, \quad (1.66)$$

assuming a natural stratification $N=1000\text{m}$ and a temperature difference (ΔT) of 8°C . This exponential is taken from Abernathay *et al.* (2011) based on modelling and observational studies (*Karsten et al.*, 2002; *Wolfe et al.*, 2008). This allows a return pathway for deep overturning that requires crossing of isopycnals to exist and is computationally inexpensive, allowing a small domain eddy resolving set up. The sponge is set using a mask (M_{rbcs}) of values between 0 and 1 (0 = no relaxation, 1 = relaxing on time scale $(\frac{1}{\tau_T})$). The tendency of temperature at each

grid point is modified to:

$$\frac{dT}{dt} = \frac{dT}{dt} - \frac{M_{rbcs}}{\tau_T}(T - T^*). \quad (1.67)$$

This is the basis for our channel model configurations. The first stage of our investigation is to understand what physical processes are altered when the northern boundary is closed and whether this is a step function response or a smooth transition. As this model is highly idealised, we use the results as a qualitative guide to provide insight on how to quantitatively and more definitively investigate this in the future.

Chapter 2

Diabatic eddies setting buoyancy forcing

This chapter focuses on the SO ROC response to closing the northern boundary condition in a highly idealised setting to understand the most basic fundamentals of this process and establish if in fact the SO ROC vanishes with a closed northern boundary.

2.1 Introduction

Changes to the Southern Ocean Residual Overturning Circulation (SO ROC) could have large effects on ocean circulation and climate, making it of great interest to understand what sets the strength and sense of the SO ROC. The upper cell of the SO ROC is closed outside the Southern Ocean connecting the surface branch with the deep branch (Fig. 2.1).

We look at this within a modelling context where a Northern boundary condition must be applied in order to close the SO ROC. In the framework of *Marshall and Radko* (2003) the SO ROC can be related to the effective buoyancy forcing in

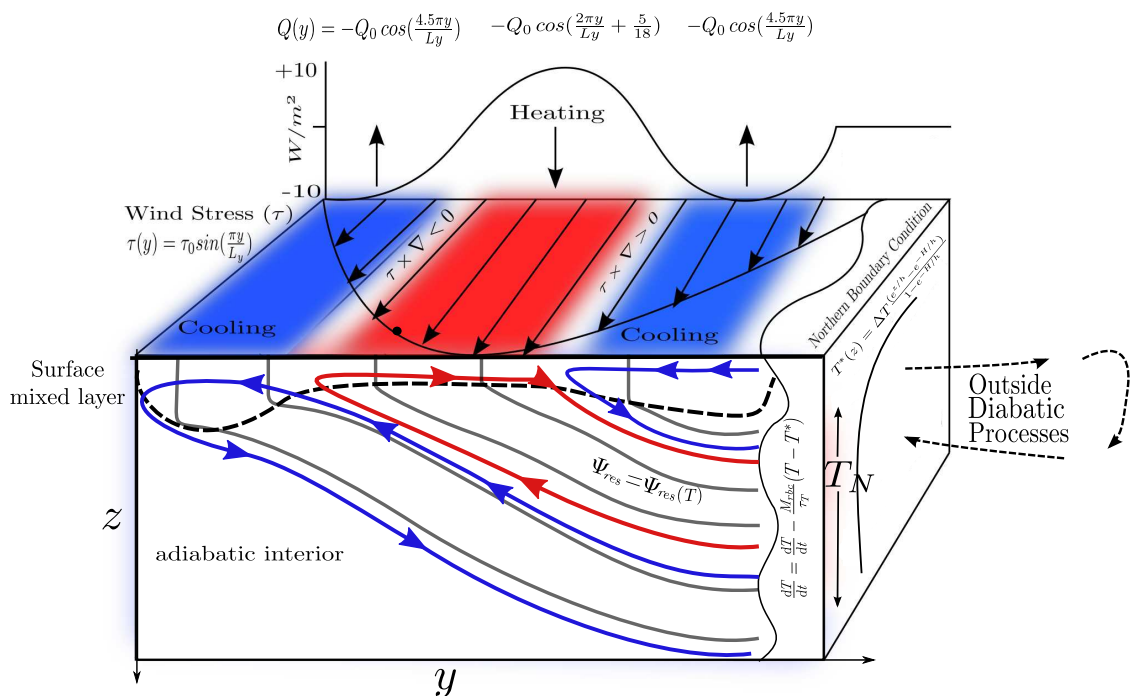


Figure 2.1: An illustration of the channel model configuration, showing the surface forcing and the sponge layer at the northern boundary, with the expected residual circulation from the surface forcing at short sponge relaxation time scales depicted. The SO ROC in coloured arrows is determined in the surface mixed layer, which in this configuration can be several hundred meters deep, and directed along mean isopycnals in the interior.

the Southern Ocean channel. However, without an open boundary the SO ROC cannot be maintained, implying that the effective buoyancy forcing in the Southern Ocean must go to zero. This part of the SO ROC circulation must be represented when considering the SO in isolation, *Marshall and Radko* (2003) argued that in the present climate the effective surface buoyancy forcing in the Southern Ocean is dominated by surface buoyancy exchange between ocean and atmosphere. If the Northern boundary of a channel model is closed then the buoyancy budget in the Southern Ocean needs to change. In a set-up of fixed surface fluxes and no diapycnal mixing (consistent with the adiabatic pole-to-pole circulation), either convective mixing, or diabatic eddy fluxes must increase to cancel the surface fluxes. This suggests the choice of northern boundary condition may have a large impact on the dynamics of the model impacting the outcome of any theory investigated.

Here we start in a very idealised theoretical framework considering the closure of the northern boundary. Specifically we show that the response in diabatic forcing in the mixed layer is achieved by diabatic eddy fluxes altering the effective surface buoyancy forcing. This is used as the initial starting point in our investigation before proposing other factors to investigate. Our first line of investigation is to establish if indeed the SO ROC ceases to exist when we close the northern boundary without altering the surface forcing and if that change is a step change or a smooth transition.

2.2 Theory

We investigate the overturning adjustments associated with changes in diabatic processes outside the Southern Ocean by considering an idealised channel model in which diabatic processes further north are represented through a diabatic sponge layer at the northern side of the channel. The diabatic forcing of the sponge layer is decreased by increasing the specified relaxation time scale in which the

stratification is restored to a prescribed profile. When the northern boundary condition is changed, we expect a response in the diabatic eddy fluxes, adjusting the net diabatic forcing in the surface mixed-layer to accommodate the change in diabatic forcing, and as a result in stratification, at the northern boundary. Also, because the unchanged winds will leave the Eulerian MOC unaffected, a change in the SO ROC must be accommodated by a change in the eddy-driven overturning. So, the change in eddy-driven overturning must be associated and consistent with a change in net buoyancy forcing in the diabatic mixed-layer. Here, we focus on how the time-mean heat budget is affected. To simplify the analysis we consider a model setup with a linear equation of state, equating buoyancy to temperature. Starting from the time mean heat budget we write:

$$\nabla \cdot \bar{\mathbf{u}}T = \frac{\partial Q}{\partial z}, \quad (2.1)$$

where Q is the heat supplied to the surface through air-sea fluxes and other diabatic processes like diapycnal mixing and convective overturning.

Starting from this time mean heat budget *Marshall and Radko* (2003) created a widely used diagnostic by decomposing the eddy fluxes into adiabatic and diabatic components and removing the diabatic eddy fluxes from the LHS of Eq. 2.1 to the RHS. The background theory for this is described this in detail in section 1.2.3 where we arrive at Eq. (1.49). Evaluated at the base of the mixed layer, below which the SO ROC is constant along mean isopycnals, the SO ROC is related to the diabatic forcing over the mixed layer. Putting Eq. (1.49) from *Marshall and Radko* (2003) in terms of temperature alone, as per our model's equation of state gives:

$$\Psi_{res}|_{hml} \frac{\partial T}{\partial y} = Q - \int_{hml}^0 \frac{\partial \left(\bar{v}'T' - \frac{\bar{w}'T'}{S_T} \right)}{\partial y} dz, \quad (2.2)$$

where Ψ_{res} is the SO ROC and $S_T = -\overline{T_y}/\overline{T_z}$ is the slope of mean temperature surfaces. *Marshall and Radko* (2003) showed that in most realistic cases the diabatic eddy contribution and other diabatic forcing terms are small compared with the surface forcing and that the SO ROC can be predicted from $Q = Q_{surflux}$, neglecting diapycnal mixing and convective overturning. As our motivation for this study is the idea of far field forcing altering the SO ROC we look to the role of northern boundary conditions in channel models. For a different stratification north of the ACC, the diabatic eddy component may become as important as the surface buoyancy forcing term, or deeper convective mixing in the SO channel must come into play. We will assume that the diapycnal mixing away from the bottom will remain negligible and will not affect the SO ROC upper cell and that diabatic eddy fluxes cannot be neglected. This could mean when setting up a channel model to evaluate the SO ROC response to altered surface forcing the fundamental dynamics may have been determined by the boundary condition applied to maintain a 3 cell SO ROC.

In some scenarios the diabatic eddy contribution to the heat budget may not be negligible and must be considered. To do this Eq. 2.2 must be reformulated to become compatible with the model equations. Part of this reformulation is due to the model's discretization, but another part is more fundamental. Some parts of the TEM theory used in *Marshall and Radko* (2003) use QG assumptions that are not appropriate in the surface mixed layer. When deriving Eq. (2.2) the QG stream function is represented by Eq. (1.37) which means the left hand side of Eq. (2.2) is appropriate for the base of the mixed layer and below. This makes the original TEM framework inappropriate to investigate the mixed layer. If we keep in a Cartesian framework and start from Eq. 2.1 and making a Reynolds decomposition the budget is split into eddy and mean transport terms:

$$\frac{\partial \overline{vT}}{\partial y} + \frac{\partial \overline{wT}}{\partial z} + \frac{\partial \overline{v'T'}}{\partial y} + \frac{\partial \overline{w'T'}}{\partial z} = \frac{\partial \overline{Q}}{\partial z}. \quad (2.3)$$

Traditionally the eddy fluxes are decomposed into an along \bar{T} component and a remaining horizontal component (*Marshall and Radko*, 2003). Here we decompose the transport terms into an along \bar{T} component and a remaining vertical component:

$$(\overline{v'T'}, \overline{w'T'}) = \underbrace{(\overline{v'T'}, \overline{v'T'}S_T)}_{\text{along } \bar{T}} + \underbrace{(0, \overline{w'T'} - \overline{v'T'}S_T)}_{\text{remaining vertical}}. \quad (2.4)$$

Diabatic eddy fluxes should be down the mean buoyancy gradient. Decomposing the eddy fluxes along isotherm and either a remaining vertical (done here) or horizontal (*Trégouier et al.*, 1997, as in). The two different decompositions makes differing assumptions about the mixed layer, the assumption in the tradition TEM configuration is as in Fig. 2.2.a whereas our assumption assumes a layer like Fig. 2.2.b (*Plumb and Ferrari*, 2005).

We have chosen to combine eddy flux vectors this way to make a direct comparison possible between diabatic forcing by surface heat fluxes and by diabatic eddies in the surface mixed layer:

$$\underbrace{\frac{\partial \bar{vT}}{\partial y} + \frac{\partial \bar{wT}}{\partial z} + \frac{\partial \overline{v'T'}S_T}{\partial z} + \frac{\partial \overline{v'T'}}{\partial y}}_{\text{Adiabatic advective fluxes } (\nabla \cdot \bar{\mathbf{u}_A T})} = \underbrace{\frac{\partial Q}{\partial z}}_{\text{air-sea fluxes}} - \underbrace{\frac{\partial (\overline{w'T'} - \overline{v'T'}S_T)}{\partial z}}_{\text{Diapycnal fluxes}} = \frac{\partial (Q - D)}{\partial z}, \quad (2.5)$$

with

$$D = \overline{w'T'} - \overline{v'T'}S_T \quad (2.6)$$

It is noted in *Plumb and Ferrari* (2005) that these "Raw" eddy fluxes contain reversible diapycnal mixing as well as irreversible mixing and will typically be much larger than the true irreversible diabatic eddy fluxes. The L.H.S will only represent the residual flux divergence when the flow is adiabatic below the surface mixed

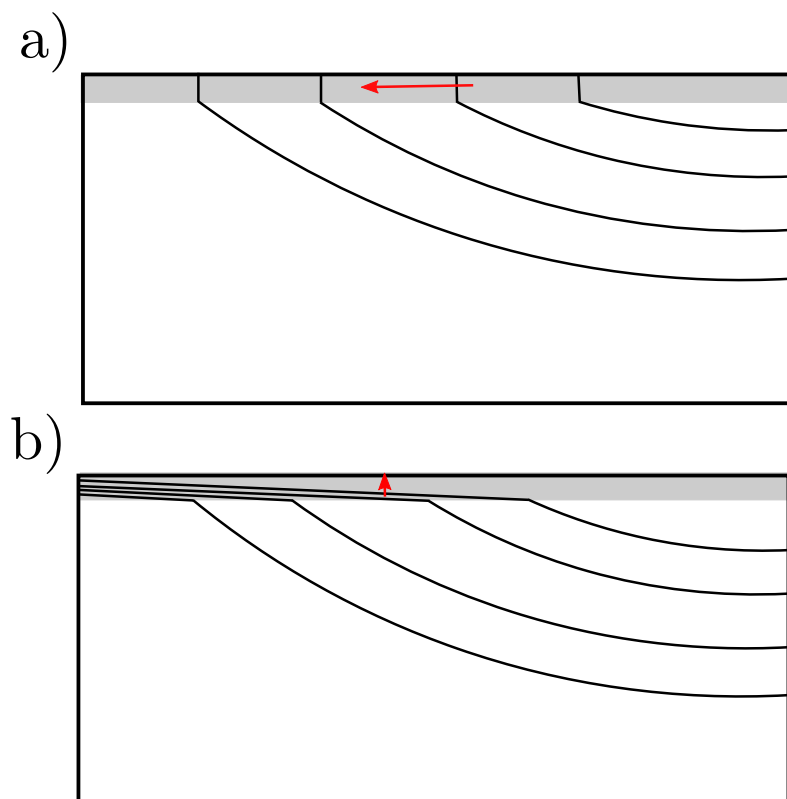


Figure 2.2: Mean isotherms in a hypothetical mixed layer (grey) showing a) assumed no vertical temperature gradient with purely horizontal diabatic fluxes and b) assumes isotherms are not vertical and an artificial thin layer where there is no along isothermal flow. adapted from *Plumb and Ferrari (2005)*

layer. In a Cartesian frame work these terms acts as approximations for the heat budget of diabatic eddies and adiabatic fluxes but will differ from the residual mean counter parts that require additional surface mixed layer assumptions (discussed in chapter 1) in order to calculate. When we refer to diabatic eddy heat flux divergence we acknowledge by this definition additional reversible fluxes will be included so these fluxes will be quantitatively larger than the true irreversible diabatic fluxes.

It should be stressed that the diabatic surface mixed layer, is the layer over which Q and D go to zero. This layer equals the depth of the (winter) convective mixing or (winter) mixed layer. In our model seasonality is excluded, but the mixed layer depth can still be O (100 m), or even O (1000 m) in some of the experiments we will discuss later in this chapter.

Tracer evolution by the SO ROC is purely advective (non divergent), so that:

$$\overline{\nabla \cdot \mathbf{u} T} = \overline{\mathbf{u}} \cdot \nabla \overline{T}, \quad (2.7)$$

This arises from the continuity equation:

$$\overline{\nabla \cdot \mathbf{u}} = 0, \quad (2.8)$$

In continuous equations if Eq. (2.8) is true then Eq. (2.7) must be true. This however, does not hold in a discrete model due to tracer and velocity grid alignment. In the MITgcm the part advection scheme FORTRAN routine generalises 1-D advection to 3-D by removing the local divergence flow separately in each dimension.

Using the identity:

$$v \frac{\partial Q}{\partial y} = \frac{\partial v Q}{\partial y} - Q \frac{\partial v}{\partial y}, \quad (2.9)$$

This indicates on a discrete model grid Eq. (2.7) would have to be written:

$$\overline{\nabla \cdot \mathbf{u} T} = \overline{\mathbf{u}} \cdot \nabla \overline{T} - \overline{T} \cdot \overline{\mathbf{u}}, \quad (2.10)$$

This has implications for transferring the continuous equations from *Marshall and Radko* (2003) to discrete equations. As a result, the divergence of heat transport cannot be formulated as advection by a (residual) stream function adequately in discrete equations. For this reason we will use the heat budget of Eq. 2.5 to diagnose the contribution by the residual circulation, diabatic eddies, surface heat fluxes, and remaining terms. The LHS of Eq. (2.5) is the advective transport and the RHS is the diapycnal divergent terms. The LHS will disappear when the circulation is adiabatic but however will be larger than the true irreversible diabatic transport.

From the derivation of the buoyancy budget put in a TEM frame work it can be noted that if the local buoyancy forcing is kept constant, in order for the heat budget (Eq. 2.5) to hold, there must be a response in the diabatic eddy heat flux if the residual circulation changes in response to changing northern boundary conditions. This is illustrated in Fig. 2.1 where the surface temperature gradient is related to the northern boundary stratification through geometrical arguments:

$$T(y) = T_N(z = yS_T), \quad (2.11)$$

so that

$$\frac{\partial T}{\partial y} = -S_T \left(\frac{\partial T_N}{\partial z} \right), \quad (2.12)$$

2.3 Model Setup

We use an idealised channel model setup similar to *Abernathay et al.* (2011) and *Zhai and Munday* (2014). The model is based off the set up described in section 1.6 and we give a brief overview of the exact set up used here. Key model parameters

Table 2.1: Model Setup for flat bottom fixed-surface flux experiments.

| Symbol | Description | Value |
|---------------|-------------------------------------|---------------------------------------|
| L_x, L_y, H | Domain | 1000 km, 2000 km, 2985 m |
| L_{sponge} | Length scale of sponge layer | 100 km |
| Q_0 | Surface heat flux magnitude maximum | 10 W m^{-2} |
| τ_0 | Max surface wind stress | 0.2 N m^{-2} |
| dx, dy | Horizontal grid spacing | 5 km |
| dz | Vertical grid spacing | 10-280 m |
| Adv Scheme | 7^{th} order centred | 7 |
| τ_T | Sponge relaxation time scale | 3-day - ∞ |
| r_b | Linear bottom drag parameter | $1.3 \times 10^{-3} \text{ m s}^{-2}$ |

are outlined in Table 2.1 and the setup is shown schematically in Fig. 2.1.

In modelling studies of the Southern Ocean, sponge layers can be used to provide a northern boundary condition representing outside processes that would maintain a background stratification, enabling the SO ROC to close (*Abernathay et al.*, 2011; *Abernathay and Cessi*, 2014; *Zhai and Munday*, 2014). By altering the relaxation rate of the sponge layer we can show how important the choice of the northern boundary condition is. We do this by changing the relaxation time scale τ_T of the sponge layer to impose a northern boundary condition of varying rigidity.

The northern boundary condition is altered by changing the relaxation time scale τ_T from days to years to decades to an infinite time scale (closed northern boundary). Short relaxation time scales strongly constrain the northern boundary stratification and the SO ROC to a circulation effectively determined by that stratification. Increased relaxation time scales provide only weak constraints allowing the stratification to free evolve leading to a breakdown of the SO ROC. When τ_T is set to infinity the northern boundary acts like a closed wall.

Each model run is spun up for 400-3000 years (depending on relaxation time scale) to reach equilibrium indicated by mean Kinetic Energy and SO ROC strength (significantly longer than *Abernathay et al.* (2011) due to the longer relaxation time scales used here). The model is then run for a further 100 years with results

averaged over this period ¹.

2.4 Overturning response

The motivation for this study is a) the conjecture that the SO ROC vanishes when the northern boundary is closed, irrespective of the surface forcing and b) that the SO ROC can be determined for all local forcing as we keep local fluxes constant but keep change the northern boundary condition. Before moving to a detailed evaluation of the processes involved, we test whether this is the case. A series of experiments were run varying the relaxation time scale τ_T in Eq. ?? from 3 days to a fully closed channel ($\tau_T = \infty$). The relaxation time scales used were: 3, 10, 30, 100, 1000, 3000, 10000 days and no relaxation ($\tau_T = \infty$). In this section, we show the results from 4 runs: a sponge layer with relaxation timescale of 3 ,300 and 300 days and a fully closed boundary. To allow us to establish if this is a stepped response or a smooth transition to SO ROC collapse.

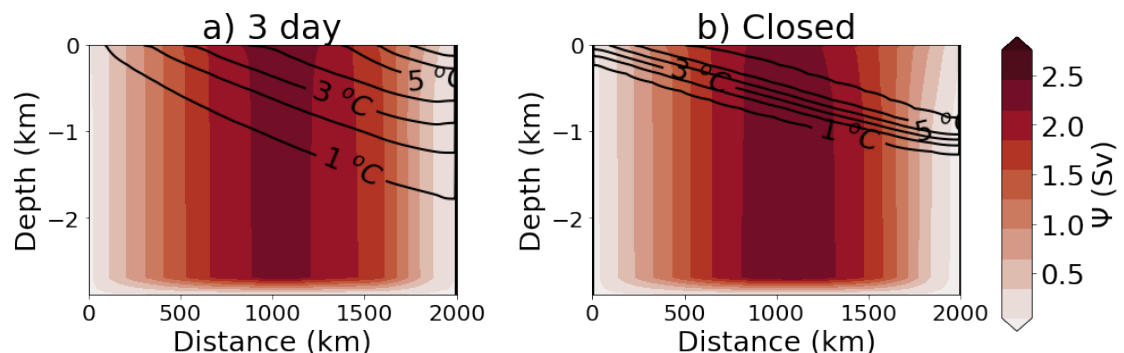


Figure 2.3: The Eulerian mean streamfunction ($\bar{\Psi}$), calculated from 100 years averaged velocities.

The Eulerian mean overturning stream function ($\bar{\psi}$) remains constant Fig. 2.3 (maximum ≈ 2.25 Sv, which scales to ≈ 60 Sv for a full channel) regardless of the northern boundary condition. This is expected as the Eulerian component is wind driven and throughout all our experiments the surface wind stress remains constant.

¹required to close the heat budget

We will not continue to show the Eulerian mean overturning in subsequent runs unless it differs from Fig. 2.3.

The SO ROC is calculated as an isothermal stream function² following the method of *Abernathay et al.* (2011):

$$\psi_{res}(y, T) = \frac{1}{\Delta t} \int_{t_o}^{t_o + \Delta t} \int_0^{L_x} \int_T^0 v h \, dT \, dx \, dt, \quad (2.13)$$

where $h = \frac{-\partial z}{\partial T}$ is the layer thickness in potential temperature (T) and the averaging period Δt is 100 years. The isothermal stream function is calculated over 42 discrete potential temperature layers shown in Fig. 2.5 and is remapped onto depth coordinates to give $\psi_{res}(y, z)$ shown in Fig. 2.4. When a short relaxation time scale of 3 days is applied the ROC features 3 distinct cells directed along mean isopycnals, reproducing the result of *Abernathay et al.* (2011). The SO ROC has a maximum of ± 0.75 Sv (30% of the mean) away from the surface. This is a realistic result as scaled to a full-length channel (approximately a factor of 25 times larger), a transport of 15 Sv would be obtained. This three cell structure disintegrates with increasing relaxation time scale and becomes virtually zero below the surface mixed layer when the northern boundary is closed (Fig. 2.4.d).

²A very good approximation for the residual stream function, but we note that this deviates from the complete ROC in the surface layers.

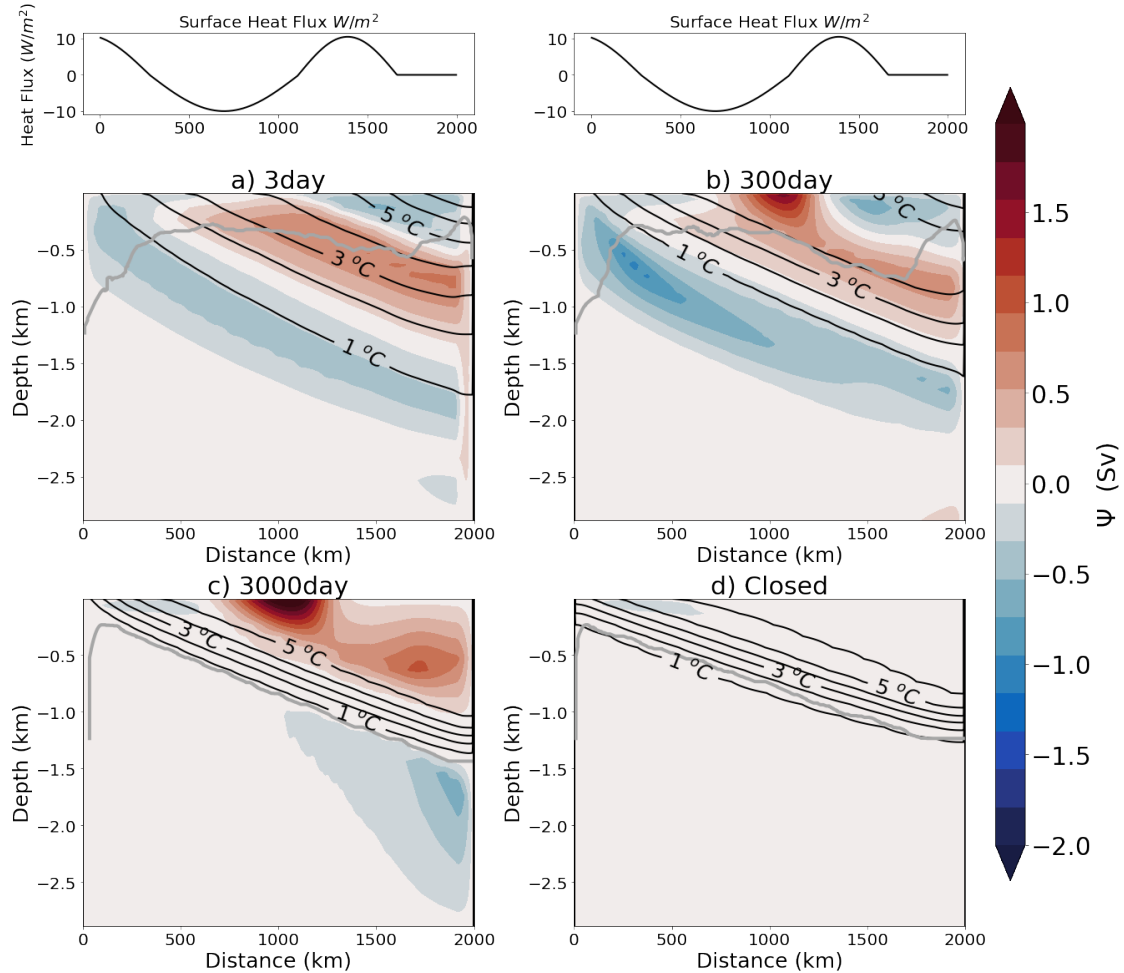


Figure 2.4: The isothermal stream function $\Psi_{res}(y, \theta)$ remapped onto depth coordinates, to give $\Psi_{res}(y, z)$ for a) $\tau_R = 3$ day and b) no relaxation. Isotherms in multiples of 1°C are overlaid as solid black contours. The surface heat forcing is displayed above.

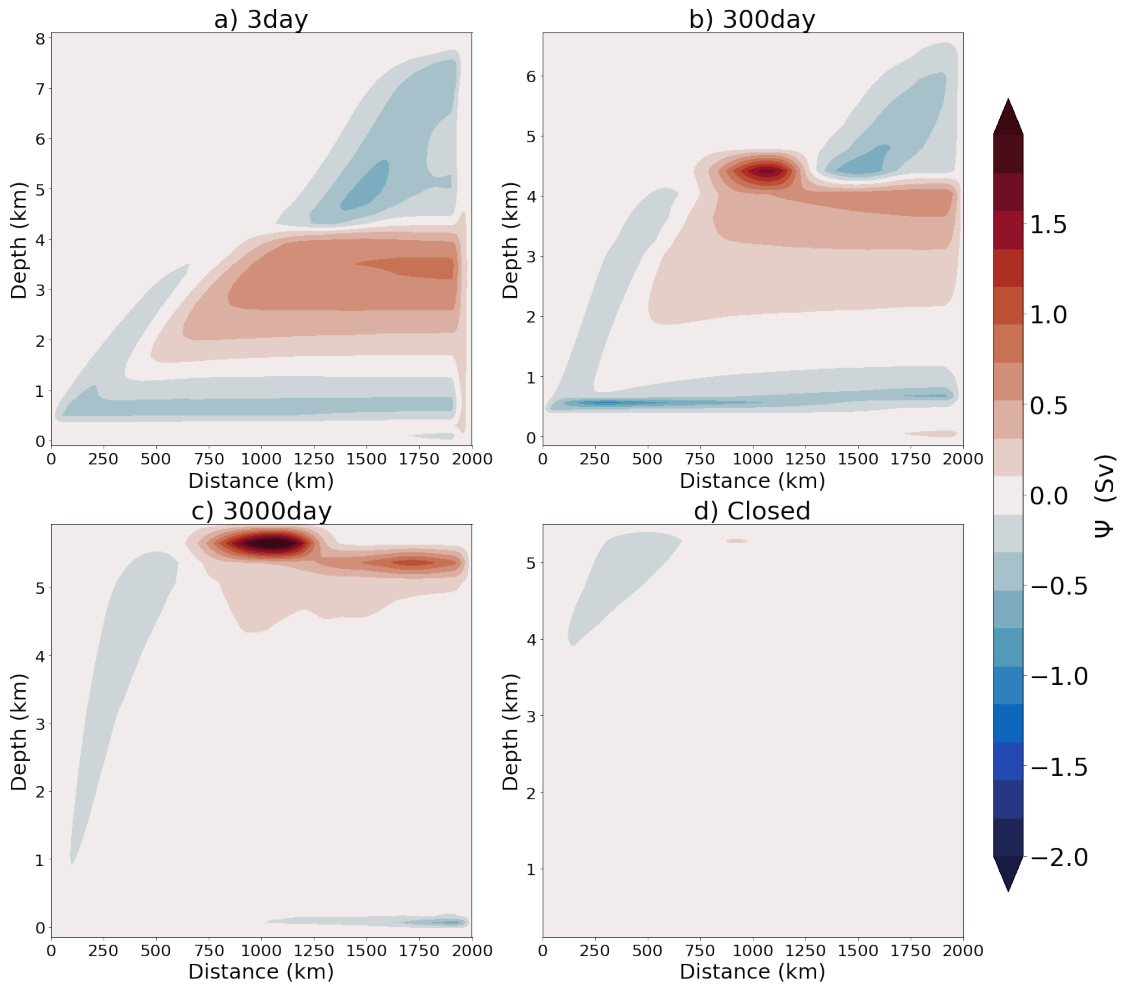


Figure 2.5: The isothermal stream function $\Psi_{res}(y, T)$ for a) $\tau_R = 3$ day and b) no relaxation.

When the northern boundary of the Southern Ocean is closed, there is a complete collapse of the SO ROC and very weak diabatic circulations remain that are completely confined to the surface mixed layer i.e. the depth of the convective overturning in the model. Below the surface mixed layer no circulation connected to the northern boundary can be maintained as there is no longer a means to close such a circulation away from the adiabatic interior. This underscores the SO ROC being part of an adiabatic pole-to-pole circulation (*Wolfe and Cessi, 2011*). When the circulation at the northern end collapses, the circulation at the southern end is doomed to disappear as well.

Fig. 2.4 shows that changing the northern boundary condition completely alters the domain-wide stratification and the diabatic layer-depth is increased with

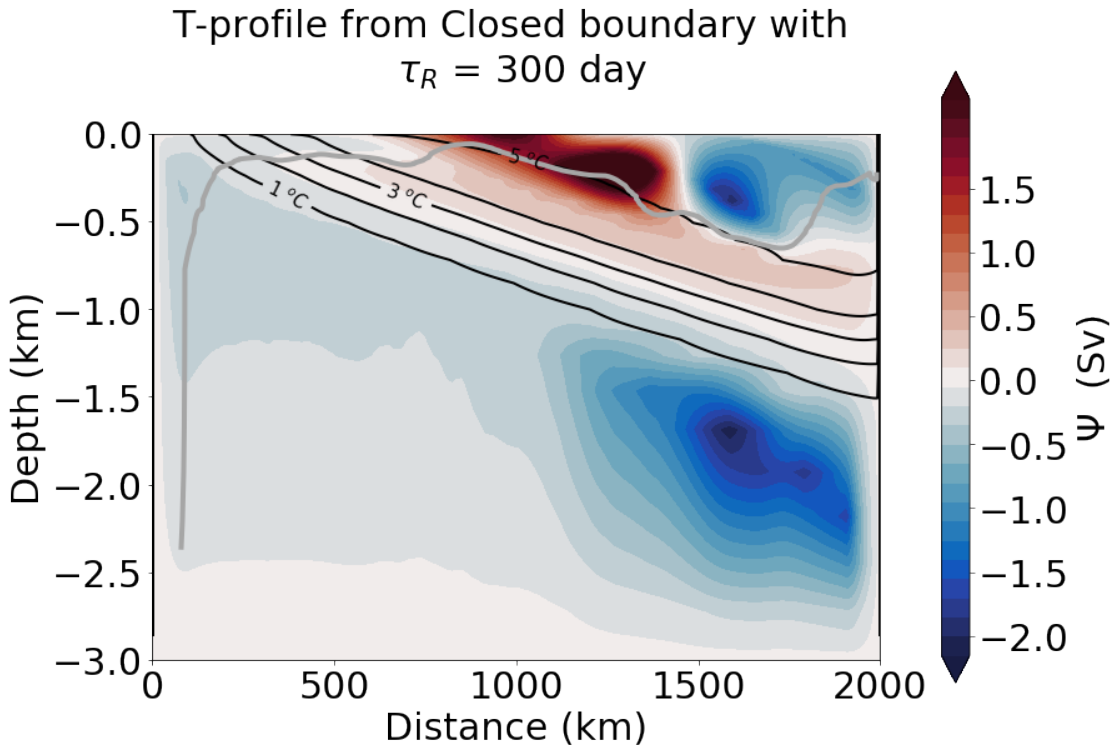


Figure 2.6: The isothermal stream function $\Psi_{res}(y, \theta)$ remapped onto depth coordinates, to give $\Psi_{res}(y, z)$ for a sponge layer relaxing to the closed boundary profile with a relaxation time scales of 300 days. Isotherms in multiples of 1°C are overlaid as solid black contours.

increasing τ_R . Short relaxation time scales show the top-to-bottom stratification of today's Southern Ocean, while longer relaxation time scales set up an alternate state with a large stratified surface layer and a sharp internal boundary layer (Fig. 2.4. c-d). The northern boundary stratification T_N also plays an important role in setting the isopycnal slope in the interior of the domain, which can be associated with a meridional buoyancy gradient allowing for the SO ROC. This result implies that not only diabatic eddy fluxes may cancel the surface heat flux in the mixed-layer, but also the role of convective mixing becomes more prominent and might be instrumental in collapsing the net surface forcing over the mixed layer. These results suggest that the SO ROC must be connected to the north of the domain in order to be maintained.

A question that arises is what is the cause of this collapse? Is it the change in stratification or the decrease in diabatic forcing in the sponge-layer? As a test

we ran an experiment where the stratification is restored on a three-day timescale towards the profile displayed in the closed boundary run (Fig. 2.4.d). With a medium 300-day relaxation time scale, the isotherm streamfunction produced is shown in Fig. 2.6. The stratification becomes inconsistent with the diabatic forcing in the sponge-layer, implying an unstable solution. A small perturbation from the prescribed profile due to an eddy, invokes a diabatic forcing term that drives the circulation further away from the prescribed profile. Using shorter relaxation timescales (3 days) results in an equally strong oscillating ROC that does not reach a steady state. These oscillations have peak to peak variations in total kinetic energy of 40% of the mean value, one to two orders of magnitude larger than in other spin-up runs. We conclude that the SO ROC is associated with net diabatic forcing and that the stratification associated with a collapsed SO ROC is inconsistent with net diabatic forcing. We address the impact of altering the boundary stratification and surface forcing systematically in chapter 3.

2.5 Heat budget

To assess if a collapse in the SO ROC is at least partly due to a response in the diabatic eddy heat flux divergence we now move to plotting the terms of the heat budget Eq. (2.5). The terms of Eq. 2.5 are plotted in Fig. 2.7. The difference between the thin grey line and the red line indicates the role of convective mixing and diabatic processes in the sponge layer. We also have included free surface correction term required due to the linear free surface boundary condition used in the model. This is calculated by:

$$\mathcal{T}_{surfcorr} = \frac{WTHMASS}{dz}, \quad (2.14)$$

where WTHMASS is the vertical mass-weight transport of potential temperature at the surface. Although included in the thin black line term to assess how well the

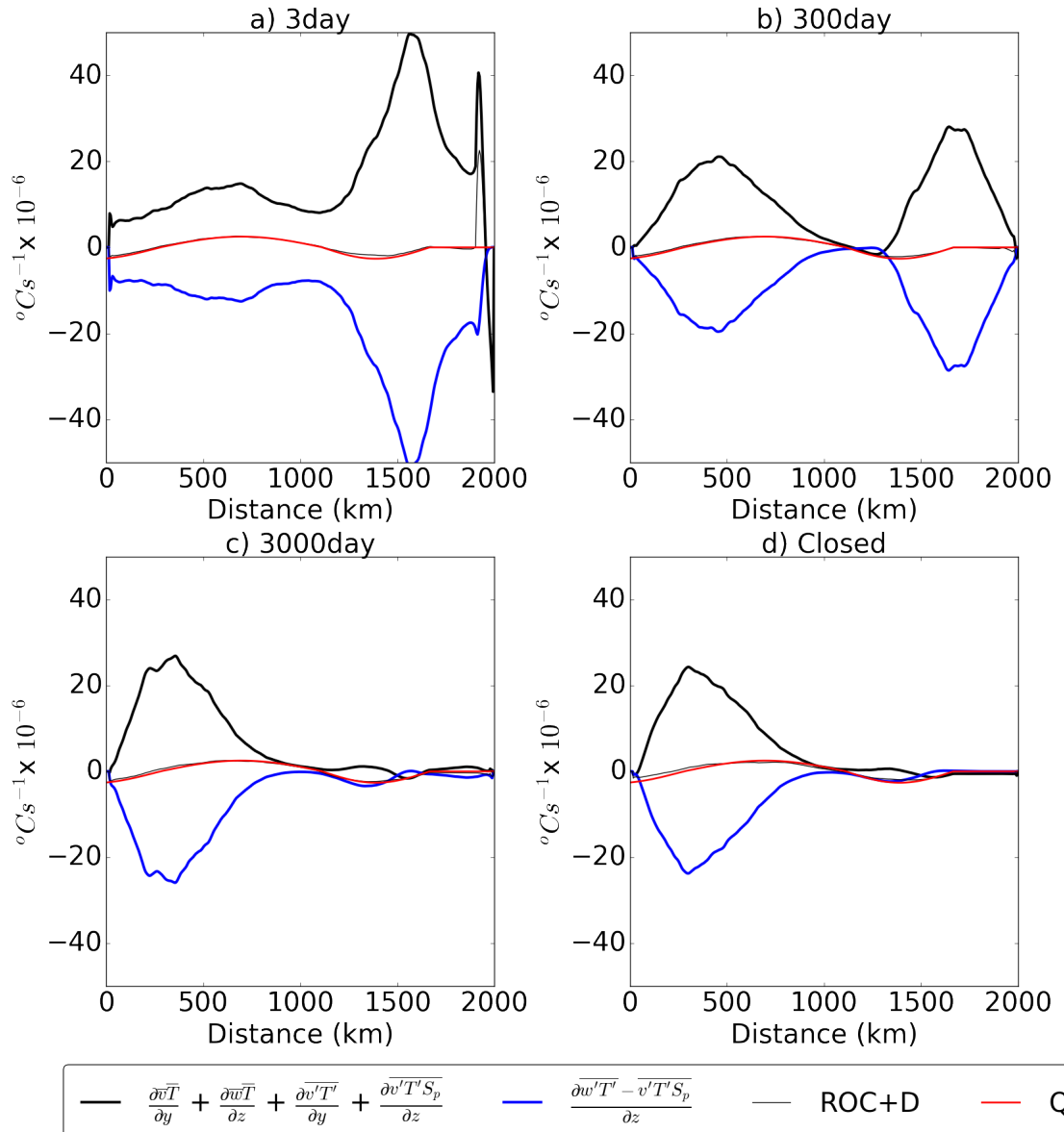


Figure 2.7: The components of the full depth buoyancy budget evaluated in as in Eq. 2.5. The advective transport component is show in black and diapycnal transport in blue, surface heat forcing in red and the total in thin black line.

heat budget closes, this term is $\mathcal{O}10^{-7}$, so essentially negligible being 1-2 orders of magnitude less than our flux divergence terms. We plot the LHS of Eq. (2.5) the advective transport head divergence term as the SO ROC heat divergence (below the surface diabatic layer) in black in Fig. 2.7 and the down gradient eddy heat heat flux divergence as our diabatic eddy term in blue, acknowledging these terms are larger than the real ROC/ diabatic eddy divergence terms. In all cases diabatic eddy heat fluxes nearly cancel the heat transport by the adiabatic ROC, with the surface heat flux being a small residual. These results suggest that for this set up there is no regime where diabatic eddy heat fluxes can be neglected in the budget of Eq. 2.2. In the northern 75% of the domain the heat transport by the ROC gradually decreases with increasing restoring time scale, until in the closed basin case heat transport divergence by the ROC drops to zero and the diabatic eddy fluxes almost exactly cancel the surface forcing. In the southern part of the domain a surface confined ROC cell remains and here the diabatic eddy fluxes at first order cancel the heat transport accomplished by this residual cell. Changes in convective mixing are negligible in affecting the net surface forcing over the surface mixed layer. Figure 2.7 highlights the changing diabatic eddy heat flux divergence and indicates the role of diabatic eddies in redistributing heat. However, as this figure shows the depth integrated divergence, we do not see the full spatial pattern. To investigate the distribution of the diabatic eddy heat flux divergence with depth, we plot the zonally averaged diabatic eddy heat flux divergence in latitude-depth space revealing the full extent of the diabatic eddy heat flux divergence changes (Fig. 2.8).

The figure reveals that the magnitude of the diabatic eddy heat flux divergence/-convergence is increasing almost everywhere with increasing relaxation timescales. The diabatic eddy heat flux divergence/convergence disappears where there is adiabatic flow, however this is not the true diabatic eddy heat flux convergence simply the down temperature gradient diapycnal fluxes. Large changes in the heat redistribution occur in the upper 1250 m. The depth over which the diabatic eddy

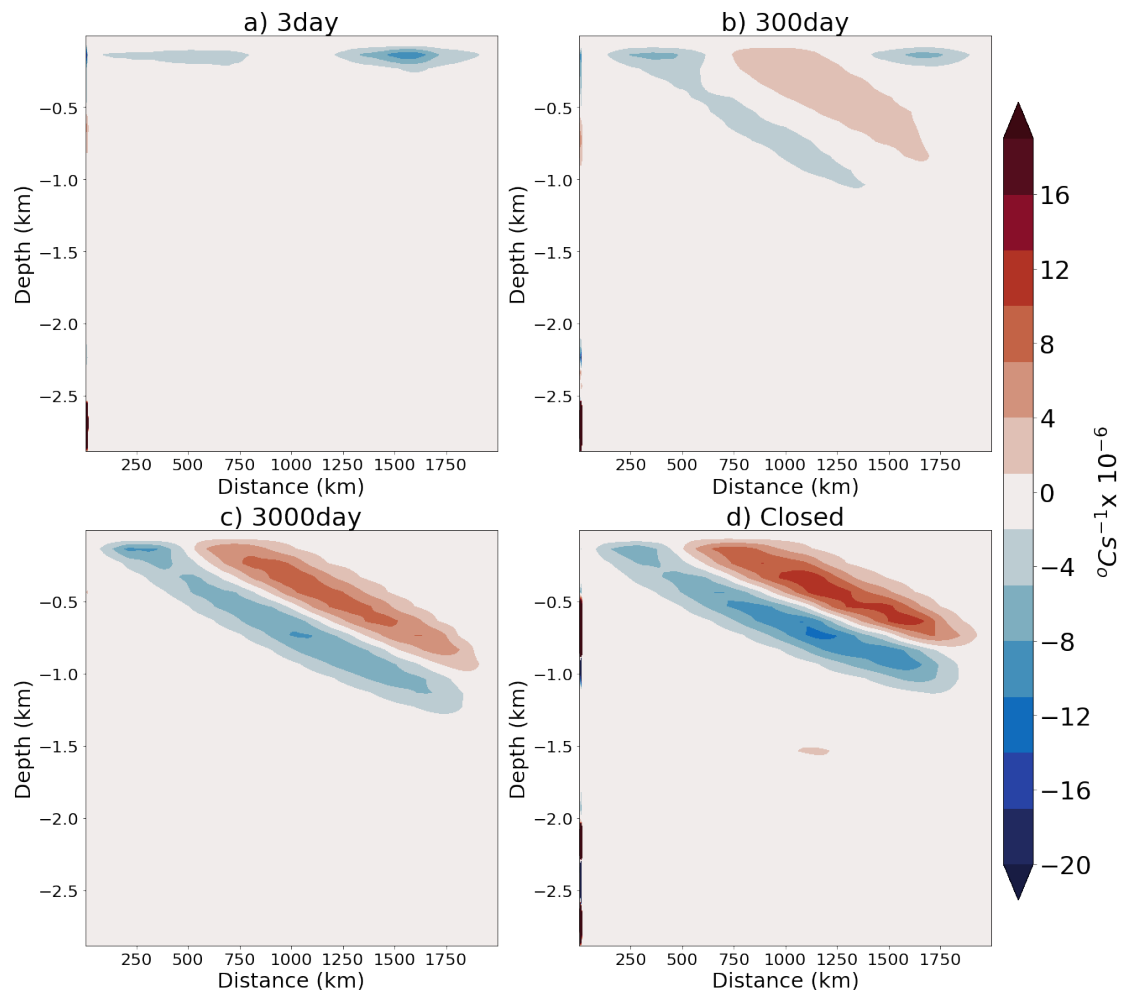


Figure 2.8: Zonal mean diapycnal heat divergence for relaxation timescale 3, 300, 3000 days and no relaxation.

fluxes are significant increases with increasing mixed layer depth as the relaxation time scale increases. Also the magnitude of the heat flux divergence increases, but at the bottom of the mixed layer a dipole pattern arises, which contributes little to the integral over depth. The diabatic eddy heat fluxes remove heat from the bottom of the mixed layer and transport it to the middle of the mixed layer layer, allowing for the creation of a sharp internal boundary layer, as seen in Fig. 2.4b, and a deep surface mixed layer. Heat transport by the ROC (Fig. 2.9) is doing the opposite, bringing the heat downwards. At the southern end, the diabatic eddies cool everywhere, opposing the heating by the surface confined ROC. At the northern end, a large area arises with weak heat convergence in the upper part of the mixed layer, with heating at the bottom due to diabatic eddies, opposing cooling by the ROC. Although the SO ROC nearly collapses, within and across the surface mixed layer a weak cell remains that is associated with non-negligible heat transport due to the increased vertical gradient in temperature. From these figures it is clear that changes in the northern boundary condition lead to large changes in the effective surface heat forcing through a diabatic eddy response. To further understand this adjustment we must consider what sets the strength of the diabatic eddies.

It should be noted that the increase in diabatic eddies is accompanied by a decrease of the vertically integrated diabatic eddy heat flux convergence, compare Figs. 2.7d and 2.8d. This occurs as the diabatic eddy heat flux convergence appears to be more and more as a perfect dipole pattern when the diabatic forcing in the sponge layer decreases. After establishment of an internal boundary layer, the diabatic eddies are associated with heating and equally large cooling in the upper and lower half of the internal boundary layer, respectively, the surface-confined ROC is associated with the opposite pattern.

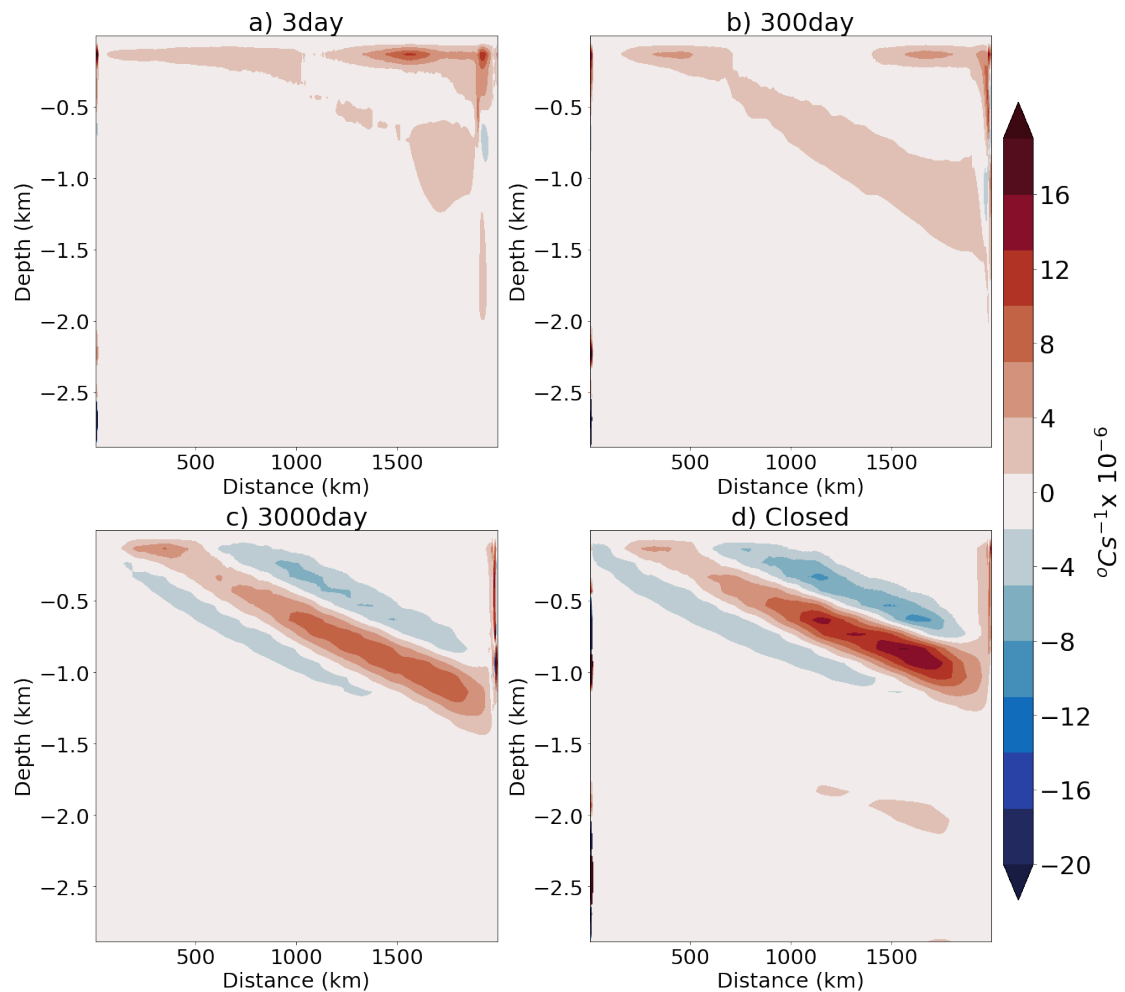


Figure 2.9: Zonal mean Adiabatic heat divergence for relaxation timescale 3, 300, 3000 days and no relaxation.

2.6 Controls on diabatic eddies

Having found a significant response in the diabatic eddy heat flux divergence, it is now important to understand what establishes this response. The controls on diabatic eddy flux divergence can be thought of as being made up of an eddy velocity perturbation v' , and a temperature perturbation T' . A relative measure of v' can be obtained by taking the square root of the eddy kinetic energy (EKE) and a measure for T' can be obtained from taking the square root of the eddy potential energy (EPE) (*von Storch et al.*, 2012). *Gill et al.* (1974) noted that changes in stratification in the upper few hundred meters can lead to large changes in stability properties; decreasing stratification leads to greater conversion from potential energy to kinetic energy i.e. increased baroclinic instability (*Legg and McWilliams*, 2001). This is exactly what we see happening when the diabatic forcing in the northern sponge layer decreases.

Figure 2.10 shows the zonally averaged EKE, with isotherms overlaid in black, and a thick grey line to indicate the mixed layer depth. Both the mixed layer depth and EKE increase, leading to large increases in diabatic eddy heat transport when the relaxation time scale in the sponge layer is increased. In the 3-day τ_R mixed layer depth is almost similar to the 300 day relaxation timescale layer depth, but once an internal boundary layer starts forming in the 3000-day and closed-basin runs, the mixed layer deepens and EKE increases. A redistribution in EKE occurs, decreasing in the north of the domain and increasing in the south and at depth, a pattern that we also observe in the diabatic eddy heat flux divergence in Fig. 2.8. As relaxation time scales increase to orders of tens of years and in the closed northern boundary case, a sharp increase in EKE with decreasing stratification occurs, in agreement with *Gill et al.* (1974). The change in mean kinetic energy between the runs is an order of magnitude smaller and the increase in EPE in Fig. 2.11 is qualitatively similar to the change in EKE.

When considering kinetic energy we see a very clear trend of increasing KE and

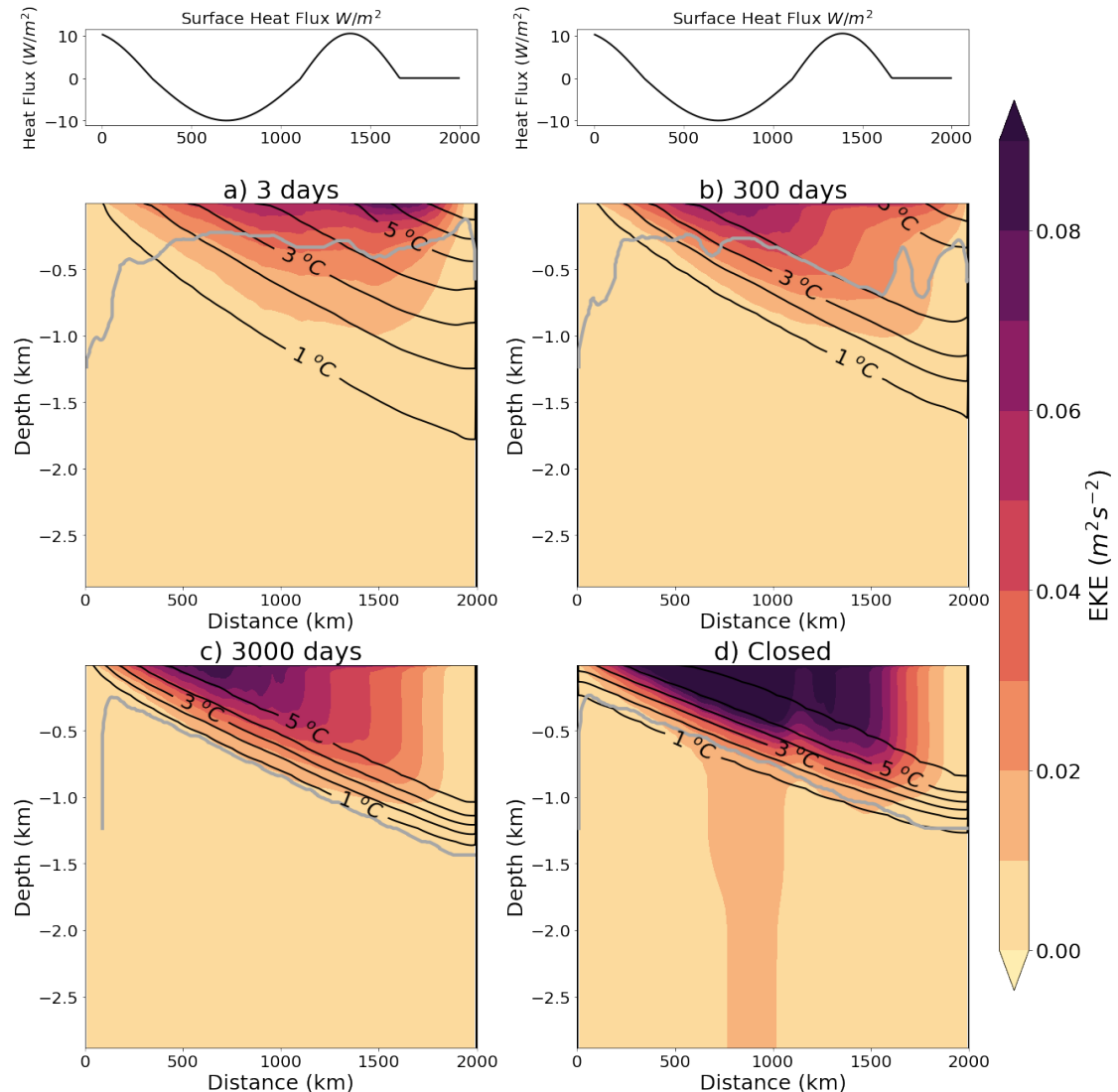


Figure 2.10: EKE $\frac{1}{2}(u^2 + v^2)$ for relaxation time scales of 3, 300, 3000 days and no relaxation. Isotherms in multiples of $1^\circ C$ are overlaid as solid black contours. The light grey contour indicates the mixed layer depth. Above the surface heat forcing is displayed.

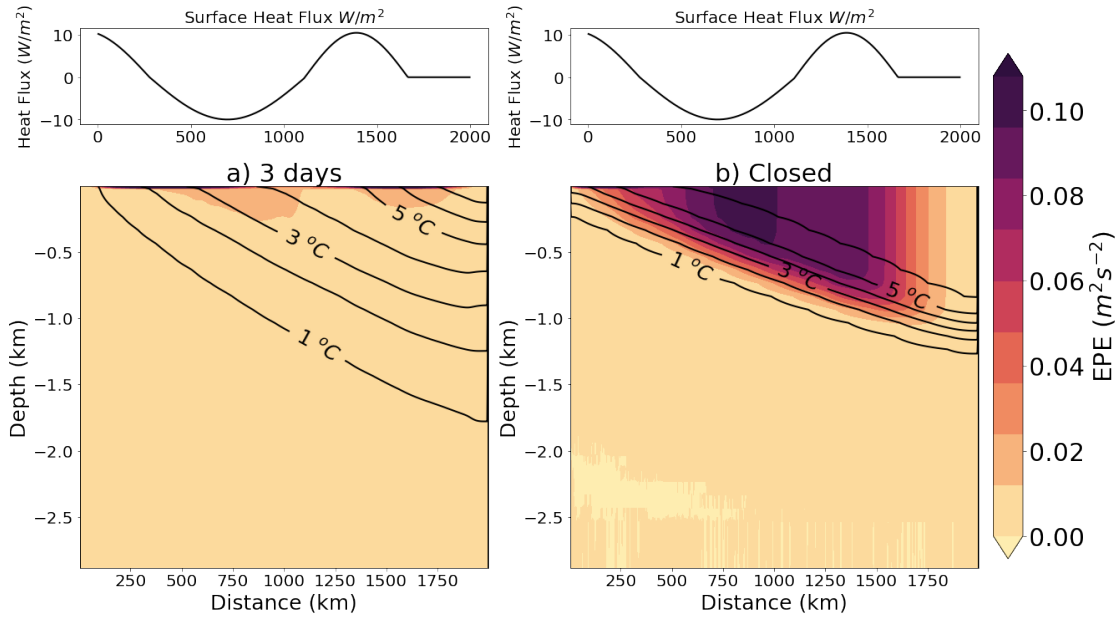


Figure 2.11: $\text{EPE} = g' T'^2 dT^*/dz$ for relaxation time scales of 3 days and no relaxation. Isotherms in multiples of 1°C are overlaid as solid black contours. Above the surface heat forcing is displayed.

EKE with increasing relaxation time scale. Again this is almost a step wise response increasing drastically between 300 days and 3000 days. Fig. 2.12 shows a) the average increase in EKE corresponding to b) the increasing domain integrated KE. The increase in Kinetic energy is almost entirely confined to the EKE component.

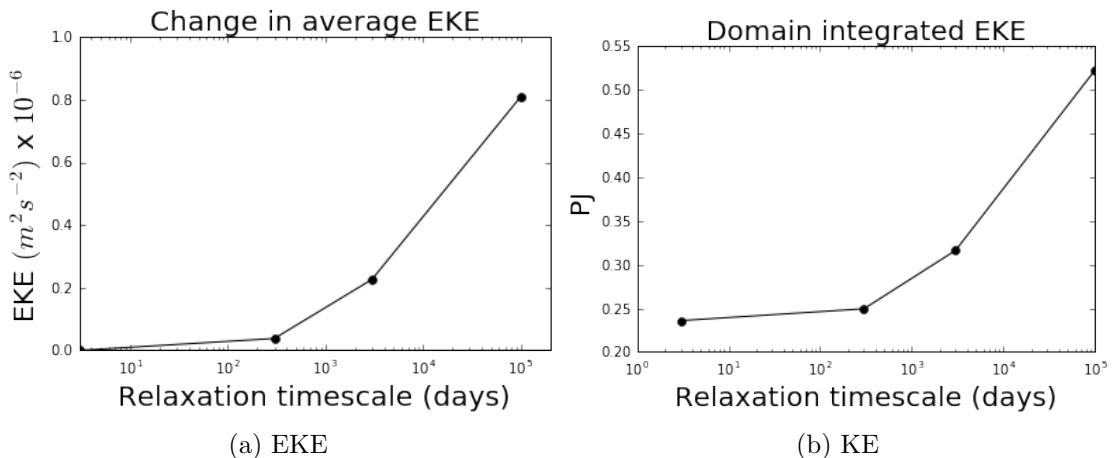


Figure 2.12: Change in kinetic energy

2.7 Conclusions

The diabatic eddy heat flux divergence strongly responds to changes in the northern boundary condition, becoming larger (increasing by 250% in amplitude) when the stratification at the northern boundary is better able to freely evolve and is less constrained by the circulation and diabatic processes in the sponge layer. The resulting changes in diabatic forcing lead to a dramatic increase in surface mixed layer depth, which leads to enhanced baroclinic instability and larger EKE and EPE. This result is qualitatively robust to the surface boundary condition, but when surface restoring is applied instead of a flux formulation, a much smaller increase in diabatic fluxes occurs and the EKE is more constrained. Nevertheless, the role of diabatic eddy fluxes in the vertically integrated heat budget is equally large for both surface boundary conditions. It appears that the diabatic eddy heat flux divergence is sensitive to both the strength of the surface heat flux and the diabatic forcing in the sponge layer, but also to the surface boundary condition for temperature (buoyancy).

When the northern boundary is closed there can be no interior residual overturning circulation (where $\Psi_{iso} = \Phi_{res}$), although we see here Ψ_{iso} reduces to near zero that is not necessarily a requirement. In the absence of diabatic forcing elsewhere the residual circulation will be confined to the surface mixed layer determined by surface heat fluxes and diabatic fluxes. When diabatic forcing becomes stronger in the sponge layer, the upper cell in the SO gains amplitude and becomes comparable to the observed SO ROC (and AMOC). In this regime the diabatic eddy heat flux divergence is always of first order importance, counteracting the heat transport by the ROC, leaving the surface forcing as a smaller residual. We did not find any regime where diabatic eddy fluxes can be neglected.

The vertical integral of the diabatic eddy heat flux convergence decreases by an order of magnitude for weaker diabatic forcing in the sponge layer. Using fixed fluxes these changes are reconciled by the establishment of a strong internal bound-

ary layer with a large vertical temperature gradient. As a result, both heat transport divergence by a weak ROC confined to strong northward deepening mixed layer, and the diabatic eddy heat flux divergence appear as dipoles of opposing signs. For the diabatic eddy fluxes heat convergence in the upper half of the internal boundary layer and heat divergence in the lower half occurs, while the heat transport divergence associated with the ROC in the mixed layer shows the opposite. Without diabatic forcing in a northern boundary sponge layer diabatic eddies cancel the effective surface buoyancy forcing, while the heat transport divergence by the ROC integrates to zero in the vertical. As a result, below the surface mixed layer the SO ROC completely collapses, because the connection to an adiabatic pole-to-pole circulation ceases to exist.

The upper cell SO ROC collapses when diabatic forcing in the northern sponge-layer is absent. These results underscore the interhemispheric link between the SO ROC and the northern hemisphere AMOC. Such links were previously demonstrated in *Gnanadesikan and Hallberg* (2000) and *Wolfe and Cessi* (2011). Here, by altering the northern boundary condition we showed how the SO ROC adjusts to changes in stratification at the northern end of the SO. Although some gradual changes can be seen with increasing relaxation timescale, this is more a stepped response between turning on or off the sponge layer when using relaxation timescale as the variable.

It should be stressed, however, that the representation of the far-field forcing, i.e. NADW formation, by a sponge layer with a prescribed e-folding stratification is crude and should be tested against other ways of closing the SO ROC. Nevertheless, the absence of far-field forcing implies a disconnect between the SO ROC and the AMOC, and our results imply that in this case the upper cell of the SO ROC cannot be maintained. The large changes in out diapycnal fluxes indicate that diabatic eddy heat fluxes could play a crucial role in the adjustment process to such changes highlights the need for a carefully designed diabatic eddy representation in the surface mixed layer of the ocean, which should also depend on the atmospheric

state and forcing. Our results also imply that although there is a significant step between the reduced diabatic forcing in sponge layers with relaxation time scale of under a year and multiple years there are already changes in the dynamics of a channel model before we see the full destruction of the SO ROC.

Chapter 3

Altering the surface boundary condition

3.1 The influence of the surface forcing formula-tion.

Introduction

Thus far we have tested the conjecture that altering diabatic processes outside the Southern Ocean through altering a relaxation time-scale in the sponge layer affects the SO ROC through a change in diabatic eddy fluxes. However, in an altered climate scenario that would lead to such large changes in diabatic forcing e.g. NADW production ceasing we would anticipate a response in the surface fluxes (*Wunsch and Ferrari, 2004; Gnanadesikan, 1999*). The southern ocean with its unique dynamics and weather systems may have a complex set of feedbacks and interactions in a changing climate. When considering the effects of changing altered buoyancy forcing, we must investigate the possible mediators of the response to altered stratification north of the ACC, represented by our northern boundary condition. The

SO Sea Surface Temperature (SST) response and feedbacks to changing climate has many uncertainties (*Hausmann et al.*, 2016; *Ferreira et al.*, 2015) and estimating the air-sea flux from the bulk formulas subject to changing basic variables (*Cerovečki et al.*, 2011). It is, therefore, useful to consider a number of different surfacing forcing scenarios in order to enable us to consider various possibilities. Buoyancy fluxes arise from contributions of heat and freshwater fluxes (*Gill*, 1982). A positive buoyancy flux implies decreasing ocean surface buoyancy flux associated with either cooling SST or increase in Evaporation minus Precipitation (E-P). As our experiments do not have varying salinity we can consider the approach of *Moore, GWK and Renfrew* (2002) which expresses buoyancy and freshwater fluxes as heat-equivalent fluxes:

$$Q_{BF} = Q_{HF} + Q_{FW} = \frac{\rho_0 c_p}{g\alpha} B \quad (3.1)$$

This allows us to consider fixed surface heat fluxes as larger contributions from Q_{HF} and surface restoring boundary conditions larger contributions from Q_{FW}

First, we compare our fist set of experiments using fixed surface heat fluxes with a similar set up using surface restoring used in *Abernathay and Cessi* (2014). These comparisons should give us some insight on the relevant next line of investigation to further access the role of the surface boundary condition.

3.1.1 Set up

To assess the sensitivity to the choice of a fixed flux boundary condition instead of a fixed surface air temperature with a restoring surface condition, a further four experiments were run using the surface forcing similar to *Abernathay and Cessi* (2014) (AC14), where the surface temperatures are relaxed to a linear meridional temperature gradient:

$$\theta = \Delta(\theta \frac{y}{Ly}), \quad (3.2)$$

where $\Delta\theta = 8^\circ C$, with τ_R set to 30 days (*Haney*, 1971). We ran two experiments with this surface restoring condition, one with a 3 day relaxation time-scale in the sponge layer, and one with a closed northern boundary. We then diagnosed the surface heat fluxes arising from the surface restoring condition and ran 2 more experiments with the diagnosed surface heat fluxes fixed. To enable us to compare with *Abernathay and Cessi* (2014) the surface restoring runs were done implementing the KPP scheme rather than using convective adjustment.

3.1.2 Influence on overturning and diabatic eddies

Figure 3.1a shows the closed flat bottom run forced with surface restoring, generating a weak overturning cell in the upper 250 m similar to that noted in *Abernathay and Cessi* (2014) due to the diabatic effects in the surface layer. However, if we diagnose the surface heat fluxes from this experiment and apply those as a fixed surface heat flux we obtain an almost vanishing SO ROC with a much deeper mixed layer and a sharp internal boundary as in our initial experiments shown in Fig. 3.1b and c. The diagnosed heat fluxes, however, are very weak in comparison with the 10 Wm^{-2} fluxes used in the first set of experiments at less than 1 Wm^{-2} . This indicates that the surface restoring generates a different and also much weaker diabatic forcing. By including a strong sponge layer we can further test the impact of the surface forcing condition on the diabatic forcing of the SO ROC. Fig. 3.2 shows the ROC for the different surface heat forcing conditions when the sponge layer is active. Fig. 3.2a shows a weak 2-3 cell ROC when forced with a surface restoring profile. The surface cell is weaker than when using a closed wall (Fig. 3.1a), but below the surface, a SO ROC is present, albeit weaker than in the first set of experiments. When replacing the surface restoring condition with fixed surface heat fluxes the SO ROC remains very similar (Fig. 3.2b). It is much weaker than in our first set of experiments, consistent with the weaker heat fluxes used. Note that the amplitude of the heat flux forcing in the first set was motivated in *Abernathay et al.*

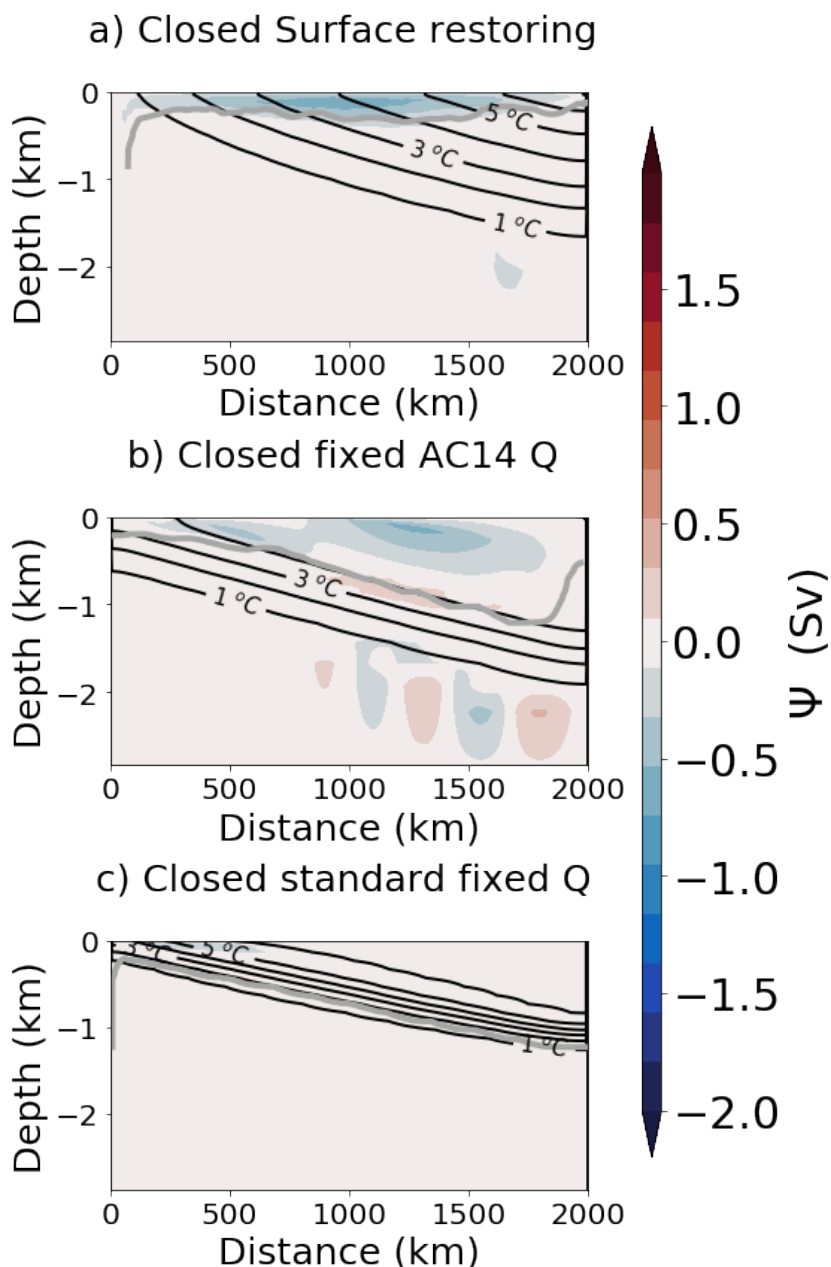


Figure 3.1: The isothermal stream function $\Psi_{res}(y, \theta)$ remapped onto depth coordinates, to give $\Psi_{res}(y, z)$. Isotherms in multiples of 1°C are overlaid as solid black contours.

(2011) by the observed heat fluxes over the Southern Ocean and that the diagnosed heat fluxes from applying the surface restoring condition appear too weak.

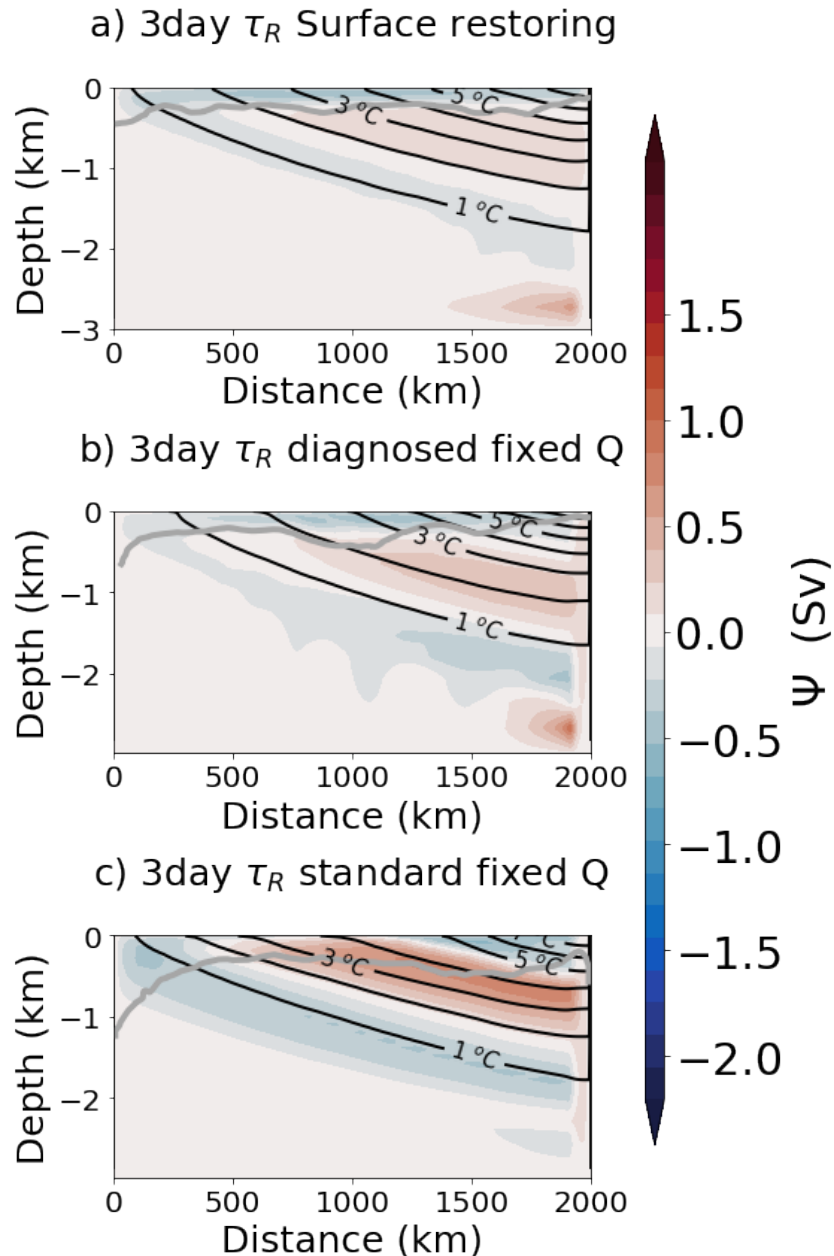


Figure 3.2: The isothermal stream function $\Psi_{res}(y, \theta)$ remapped onto depth coordinates, to give $\Psi_{res}(y, z)$. Isotherms in multiples of 1°C are overlaid as solid black contours.

We can deduce from these figures that the northern boundary is responsible for the sense and existence of the SO ROC, but that the local overturning strength is moderated by the surface heat forcing over the Southern Ocean.

To investigate whether the surface forcing conditions affect the driving mechanisms for changes in diabatic eddy heat flux divergence when the northern wall closes, we performed a heat budget analysis and plotted the diabatic eddy heat flux divergence in depth space. When a short relaxation timescale sponge layer is present all runs feature a similarly weak diabatic heat flux divergence, slightly increasing when the surface fluxes become stronger (not shown). The closed boundary runs display larger differences, but these are mainly quantitative. All runs feature an increased diabatic eddy heat flux divergence as well as an increase in mixed layer depth over which these fluxes occur. The dipole just above and below the bottom of the mixed layer, however, only develops when fixed fluxes are used, but appears more prominently when these fluxes are larger (Fig. 3.3a-c).

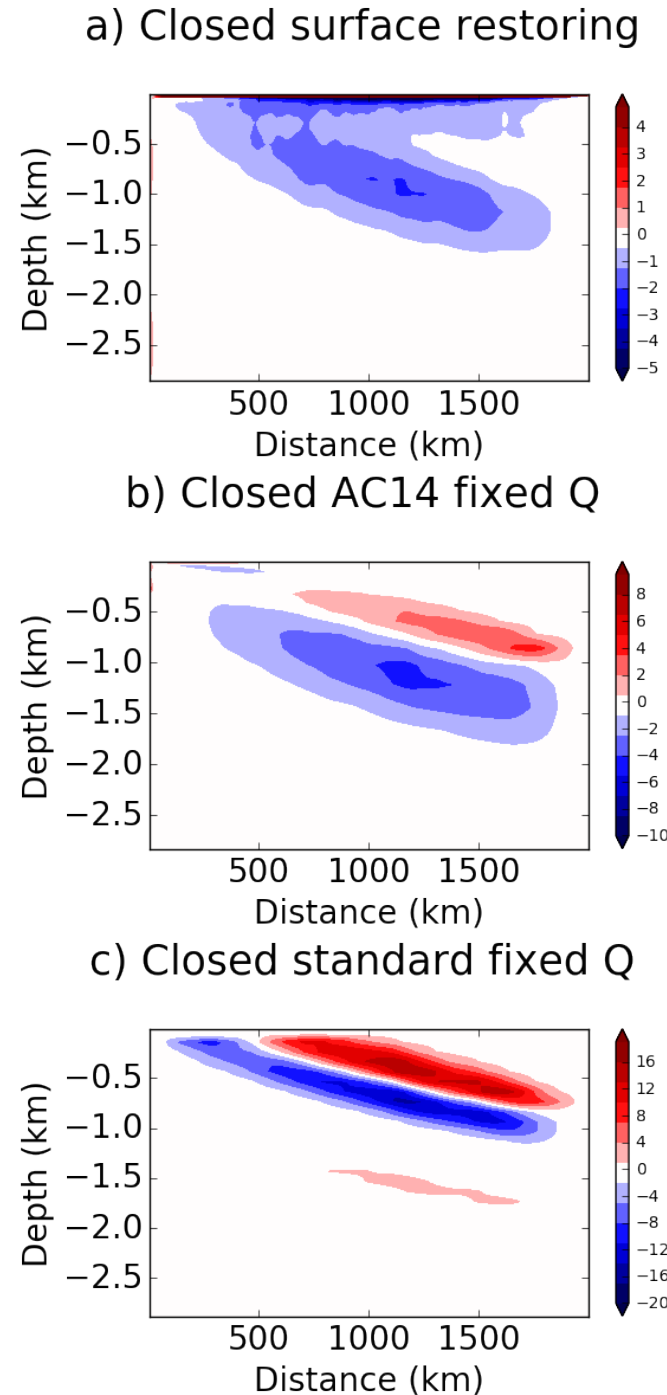


Figure 3.3: Zonal mean diapycnal heat divergence for varying surface forcing in flat bottom closed northern boundary runs. a) Surface restoring from AC14, b) Equivalent heat fluxes, c) Original heat fluxes.

These results imply that when surface restoring conditions are used the increase in diabatic eddy heat fluxes when the northern boundary is closed is much smaller than when a flux condition is used. The smaller increase is to be expected as for both the short relaxation timescale sponge and the closed wall basin the runs with

temperature restoring are weakly forced by heat exchange and feature a diabatic driven overturning cell that is mainly confined to the upper 250 m, cancelling the through its heat transport divergence the surface forcing, without the need to invoke strong diabatic eddy fluxes. When the diagnosed surface heat fluxes from the restoring conditions are applied, both the SO ROC and stratification in the channel change and they become more sensitive to the northern boundary condition. This adjustment is associated with a larger response in the diabatic eddy heat fluxes, associated with a collapsing SO ROC. This increase, however is still small in comparison to the increase when stronger, fixed surface heat fluxes are applied, consistent with observational estimates. In a closed basin the larger surface forcing creates deeper mixed-layers, allowing for stronger baroclinic instabilities and larger diabatic heat fluxes.

3.1.3 Summary

One of the main differences between using restoring conditions and fixed fluxes is that, when the northern boundary is closed, with fixed fluxes a deeper mixed-layer arises in the north, with isothermals at the bottom that surface only in the southern part of the channel, causing the establishment of a sharp thermal front in the south. When restoring to a fixed temperature gradient this response is prohibited, and even in the closed boundary case an anti-clockwise overturning in the surface layer exists. Which response is the correct one, cannot be deduced from these idealised experiments. While the temperature boundary condition is closer to a restoring condition, the surface boundary condition for freshwater forcing should be more like a fixed flux condition. Ultimately, however, the large adjustments associated with these changes in the SO ROC and diabatic processes north of the Southern Ocean, would also affect the atmosphere, that is the temperature profile to which sea surface temperature is restored and associated with this, the meridional profile of the wind forcing. Since it is impossible without using a global

coupled ocean-atmosphere model, to adequately represent all these processes, the results presented here must be interpreted as envelopes, or extreme limits, of the behaviour expected in a fully coupled model. For instance, the strong adjustment in sea surface temperature profile, when using fixed fluxes, to changes in the northern boundary condition might give an indication on how sea surface and atmospheric surface temperature could adjust to such changes further north. In any case, however, we should expect the response of a fully coupled global system to be a mixture of the responses shown in chapters 2 and 3 under different boundary conditions.

3.2 Varying the surface forcing

In section 3.1 we compared the impact of changing the surface forcing to a surface restoring taken from the channel model of *Abernathay and Cessi* (2014). Here we wish to further investigate the role that the surface heat boundary condition plays. The behaviour in model runs with surface restoring were quite different to fixed surface heat fluxes. Fig. 3.4 shows the variation in SOROC produced with the differing surface forcing.

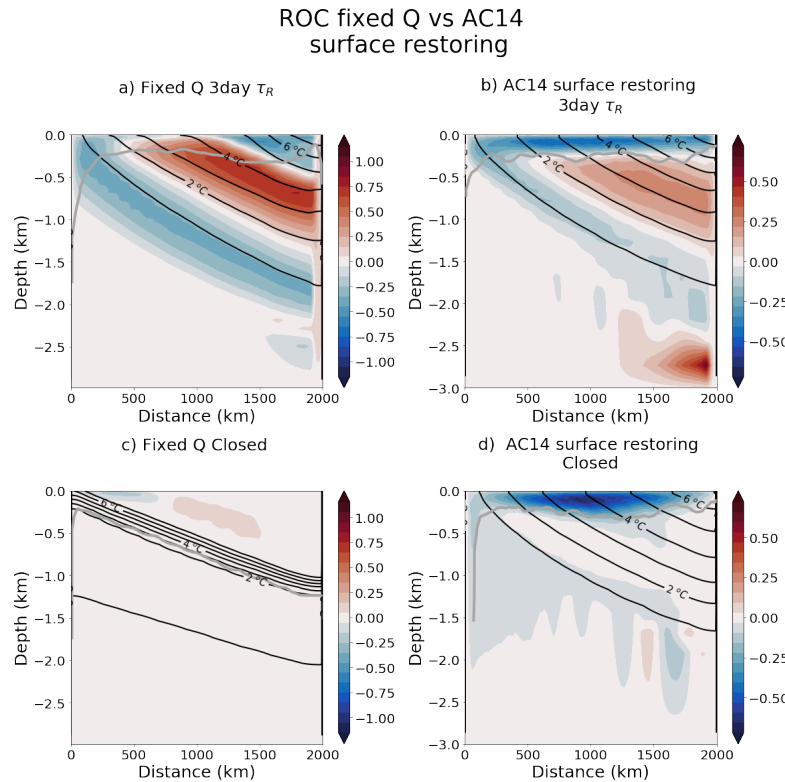


Figure 3.4: The isothermal stream function $\Psi_{res}(y, \theta)$ remapped onto depth coordinates, to give $\Psi_{res}(y, z)$ for a-b) $\tau_R = 3$ day and c-d) no relaxation. Isotherms in multiples of 1°C are overlaid as solid black contours. Note: AC14 runs b and d have rescaled colour bars to account for weaker circulation

It would appear perhaps that the surface restoring in AC14 heat forcing appears to be too weak. This provides some insight into the role of the surface forcing, but the very weak heat fluxes that negate some of our comparisons. When we applied the diagnosed heat fluxes from the surface restoring runs we see a differing result to the surface restoring (see Fig. 3.1 and Fig. 3.2) runs suggesting that the mechanics of surface restoring is playing a role in altering the way diabatic eddies respond to altered northern boundary conditions. The main questions we wish to address are: what causes the surface overturning cell seen in runs with surface restoring? why does the deep surface mixed layer appear with fixed fluxes and not with surface restoring? Can we produce the same strength SO ROC with surface restoring alone and if not why?

Table 3.1: Model Setup parameters for the flat bottom surface restoring experiments

| Symbol | Description | Value |
|-----------------|-------------------------------------|--|
| L_x, L_y, H | Domain | 1000 km, 2000 km, 300 m |
| L_{sponge} | Length scale of sponge layer | 100 km |
| Q_0 | Surface heat flux magnitude maximum | 0-10 W m ⁻² |
| τ_0 | Max surface wind stress | 0.2 N m ⁻² |
| dx, dy | Horizontal grid spacing | 5 km |
| dz | Vertical grid spacing | 5-280 m |
| Adv Scheme | 7 th order centred | 7 |
| Open τ_R | Sponge relaxation time scale | 30-day |
| Closed τ_R | Sponge relaxation time scale | ∞ |
| λ | Surface restoring time scale | 30-300 |
| r_b | Linear bottom drag parameter | 1.3x10 ⁻³ m s ⁻² |

3.2.1 Model set up

To investigate this we devised a further set of experiments. The model is once again based on the set up described in section 1.6 and we give a brief overview of the exact set up used here. The channel domain is 1000 km by 2000 km and 3000 m deep with an eddy-resolving horizontal resolution of 5 km with 30 geopotential layers, ranging in thickness from 5 m at the surface to 280 m at the bottom. To allow for a small domain size and reduce the computational cost the channel was setup with no topography as rationalized in *Abernathay et al.* (2011). To reduce spurious diapycnal mixing advection scheme 7 was chosen (*Hill et al.*, 2012; *Ilcak et al.*, 2012) and convective adjustment was employed to maintain a stable mixed layer. Key model parameters are outlined in Table 5.1.

The fixed surface model runs are again forced using similar zonal wind stresses and surface heat fluxes as in *Abernathay et al.* (2011) As a result, the profiles used

in *Abernathay et al.* (2011) have been adjusted to:

$$Q(y) = \begin{cases} -Q_0 \cos\left(\frac{18\pi y}{5Ly}\right) & \text{for } y \leq \frac{5Ly}{36} \text{ and } \frac{22Ly}{36} \geq y \geq \frac{30Ly}{36}, \\ -Q_0 \cos\left(\frac{18\pi y}{5Ly} - \frac{\pi}{2}\right) & \text{for } \frac{5Ly}{36} \geq y \geq \frac{20Ly}{36}, \\ 0 & \text{for } y \geq \frac{5Ly}{6}. \end{cases} \quad (1.65 \text{ revisited})$$

The surface wind stress is kept the same as in *Abernathay et al.* (2011):

$$\tau_s(y) = \tau_0 \sin\left(\frac{\pi y}{Ly}\right), \quad (1.64 \text{ revisited})$$

where L_y is the meridional width, $Q_0 = 2\text{-}10 \text{ W m}^{-2}$ and $\tau_0 = 0.2 \text{ N m}^{-2}$. As before the surface restoring and the sponge layer are set using a mask (M_{rbcs}) of values between 0 and 1 (0 = no relaxation, 1 = relaxing at a rate of $\frac{1}{\tau_T}$). The tendency of temperature at each grid point is modified to:

$$\frac{dT}{dt} = \frac{dT}{dt} - \frac{M_{rbcs}}{\tau_T}(T - T^*).$$

We adjust the value of (M_{rbcs}) to allow for differing timescales in the sponge and surface restoring.

For the additional runs with surface restoring alone as well as along side fixed surface heat fluxes we must determine a temperature profile varying with meridional distance. The profile for the surface restoring is drawn from *Zhai and Munday* (2014), where we can take the surface temperature profile from our fixed fluxes runs and moderate that in order to produce the same fluxes using Eq. (3.3).

$$T_s = T_{ref} - \frac{Q(y)}{\rho C_p \lambda \Delta z} \quad (3.3)$$

Where T_s is the surface restoring profile, T_{ref} is the reference profile, Q is the standard heat flux from the original experiments, ρ reference density and Δz the water depth. How the surface temperature profile must vary with varying λ is

shown in Fig. 3.5. We see at short restoring time scales we see a more similar profile to the reference profile (closer to linear and the profile used in AC14). As mentioned in the 30 day time scale is justified in *Haney* (1971) to be appropriate keeping the surface temperatures very close to the profile.

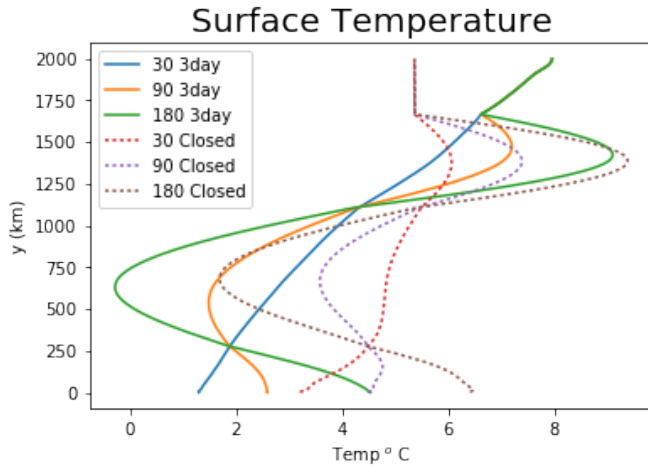


Figure 3.5: The surface temperature restoration profile calculated from eq. 3.3. Varying λ from 1 month to 6 months (30 - 300 days)

To establish the role of surface boundary condition we can adjust 3 parameters: Q , λ and T_{ref} . As mentioned previously the surface temperature is related to the stratification at the northern boundary:

$$T(y) = T_N(z = yS_T),$$

so that

$$\frac{\partial T}{\partial y} = -S_T \left(\frac{\partial T_N}{\partial z} \right),$$

We would expect to see a difference in results when we alter the T_{ref} to that of the closed boundary simulations as this may better match the closed wall northern boundary stratification. We performed some preliminary work to assess what experiments to run, this involved finding λ that produces the closest SO ROC to our runs in chapter 2 , including a small fixed surface Q to increase the SO ROC and runs without either fixed fluxes or restoring. After comparing results we used $\lambda = 90$. We will compare the strong sponge and closed boundary scenarios varying

lambda and the reference profiles as shown in Fig. 3.5 by dashed lines. These runs have both a weak surface heat flux ($Q_0 = 2W/m^2$) and pure restoring. The runs used are summaries in table 3.2.

Table 3.2: Outline of runs with differing surface forcing.

| Run name | Restoring or fixed fluxes? | Q_0 | λ | additional info |
|----------|----------------------------|------------|-----------|------------------------------|
| Original | fixed | $10 W/m^2$ | n/a | |
| AC14 | restoring | $0 W/m^2$ | 90 | with KPP |
| AC14HF | fixed | $0 W/m^2$ | 90 | |
| NoQ | none | $0 W/m^2$ | n/a | |
| L902Q | mixed | $2 W/m^2$ | 90 | T_{ref} altered for closed |
| L90 | restoring | $0 W/m^2$ | 90 | T_{ref} altered for closed |

In *Zhai and Munday* (2014) and *Abernathay and Cessi* (2014) and in section 3.1 we see a surface counter cell appear in the surface mixed layer that is not seen with fixed surface heat fluxes. We wish to assess what causes this and would the cell appear with surface restoring that most closing matches the fixed heat flux forcing? In *Zhai and Munday* (2014) this surface cell does disappear at surface restoring time-scales (λ) of greater than half a year and requiring spinning up with strong fixed surface heat fluxes.

3.2.2 Overturning

All experiments were run focusing on the closed northern boundary and the strongest sponge scenarios. The Eulerian Mean overturning remains constant for all the runs (at a maximum of ≈ 2.25 Sv) as the wind forcing remains the same throughout our experiments. In this section, we look at the effects these boundary conditions have on the two extremes of northern boundary conditions. The SO ROC is calculated as before as an isothermal streamfunction (Eq. (2.13)). Fig. 3.6, shows the SO ROC in temperature space for the two extremes of northern boundary condition, is included here for easy reference when comparing the differing surface forcing

with our original strong fixed surface heat fluxes used in chapter 2.

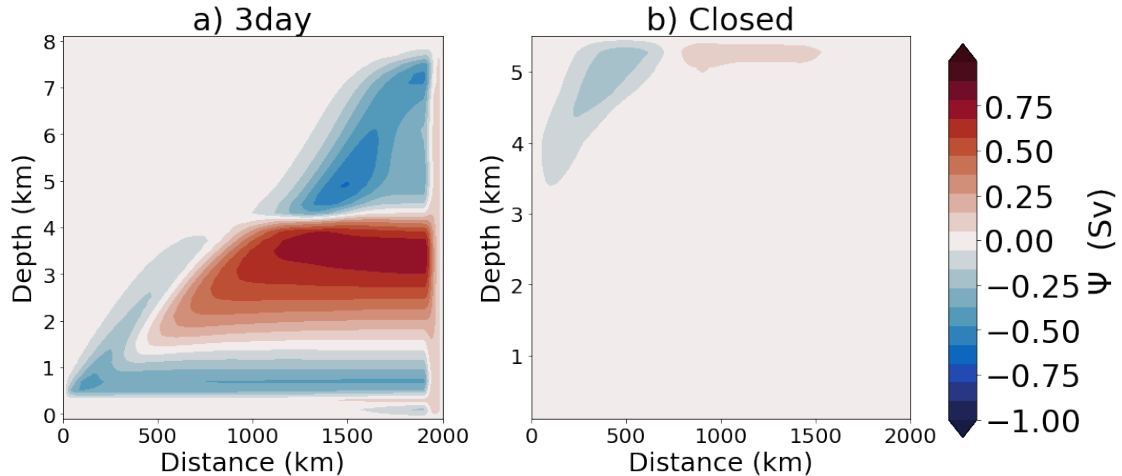


Figure 3.6: The isothermal stream function $\Psi_{res}(y, T)$ for a) $\tau_R = 3$ day and b) no relaxation.

No surface heat forcing

First, we show the effects of having no surface heat forcing. Spinning up the model runs that involve no surface heat forcing requires significantly more spin up time. Kinetic energy plots suggest after 1000 year spin ups the models are yet to achieve equilibrium. This leads to a noisy SO ROC. Fig. 3.7 shows the 3 day SO ROC is much diminished in the absence of either surface heat fluxes or surface restoring, at half the maximum and minimum values. Despite the noisy nature of the SO ROC generated we can see different overturning circulation forming, with no cooling in the south of the domain the lowermost cell is unable to form¹. We also see the surface counter clockwise cell that appeared in Fig. 3.2 at a minima of -0.4 Sv. The surface diabatic layer is also shallower than the runs with a fixed surface flux never extending deeper than 500 m. However, apart from the noise at depth, we see the SO ROC responds the same way by vanishing when the northern boundary is closed. It is worth noting, however, in the spin up of the closed scenario we see a different path to the collapsed state with no surface intensification before the SO ROC disappears.

¹*In the absence of topography

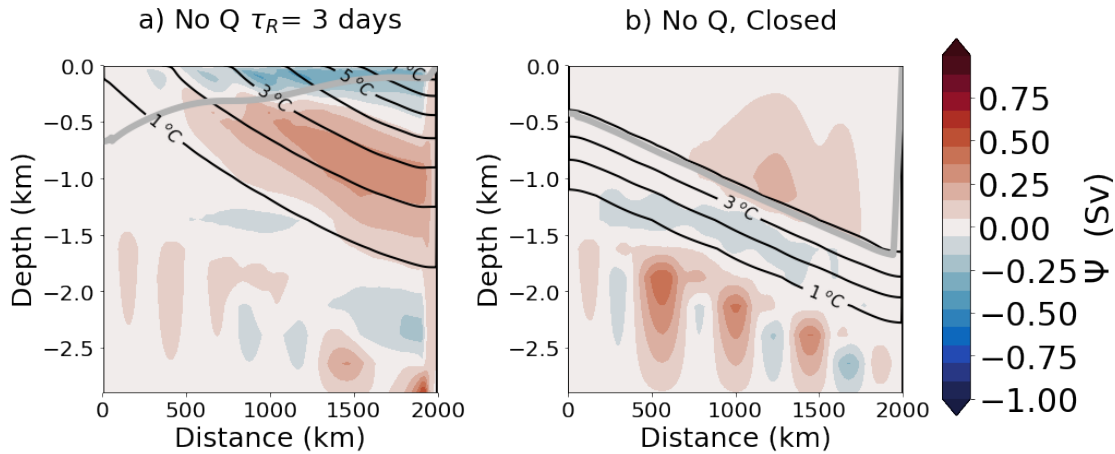


Figure 3.7: The isothermal stream function $\Psi_{res}(y, T)$ for a) $\tau_R = 3$ day and b) no relaxation, remapped into depth space.

In temperature space in 3.8.a we see how the counter-clockwise cell that appears in the surface extends down to lower temperatures than the fixed surface flux scenario (Fig. 3.6.a but the coldest temperature layers are not able to outcrop. Where isotherms do not outcrop no SO ROC can exist. We also see the source of the noise in Fig. 3.8b), mainly in the coldest waters that expand when remapped into depth space.

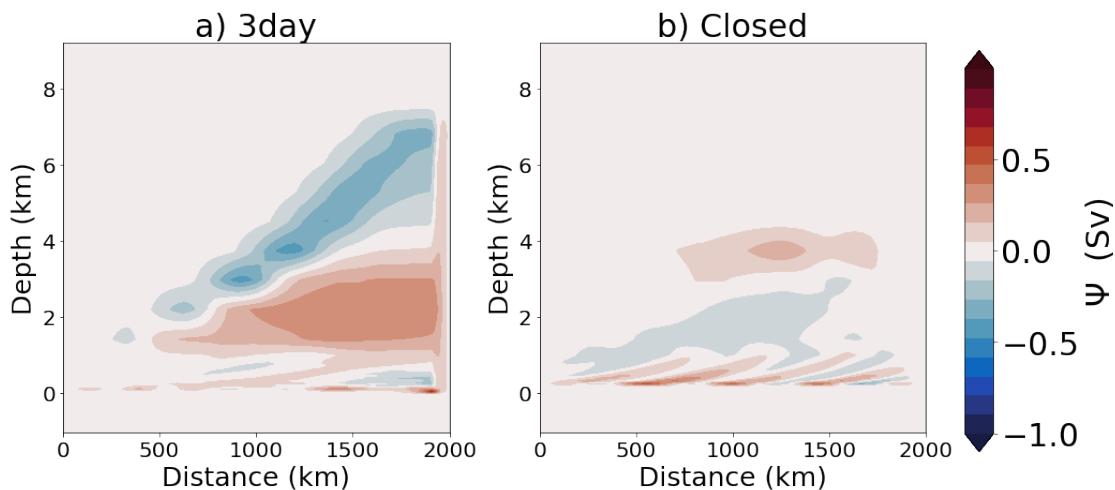


Figure 3.8: The isothermal stream function $\Psi_{res}(y, T)$ for no surface heat forcing runs: a) $\tau_R = 3$ day and b) no relaxation.

Surface restoring

When we set λ to 90 days as with all surface restoring runs we see a strong clockwise surface overturning not seen with only fixed fluxes. This cell was larger in runs with shorter λ . Fig. 3.9 shows the SO ROC for the extremes of τ_R and T_{ref} profile. The surface mixed layer remains similar for the T_{ref} profiles from the 3 day relaxation timescale runs in Fig. 3.9.a-b. This hints at the surface overturning cell being controlled by meridional temperature gradient we can deduce that the response to closing the northern boundary is moderated by surface conditions preventing the deep mixed layer from forming. In all cases when the northern boundary is closed the clockwise cell is unable to form Fig. 3.9.b-c and whenever surface restoring is employed the SO ROC strength remains around a third of the strength seen in the fixed flux cases.

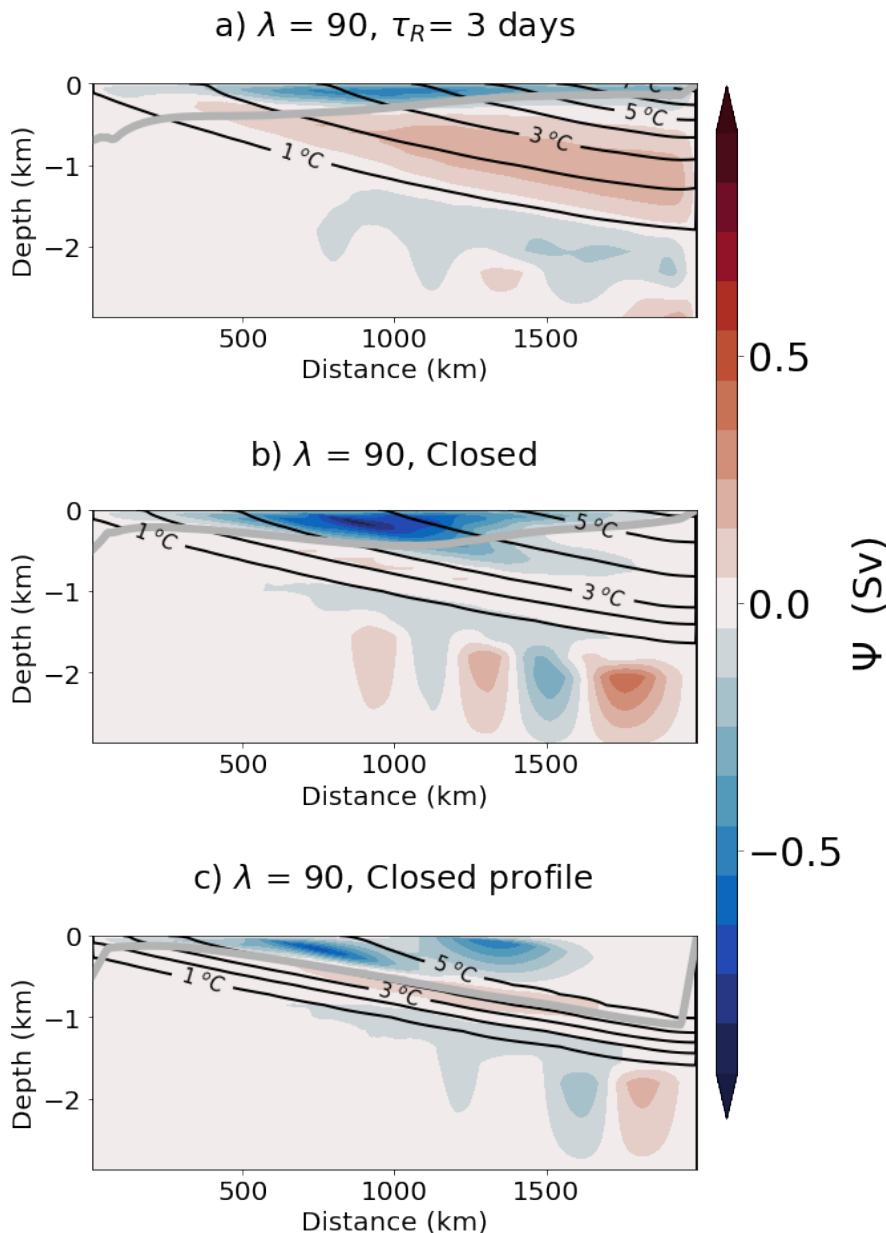


Figure 3.9: The isothermal stream function $\Psi_{res}(y, T)$ for surface restoring runs:
a) $\tau_R = 3$ day and b) no relaxation, remapped into depth space.

This behaviour is further demonstrated when we compare 3.10 with that of Fig. 3.6. The three cell pattern seen in Fig. 3.6.a is not established in Fig. 3.10.a with the upper anticyclonic cell elongated over many more latitudes and temperature layers. These long thin cells crossing many temperature layers suggest a diabatic nature to the overturning. When the boundary is closed Fig. 3.10.b keeps a strong intense surface overturning in the surface mixed layer, it is worth noting

in the fixed flux run spin up a large diabatic surface cell appeared before disappearing perhaps required to redistribute heat for the new equilibrium state. In the fixed flux runs we saw a drastic shift in the surface temperature profile which is prevented here by restoring to the standard surface temperature profile. Fig. 3.9.c and Fig. 3.10.c show that when the surface temperature profile is altered the deep surface mixed layer is able to form and the SO ROC is much more similar to the closed scenario when using strong fixed surface heat fluxes.

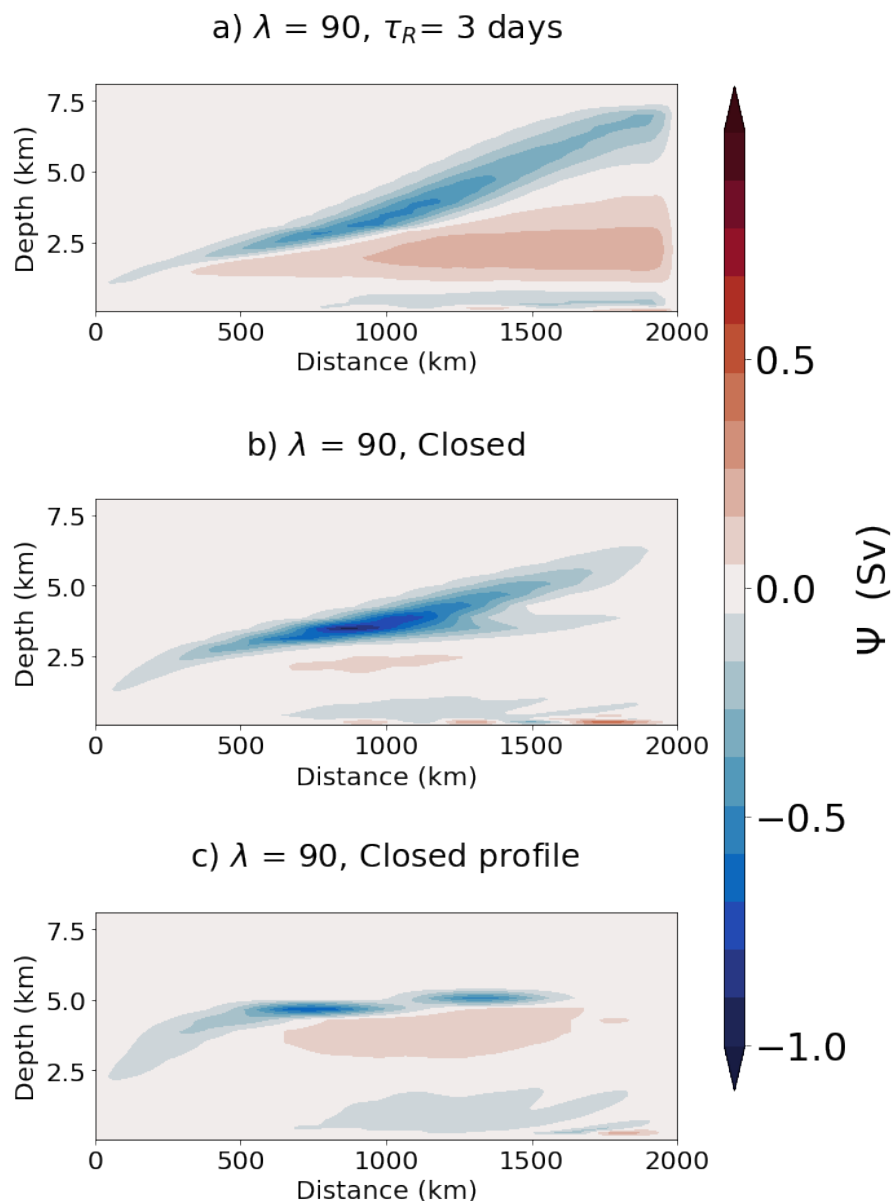


Figure 3.10: The isothermal stream function $\Psi_{res}(y, T)$ for surface restoring runs:
a) $\tau_R = 3$ day and b) no relaxation.

Surface restoring with a small flux

We have shown the SO ROC with strong fixed surface fluxes where we see a strong three cell overturning vanish when the northern boundary is closed (Fig. 3.6). Compared with no surface forcing when a very weak 2 cell SO ROC consists of a surface overturning cell and clock wise adiabatic cell vanished when the northern boundary is closed (Fig. 3.8) and surface restoring which generates a similar SO ROC that does not completely vanish when the northern boundary is closed but remains as an intense surface overturning cell (Fig. 3.10). This leads us to consider the scenario of mixed surface restoring and fixed fluxes if we include a small surface heat flux, does this allow the water mass transformations required. Fig. 3.11a. shows with an additional $2W/m^2$ a much strong SO ROC forms (around half that of the strong fixed fluxes), the additional cooling in the south of the domain also allows for the lowermost cell to form. When the northern boundary is closed the SO ROC remains the same as the surface restoring run without any additional surface fluxes added (Fig. 3.11.b).

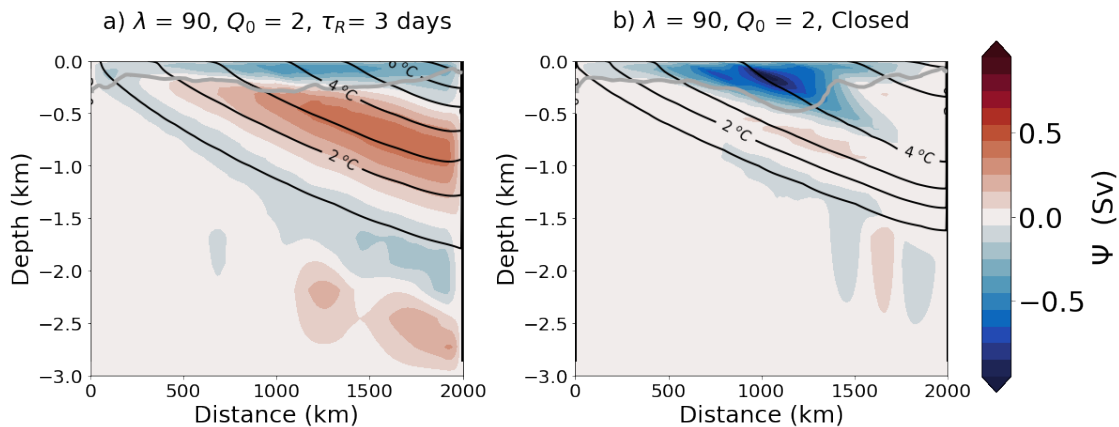


Figure 3.11: The isothermal stream function $\Psi_{res}(y, T)$ for a) $\tau_R = 3$ day and b) no relaxation, remapped into depth space.

This is further shown when plotted in depth space with Fig. 3.11.a more closely matching the fixed flux scenario Fig. 3.6.a ,but with an enhanced surface cell and Fig. 3.11.b matching Fig. 3.10.b showing little effect from the addition of heat fluxes in a closed scenario.

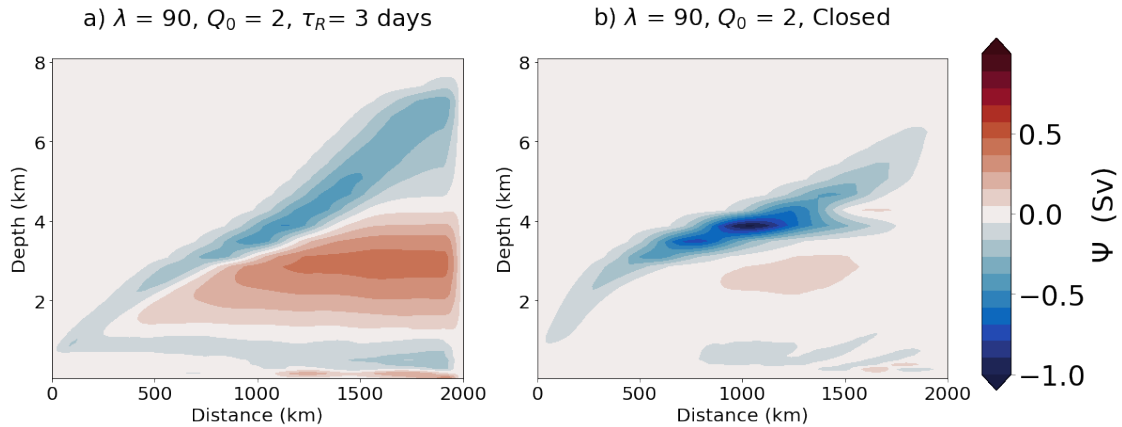


Figure 3.12: The isothermal stream function $\Psi_{res}(y, T)$ for mixed surface restoring and fixed-flux runs: a) $\tau_R = 3$ day and b) no relaxation.

These runs demonstrate the surface cell and surface mixed layer appear to be dependent on the surface meridional temperature gradient and the deep cell is dependent on cooling over the south of the domain in the absence of topography. The mixed layer depth depends with decreasing meridional temperature gradient perhaps controlling the southwards eddy-induced transport at the surface requiring further analysis.

Heat Budget

Starting from Eq. (2.5):

$$\underbrace{\frac{\partial \bar{v}T}{\partial y} + \frac{\partial \bar{w}T}{\partial z} + \frac{\partial \bar{v}'T'S_T}{\partial z} + \frac{\partial \bar{v}'T'}{\partial y}}_{\text{Residual } (\nabla \cdot \bar{\mathbf{u}}_{res} \bar{T})} = \underbrace{\frac{\partial Q}{\partial z}}_{\text{air-sea fluxes}} - \underbrace{\frac{\partial (\bar{w}'T' - \bar{v}'T'S_T)}{\partial z}}_{\text{Diabatic eddies}} = \frac{\partial(Q - D)}{\partial z}.$$

We can, as before use the terms to gain insight of the redistribution of heat in these model runs.

No surface heat forcing

In the absence of any surface heat forcing when we evaluate the terms in 2.5 , with no surface heat flux terms to force heat redistribution we see little latitudinal variation in vertically integrated terms from 2.5 in Fig. 3.13. There a peak coinciding with the maximum overturning of the SO ROC in Fig. 3.13a) which is absence in Fig. 3.13b) when there is no SO ROC present. Overall we see the heat flux divergence fall 10 fold when the northern boundary is closed.

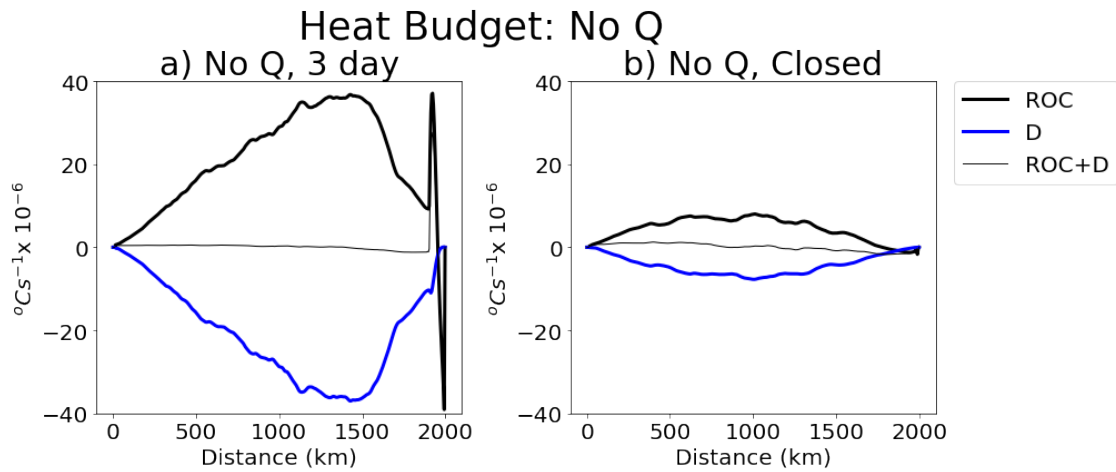


Figure 3.13: The components of the full depth heat budget of the no surface heat forcing runs evaluated in as in Eq. 2.5.

When we plot the diabatic eddy heat flux term in depth space (Fig. 3.14) We once again see the near perfect dipole pattern emerge when the northern boundary is closed contributing to the very small vertically integrated values. One thing to note is the the diabatic eddy heat flux divergence is separated from the surface and without heat forcing shows no asymmetry in the divergence and convergent cells that appear in the closed scenario. The values for both are significantly smaller suggesting the surface heat flux plays a role in setting the strength of the diabatic eddy heat flux divergence as well as the spatial distribution (to a lesser extent).

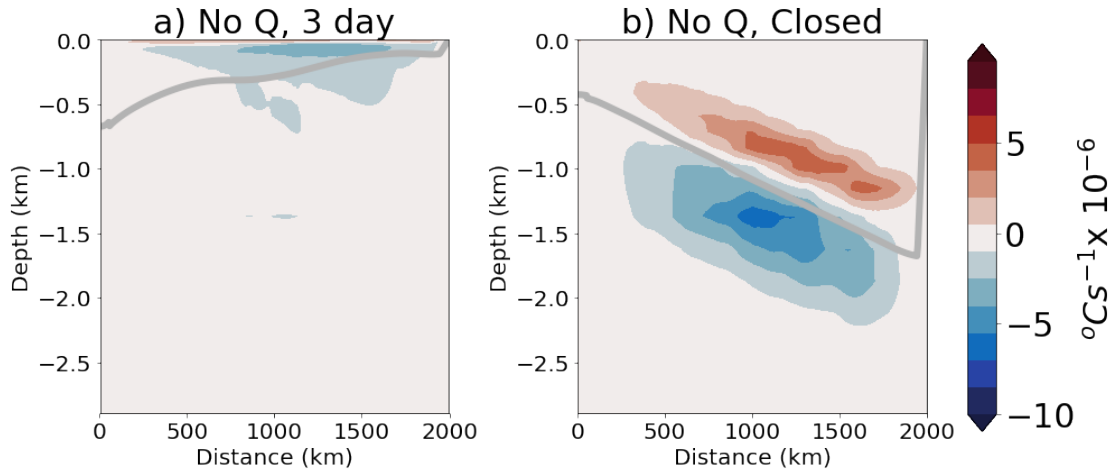


Figure 3.14: Zonal mean diapycnal eddy heat flux divergence for runs with no surface heat forcing for a) Strong sponge b) Closed northern Boundary.

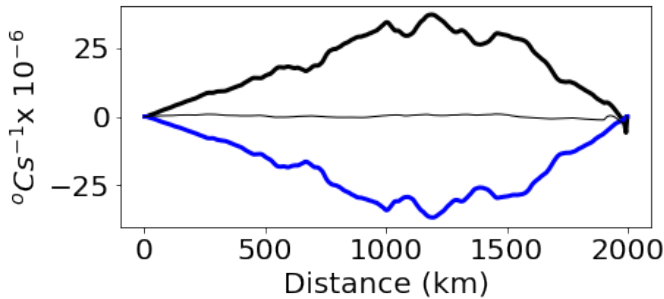
This is useful to see the diabatic eddy heat flux dipole appears to not require fixed surface heat fluxes Fig. 3.14.b. The dipole once again forms around the deep mixed layer.

Surface restoring

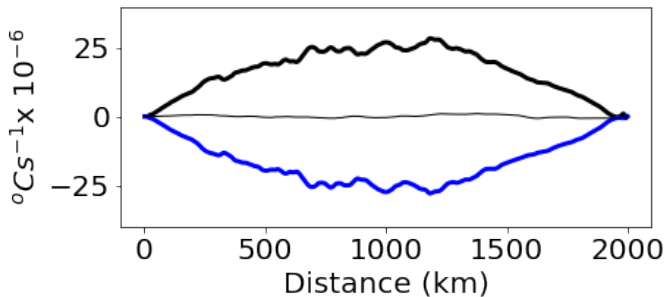
We now look at the surface restoring runs. As the runs with a small heat flux added produced very similar results to those with surface restoring alone we discuss only the surface restoring runs here for brevity. Overall the largest vertically integrated heat flux divergences are in Fig. 3.15.a when we have strong sponge layer, turning off the sponge layer in Fig. 3.15.b reduces this by 25%, but when the closed surface temperature profile is applied alongside the closed northern boundary we get a 50% reduction Fig. 3.15.c.

Heat Budget: $\lambda = 90$

a) $\lambda = 90, \tau_R = 3$ days



b) $\lambda = 90$, Closed



c) $\lambda = 90$, Closed profile

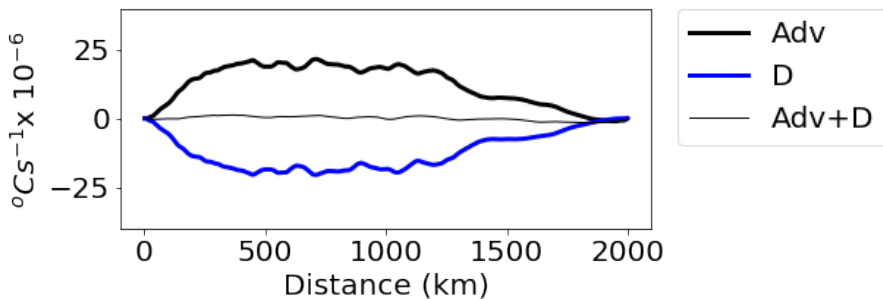


Figure 3.15: The components of the full depth buoyancy budget for mixed surface forcing runs evaluated in as in Eq. 2.5.

This is much like our original fixed flux runs when we compare the diabatic eddy heat flux divergence in depth space. We see a small surface convergence in Fig. 3.16.a which leads to a large vertical integrated term with nothing to counteract it at depth. Unlike the surface restoring experiments we used in section 3.1 we

see the formation of a dipole in the diabatic eddy heat flux divergence when the northern boundary is closed Fig. 3.16.b-c that does not arise with the restoring of *Abernathay and Cessi* (2014). When the surface is restored to the surface profile set by a strong sponge we see coherent diabatic eddy heat flux divergence Fig. 3.16.a-b, this is also seen in every run that generates the surface overturning cell (Fig. 3.14 and Fig. 3.2) and can be associated with diabatic layer anticlockwise overturning. This suggests the surface overturning cell is linked to the surface meridional temperature gradient. Indeed we see a slight decrease in surface temperature gradient over the ACC in our fixed flux runs from chapter 2. When we switch to the surface temperature profile of the closed runs we get a strong diabatic eddy heat flux divergence dipole arising much like we saw in chapter 2. This also aligns with a deep mixed layer. Suggesting that a weak meridional temperature gradient allows for the set up of opposing diabatic eddy heat flux divergence cooling the upper layers and warming bottom to generate a sharp internal boundary layer.

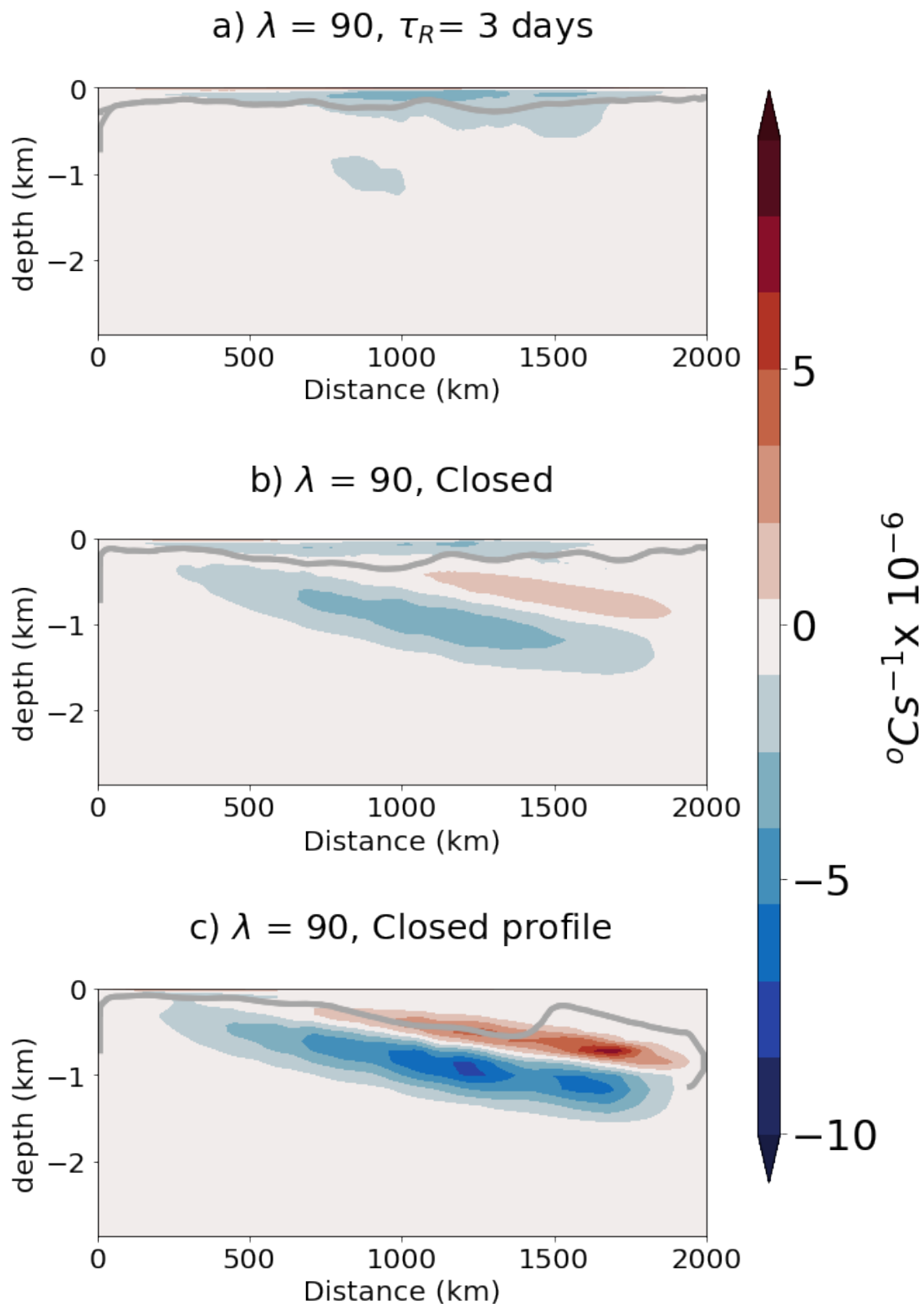


Figure 3.16: Zonal mean diapycnal eddy heat flux divergence in surface restoring runs with closed northern boundary.

Energetics

No surface heat forcing

With out any surface heat forcing we see a stark difference in EKE response to closing the northern boundary. Fig. 3.17 shows a decrease in EKE maxima as well as a decrease in the area over which there is enhanced eddy kinetic energy. This is not perhaps what we would expect as the same large decrease in stratification occurs in a deep mixed layer. Once again we see little increase in the Mean kinetic energy.

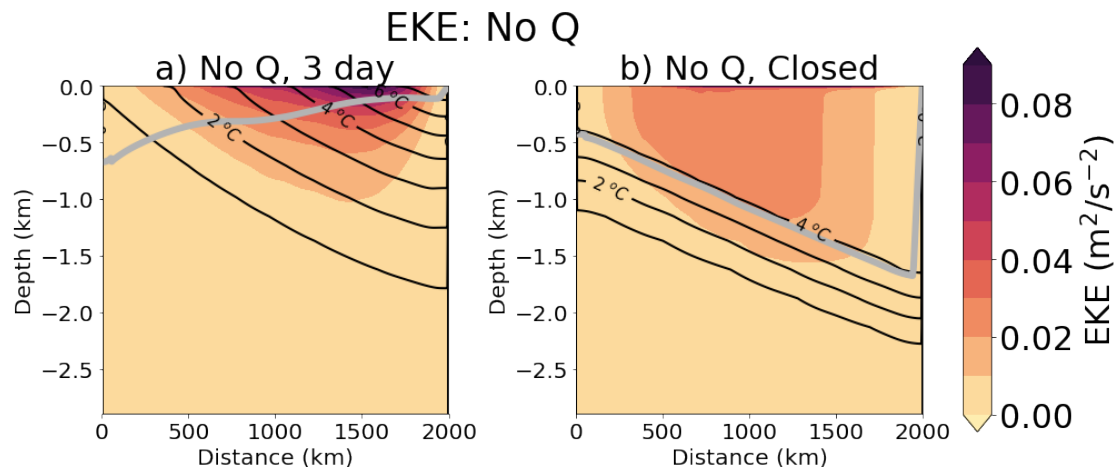


Figure 3.17: Zonal mean EKE for no surface forcing runs. a) Strong sponge, b) Closed northern boundary.

Surface restoring

EKE remains fairly consistent across all the runs with fixed Q or surface restoring. We do not see the increase in EKE when the northern boundary is closed but the surface restoring remains the same Fig. 3.18.b, but the increase seen in the fixed flux runs is nearly replicated when the surface restoring is set using the closed Fig. 3.18.c.

EKE: $\lambda = 90$

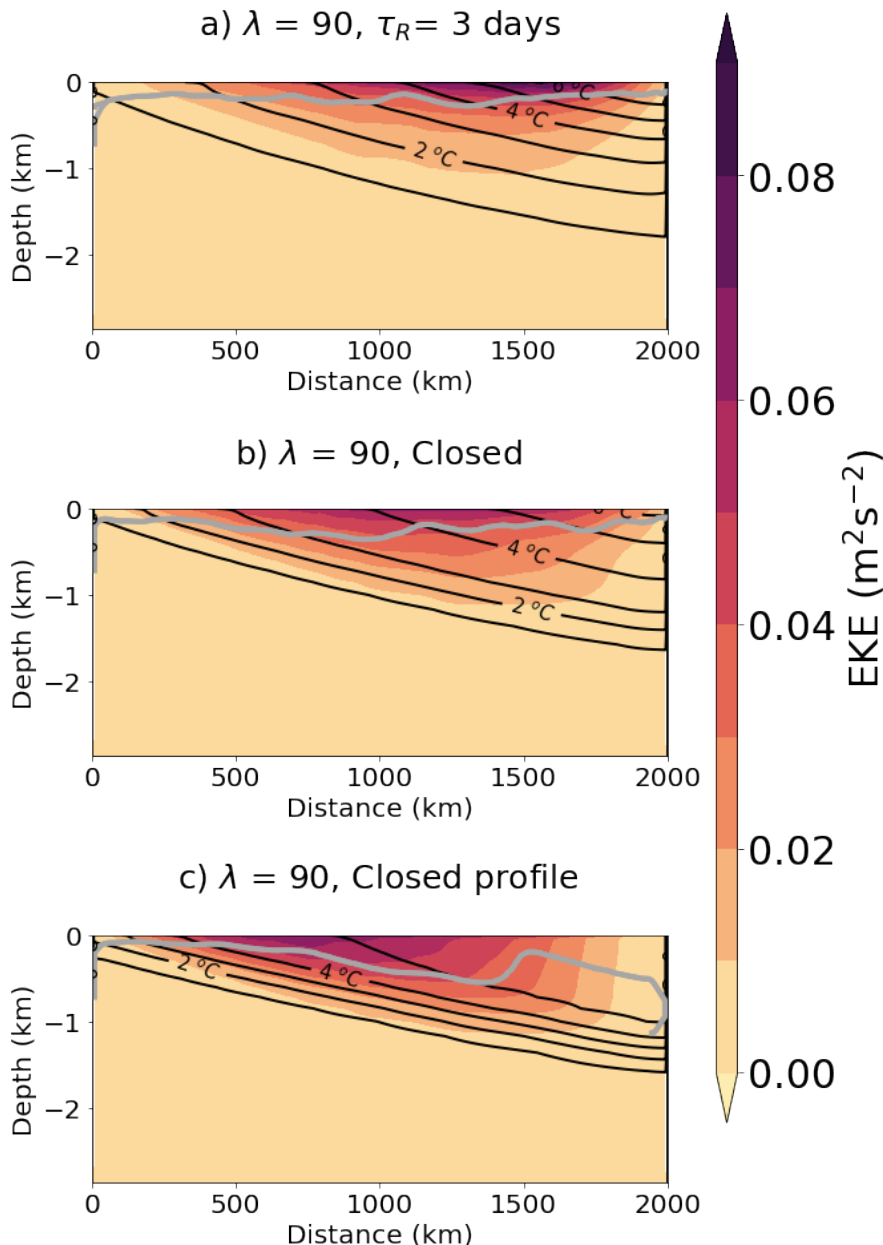


Figure 3.18: Zonal mean EKE for surface restoring runs. a) Strong sponge, b) Closed northern boundary c) Closed northern boundary and closed restoring profile.

However, EPE is increased with surface restoring and reduced with the addition of a fixed surface Q, a large increase is seen in the northern half of the domain. EPE is plotted for our surface restoring experiments in Fig. 3.19. The surface restoring is forcing short time scale temperature perturbations relaxing surface temperature to a prescribed profile. This is greatly increased by setting the restoration profile

using the closed scenario Fig. 3.19.c where large temperature perturbations are combined with sharp temperature gradients at the internal boundary layer.

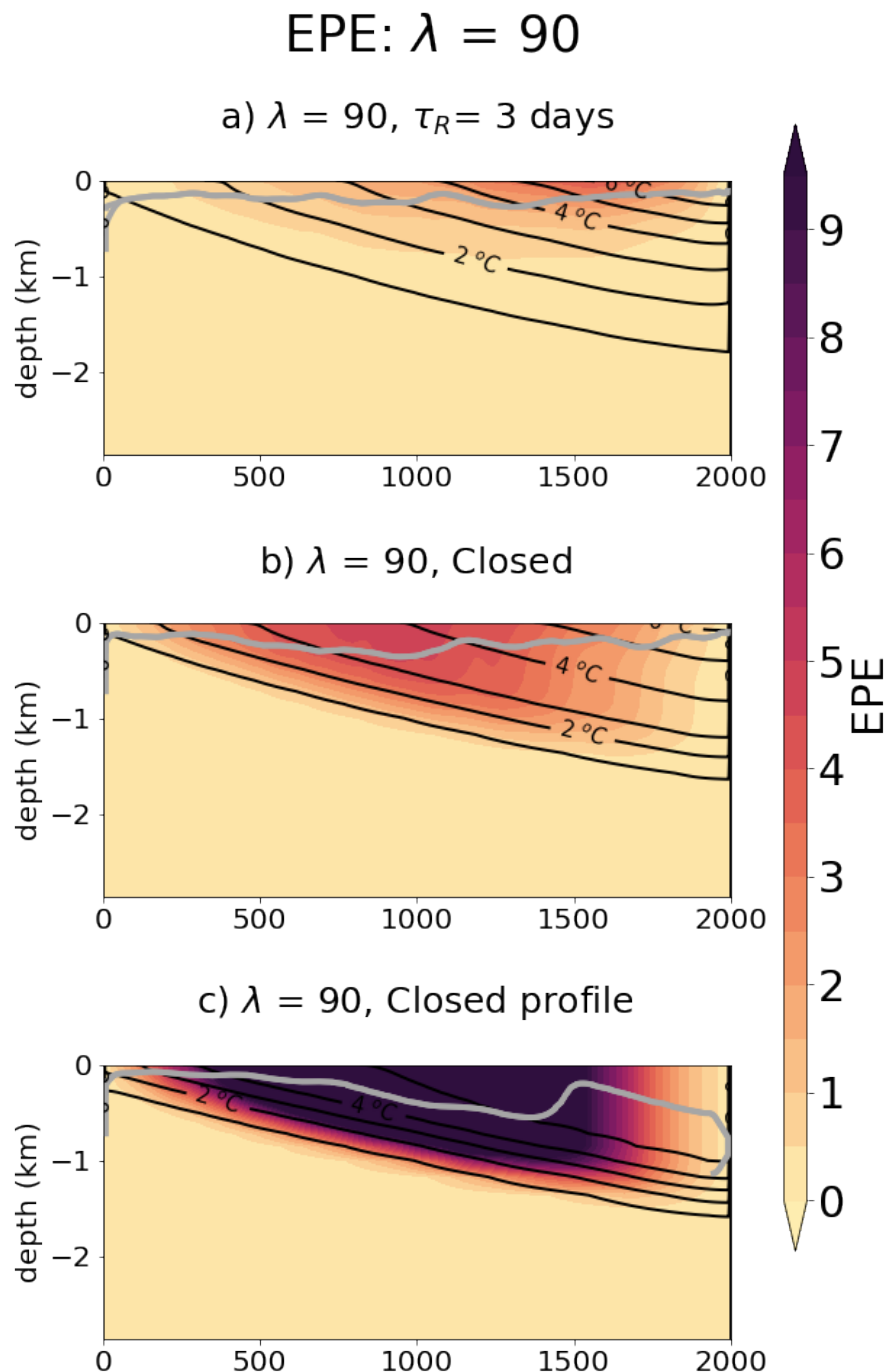


Figure 3.19: Zonal EPE for surface restoring runs. a) Strong sponge, b) Closed northern boundary c) Closed northern boundary and closed restoring profile.

3.2.3 Conclusions on varying the surface boundary condition

We did not find any regime where diabatic eddy fluxes can be neglected even when using restoring conditions. The vertical integral of the diabatic eddy heat flux convergence decreases by an order of magnitude for weaker diabatic forcing in the sponge layer, however, the eddy fluxes themselves increase by a factor of 2 to 3 between a closed basin and a configuration with strong restoring to a prescribed temperature stratification in the northern sponge layer.

When using a restoring boundary condition the main balance in the vertically integrated heat budget is somewhat different because no internal boundary layer develops and the northward deepening of the mixed layer is absent except for when the surface is restored using the closed fixed flux scenario as the reference temperature. In the runs with surface restoring to a strong meridional temperature gradient the ROC is even more confined to the surface layer, and also in the case of a closed basin diabatic eddies and heat transport convergence by the ROC dominate the surface forcing. To illustrate our conclusions on the impact of surface restoring on the diabatic eddy and SO ROC response to closing the northern boundary, we include here additional plots for various surface restoring scenarios compared with the fixed surface flux scenario for the closed northern boundary runs.

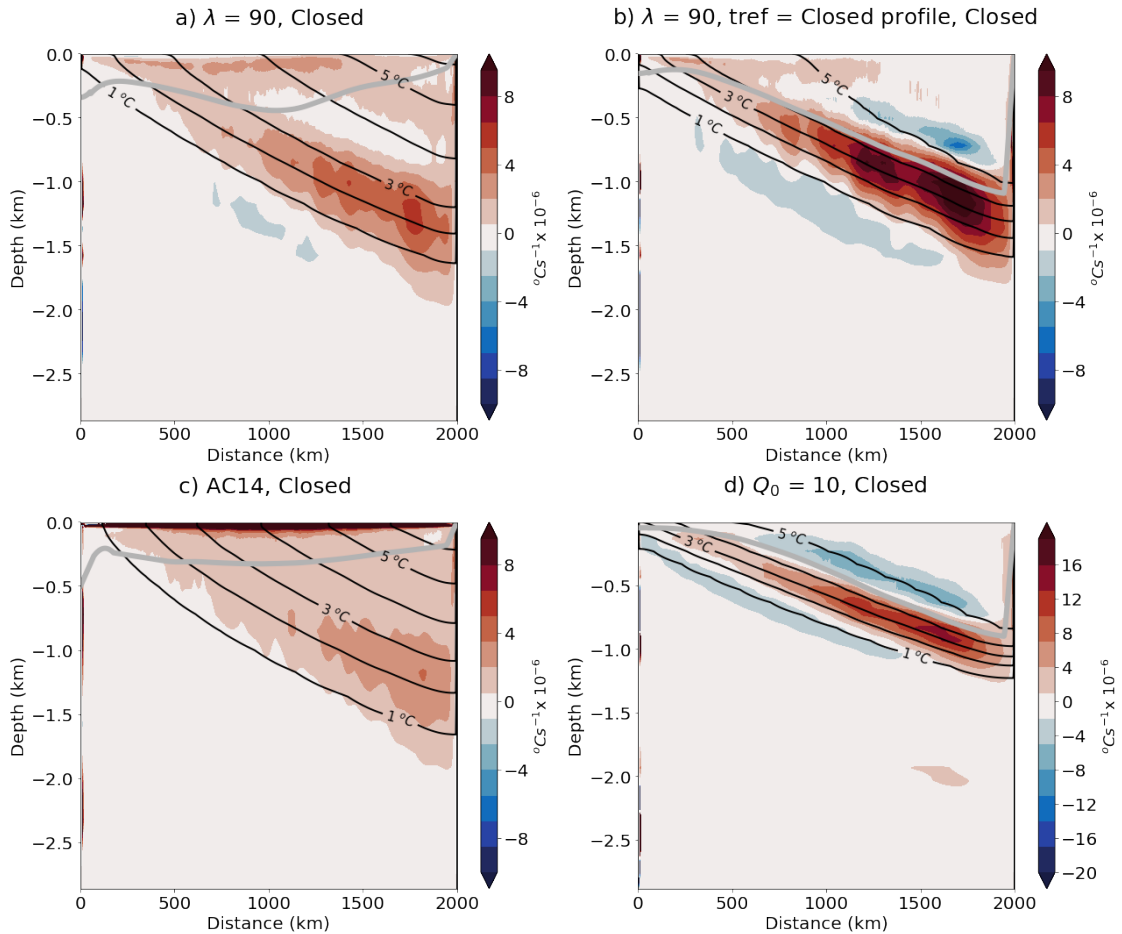


Figure 3.20: Zonal mean advective heat flux divergence for various surface heat forcing scenarios with closed northern boundary. a) Surface restoring, b) Surface restoring with closed restoration profile c) AC14 surface restoring and d) fixed surface fluxes.

In the AC14 surface restoring runs, there is a very larger heat flux divergence in the surface Fig. 3.20.c generating a large surface overturning. This pattern is reduced with a weaker surface restoring Fig. 3.20.a, where we saw a weaker surface overturning cell, both the ROC heat divergence and the diabatic eddy heat divergence show less intensification surface intensification. Fig. 3.20.a is very similar to Fig. 3.20.c with a near linear reference temperature profile, but weaker restoring, the surface meridional temperature gradient, however, is weaker, then when restoring to a reference profile from the closed scenario fixed fluxes Fig. 3.20.b begins to match Fig. 3.20.d more closely with the alternating patterns of divergence and convergence emerging.

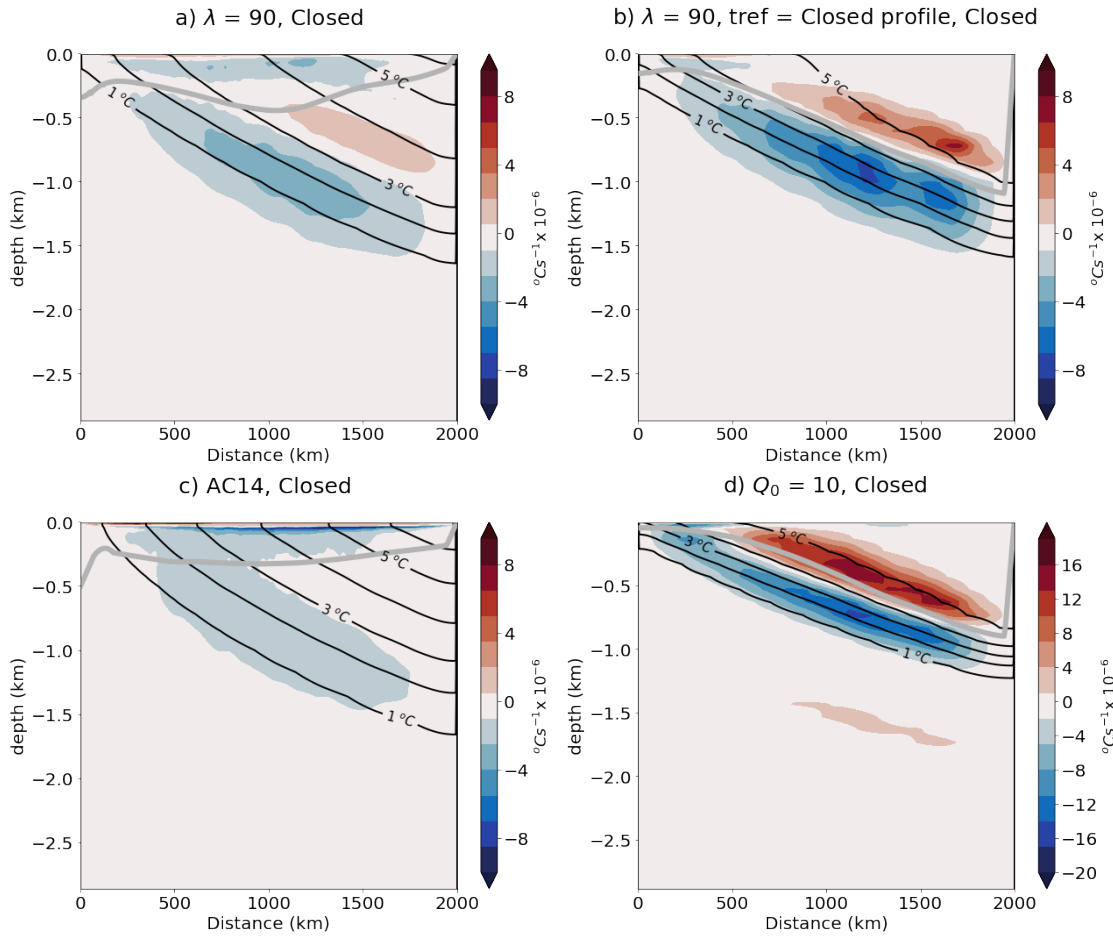


Figure 3.21: Zonal mean diapycnal eddy heat flux divergence for various surface heat forcing scenarios with closed northern boundary. a) Surface restoring, b) Surface restoring with closed restoration profile c) AC14 surface restoring and d) fixed surface fluxes.

This pattern is further illustrated when examining the diabatic eddy heat flux divergence in Fig. 3.21. We see a clear transition from Fig. 3.21.c to Fig. 3.21.b to Fig. 3.21.b to the fixed flux scenario Fig. 3.21.d. With the emergence of a strengthening convergence/ divergence dipole with weakening meridional temperature gradient and a deepening of the surface mixed layer.

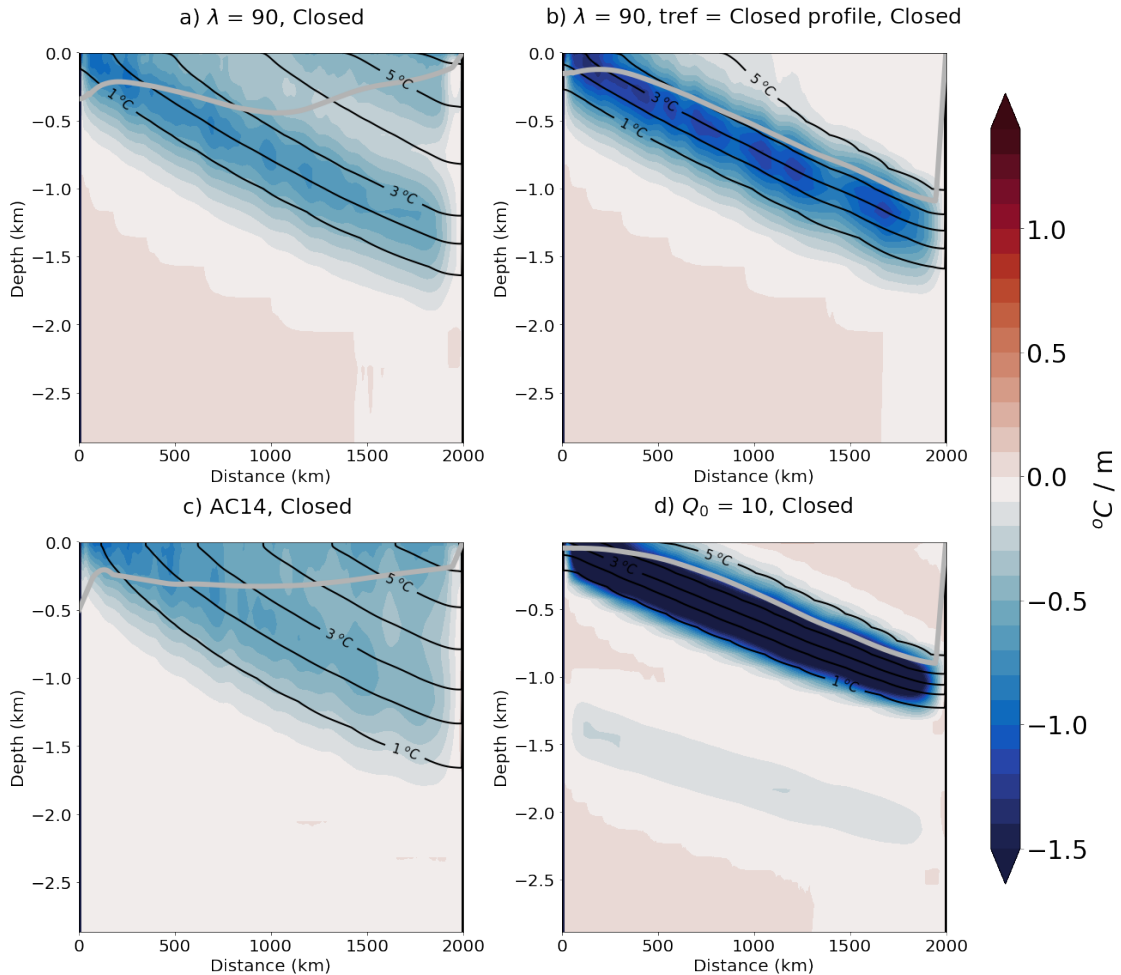


Figure 3.22: Meridional temperature gradient for various surface heat forcing scenarios with closed northern boundary. a) Surface restoring, b) Surface restoring with closed restoration profile c) AC14 surface restoring and d) fixed surface fluxes.

For reference we plot the zonal mean meridional temperature gradient in Fig. 3.22.

As shown by the temperature contours were we get an intense surface overturning we have consistent strong meridional temperature gradient Fig. 3.22.c where strong southward eddy heat fluxes dominate. The gradient is much less constant Fig. 3.22.a allowing for a reduction in that intense surface cell. When the SO ROC collapses with a closed northern boundary we see weak surface meridional temperature gradients in the north of the domain Fig. 3.22.b and Fig. 3.22.d. These results demonstrate the complex nature we would expect from a coupled system the perfect dipole in the diabatic eddy heat could arise from either fixed fluxes or surface restoring but only with certain caveats. We can see that in all cases the

SO ROC is altered dramatically when the northern boundary is closed.

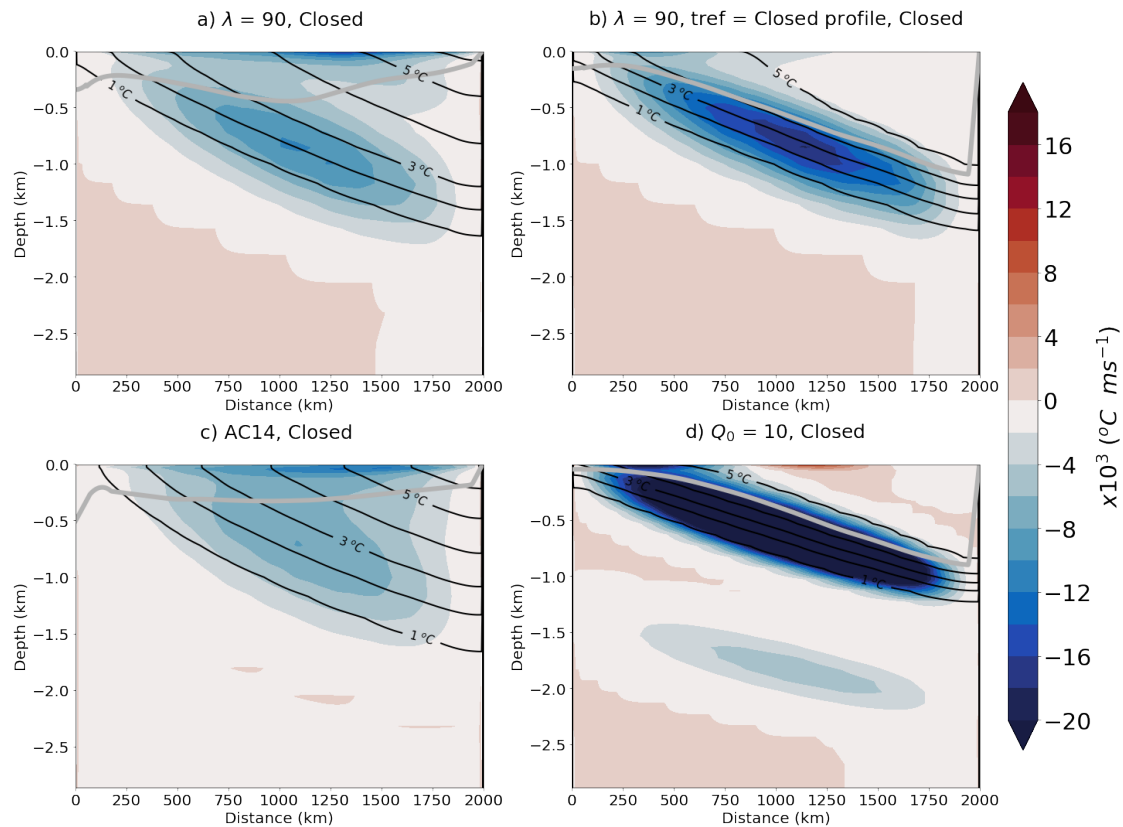


Figure 3.23: Meridional eddy heat fluxes for various surface heat forcing scenarios with closed northern boundary. a) Surface restoring, b) Surface restoring with closed restoration profile c) AC14 surface restoring and d) fixed surface fluxes.

Chapter 4

Varying the northern boundary stratification

The previous chapters have shown the role of diabatic eddies in responding to closing the northern boundary. Originally we ran experiments altering τ_r , the relaxation time scale, this dramatically altered the domain stratification so a natural extension to this is to alter the stratification profile of the sponge layer by altering the e-folding depth scale N . We saw although some gradual changes can be seen with increasing relaxation timescale, this is more a stepped response between turning on or off the sponge layer when using relaxation timescale as the variable, to assess if this would truly be a stepped response directly altering the stratification to see how the SO ROC responds. This may also assist to assess if there as any form of proportionality in that response relating to T_N . It should be stressed that as an idealised modelling study these will just be approximate proportionality merely forming a guide for consideration of consequences for altering boundary conditions. Or to guide further studies to narrow down a parameterisation once more complex factors are included such as a coupled atmosphere and variations in salinity. Chapter 2 showed us that changing stratification at the northern boundary can lead to increased diabatic eddy heat fluxes from increase diabatic layer

depth and EKE and a small increase in APE. Those experiments used changing sponge layer to achieve this so although allowed a demonstration of the change in diabatic eddies leaving to modulating the effects of effective surface buoyancy forcing. Although this allowed us to gain insight into what factors control diabatic eddies and the role that diabatic eddies can play in setting the ROC these experiments did not allow us to establish a direct relationship between stratification and diabatic eddy heat fluxes. These findings prompted us to investigate further the link between northern boundary stratification and diabatic eddy heat flux modulation of the effective buoyancy forcing. Establishing how diabatic eddies will respond to altered northern boundary conditions may be important for setting up a channel or southern hemispheric models; where the effective buoyancy forcing may be partly determined by the northern boundary condition before the surface parameters are altered. Understanding the response of diabatic eddies to changing background ocean stratification may also be useful for parametrisations in climate models and understanding the Southern Ocean response in high-resolution climate models. We now investigate diabatic eddy heat fluxes with a direct alteration of northern boundary stratification to propose a new scaling of diabatic eddy heat fluxes with stratification.

4.0.1 Set up

Once again we base the model set up off the set up described in section 1.6 (Fig. ??) however we now directly alter the northern boundary stratification to establish a relationship. We use an idealised channel model setup similar to part I based off the setup used in *Abernathay et al.* (2011). For an in depth explanation of model set up the reader is directed to Part I. The model code is the Massachusetts Institute of Technology general circulation model (MITgcm) (*Marshall*, 1997). The channel domain is 1000 km by 2000 km and 2985 m deep with an eddy-resolving horizontal resolution of 5 km with 30 geopotential layers, ranging in thickness from 2 m at the

surface to 275 m at the bottom. The surface forcing is a the original fixed surface heat flux:

$$Q(y) = \begin{cases} -Q_0 \cos\left(\frac{18\pi y}{5Ly}\right) & \text{for } y \leq \frac{5Ly}{36} \text{ and } \frac{22Ly}{36} \geq y \geq \frac{30Ly}{36}, \\ -Q_0 \cos\left(\frac{18\pi y}{5Ly} - \frac{\pi}{2}\right) & \text{for } \frac{5Ly}{36} \geq y \geq \frac{20Ly}{36}, \\ 0 & \text{for } y \geq \frac{5Ly}{6}. \end{cases}$$

The surface wind stress is kept the same as in *Abernathay et al.* (2011):

$$\tau_s(y) = \tau_0 \sin\left(\frac{\pi y}{Ly}\right),$$

where L_y is the meridional width, $Q_0 = 10 \text{ W m}^{-2}$ and $\tau_0 = 0.2 \text{ N m}^{-2}$.

For the control run the northernmost 100 km of the domain is a full depth sponge layer to relax the northern boundary temperature (T) profile to a prescribed temperature profile:

$$T^*(z) = \Delta T \frac{(e^{z/N} - e^{-H/N})}{1 - e^{-H/N}},$$

assuming a natural stratification $N = 1000 \text{ m}$ and a temperature difference (ΔT) of $8 \text{ }^\circ\text{C}$. The sponge is set using a mask (M_{rbcs}) of values between 0 and 1 (0 = no relaxation, 1 = relaxing on time scale $\left(\frac{1}{\tau_T}\right)$). The tendency of temperature at each grid point is modified to:

$$\frac{dT}{dt} = \frac{dT}{dt} - \frac{M_{rbcs}}{\tau_T}(T - T^*),$$

where the relaxation timescale τ_T is set to 3 days.

We then directly alter the northern boundary stratification by altering N in Eq. 1.66 from $N = 50 \text{ m}$ to $N = 10000 \text{ m}$.

Another way to directly alter the northern boundary stratification is by altering ΔT . Once again a channel model set up similar to that outlined in chapter 2 and that will be further outlined in the next section. We began to investigate the effects

of direct alteration on the northern boundary stratification.

4.0.2 Preliminary experiments

We ran a series of experiments varying N from 50 m to 10000 m, which generate the temperature profiles shown in

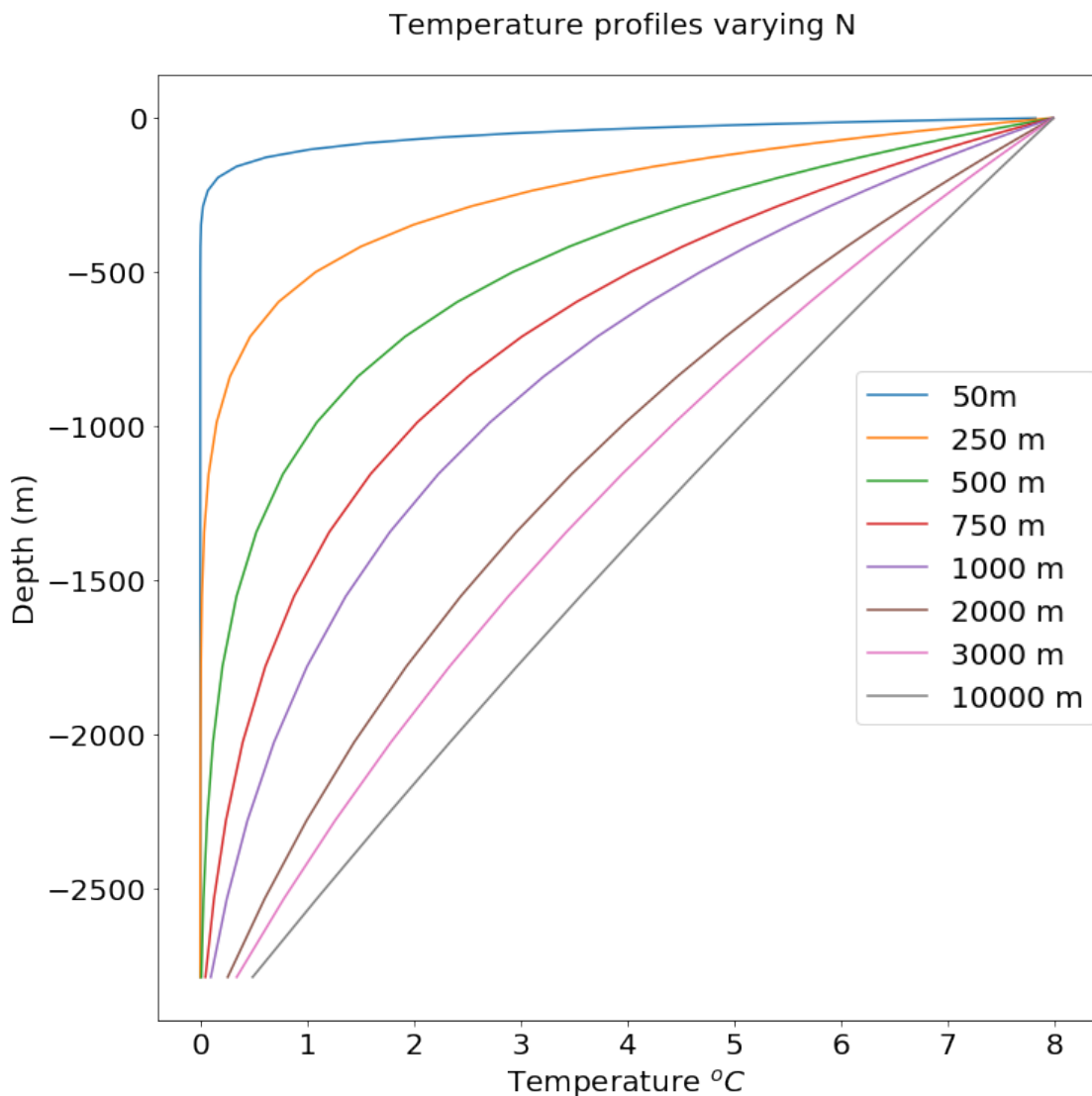


Figure 4.1: Sponge layer temperature profiles altering N in Eq. (1.66).

4.2 shows the ROC when these new stratifications are applied. The natural stratification of 1000m used in previous experiments Fig. 4.2.e shows the 3 cell ROC we are familiar with and increasing N depth weakens the ROC as isotherms

appear to flatten slightly Fig. 4.2. When the e-folding length N is reduced we see a steepening of the isotherms in the south of the domain and a shallowing of the isotherms in the upper north of the domain. This leads to a large increase in the lower-most cell - baroclinic instability driven overturning cell Fig. 4.2.a-c. However, the steep isotherms and 'bumpy' nature of this overturning appears somewhat unstable as the isotherms become almost vertical in the south of Fig. 4.2. Fig. 4.2. We see a full depth diabatic layer ¹ in the south of the domain. Fig. 4.2. f-h) have unventilated isotherms which leads to some behaviour that suggests the model has not reached equilibrium.

¹For speed in the calculation the mixed layer depth plotted here is simply the MITgcm output mixed layer depth, which gives an approximation.

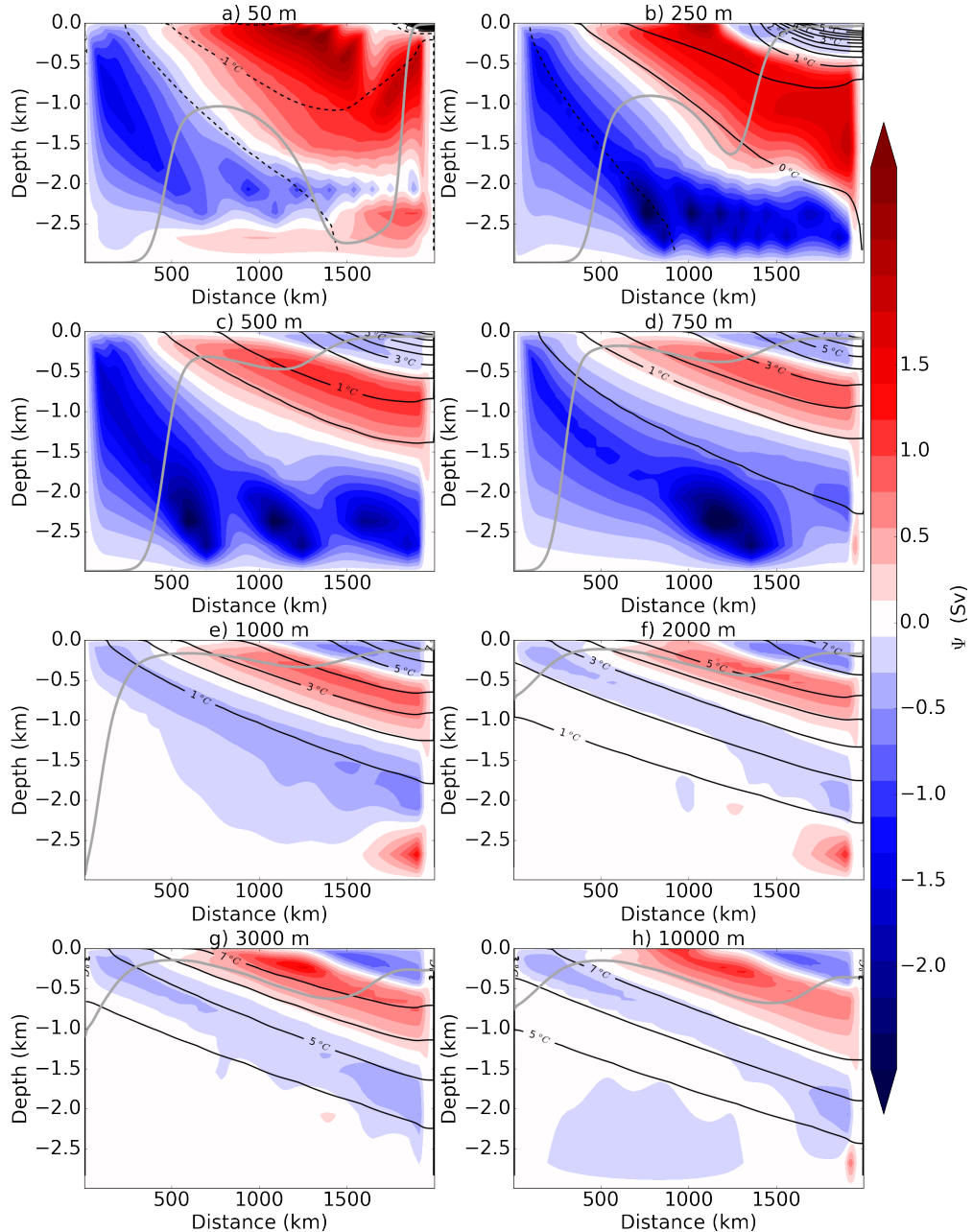


Figure 4.2: The isothermal stream function $\Psi_{res}(y, \theta)$ remapped onto depth coordinates, to give $\Psi_{res}(y, z)$ for various values of N in the sponge layer relaxation profile . Isotherms in multiples of 1°C are overlaid as solid black contours. (Preliminary experiment.)

4.0.3 Direct alteration of northern boundary stratification

As the preliminary experiments revealed that the temperature profile must also be adjusted to make the northern boundary condition consistent with the surface heat fluxes.

$$T^*(z) = \Delta T \frac{(e^{z/N} - e^{-H/N})}{1 - e^{-H/N}} + 2 \left(\frac{N - N_0}{N_0} \right), \quad (4.1)$$

with $N_0 = 1000\text{m}$ and setting setting N max as H for the adjustment term. After which temperature profile is linear. ΔT is given by:

$$\Delta T = \Delta T_0 - \left(\frac{N - N_0}{N_0} \right), \quad (4.2)$$

This gives us the new temperature profiles in fig. 4.3. The maximums and minimums of these profiles are a match with the southern surface minimums and surface maximums seen in the preliminary experiments. The most extreme case $N = 50\text{ m}$ and $N \geq 3000\text{ m}$ required a further degree of adjustment in order to remove unventilated isotherms and or cold water that is never seen at the northern boundary.

To ascertain the direct link between stratification at the northern boundary and the ROC we ran a series of experiments altering $T^*(z)$ by varying N (50m, 250m, 500m, 750m, 1000m, 2000m, 3000m and 100000m). Here for clarity we focus on 4 runs varying N and 4 runs varying ΔT with the altered temperature profiles shown in figure Fig. 4.3.a , which vary from a shallow sharp thermocline to a linear stratification profile. The focus on stratification leads us to run an additional two experiments halving and doubling the temperature range (ΔT) in eq. Eq. (4.3) with an adjustment to prevent unstable circulation:

$$T^*(z) = \Delta T \frac{(e^{z/N} - e^{-H/N})}{1 - e^{-H/N}} + 2 \left(\frac{\Delta T - \Delta T_0}{\Delta T_0} \right), \quad (4.3)$$

where ΔT_0 is again 8°C . Again the maximums and minimums of these profiles are a match with the southern surface minimums and surface maximums seen in the preliminary experiments. The profiles are shown in Fig. 4.3b). All experiments were relaxed with a 3 day relaxation timescale.

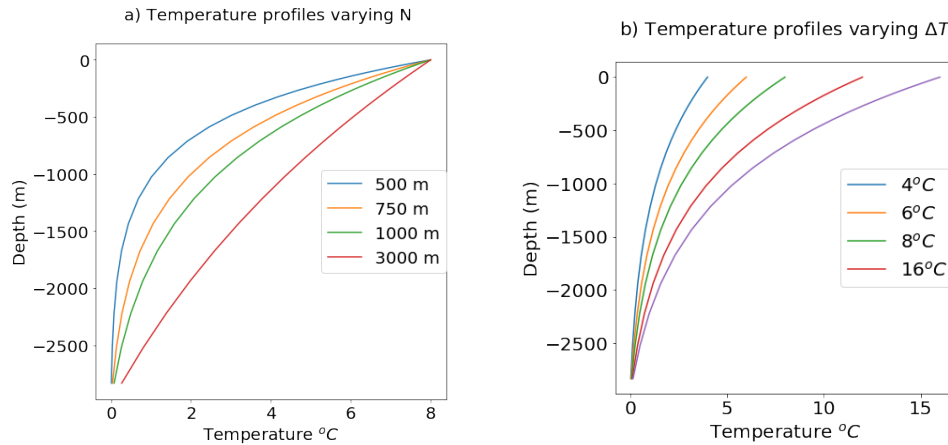


Figure 4.3: New temperature profiles for Sponge layer relaxation for update equations a)Varying N (Eq. (4.1)) and b) Varying ΔT (Eq. (4.3)).

4.0.4 Overturning response

Varying N

Once again the Eulerian mean overturning remains constant at around 2.25 Sv (not shown here). We calculate the iso thermal streamfunction following Eq. (2.13) for $N = 500, 750, 1000, 3000$ m to demonstrate the effect of directly altering the northern boundary stratification.

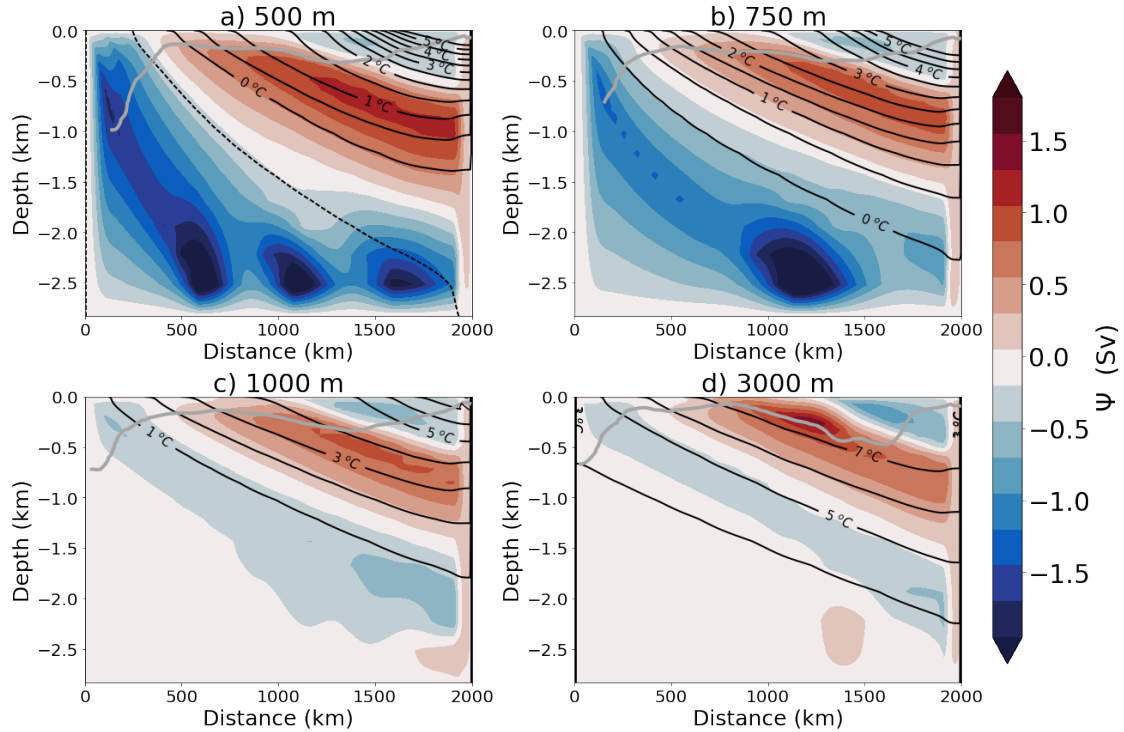


Figure 4.4: The isothermal stream function $\Psi_{res}(y, \theta)$ remapped onto depth coordinates, to give $\Psi_{res}(y, z)$ for a) $N = 500$ m b) $N=750$ m, c) $N=1000$ m and d) $N=3000$ m. Isotherms in multiples of 1°C are overlaid as solid black contours.

Figure 4.4 shows the ROC when these new stratifications are applied. The natural stratification of 1000m used in previous experiments fig. 4.4.c shows the 3 cell ROC we are familiar with. Increasing N depth weakening the ROC as isotherms appear to flatten slightly fig. 4.4.d .When the e-folding length N is reduced we see a steepening of the isotherms in the south of the domain and a shallowing of the isotherms in the upper north of the domain. This leads to a large increase in the lower-most cell - baroclinic instability driven overturning cell fig. 4.4.a-b. The isotherms become almost vertical in the south of fig. 4.4. The clockwise mid-depth cell also intensifies as N is reduced in fig. 4.4. In general we note decreasing N strengthens the SO ROC, however, in the absence of any abyssal stratification the lowermost cell appears to strengthen disproportionately. We see little effect on the surface mixed layer depth, varying only weakly in areas of reduced stratification.

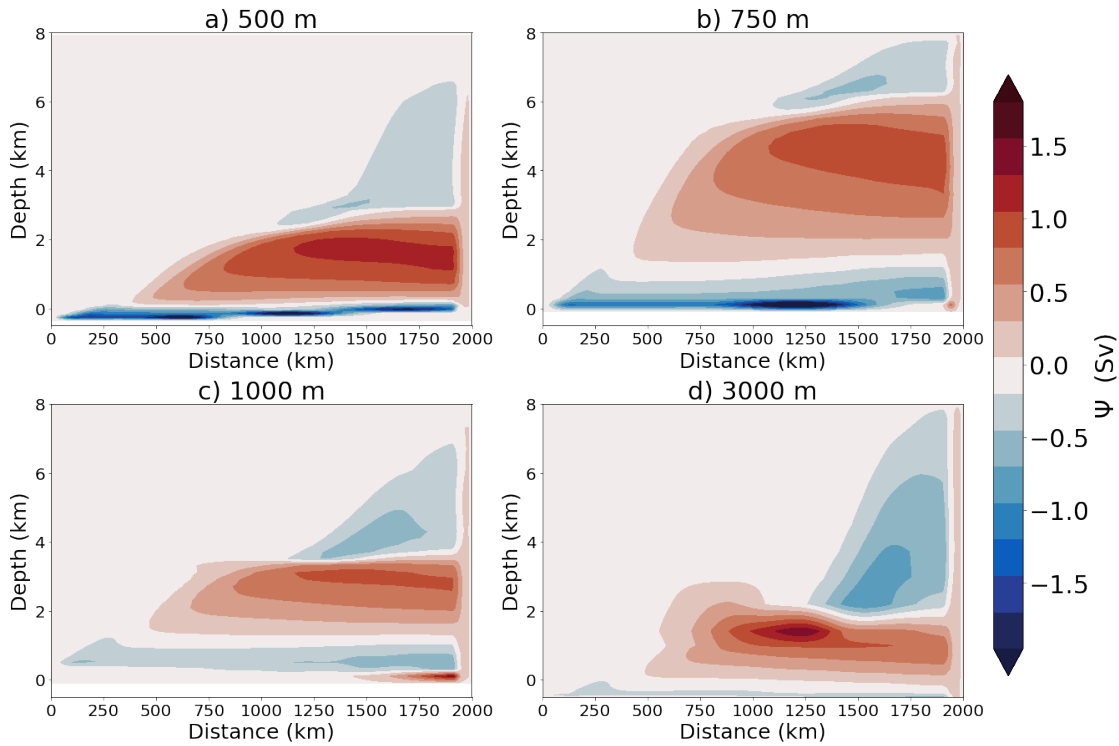


Figure 4.5: The isothermal stream function $\Psi_{res}(y, \theta)$ for a) $N = 500$ m b) $N=750$ m, c) $N=1000$ m and d) $N= 3000$ m.

The changes to the SO ROC are highlighted in temperature space in Fig. 4.5, where the clock wise cell distinctly weakens with Fig. 4.5.d approaching the circulation seen at higher sponge relaxation time scales seen in chapter 2. The SO ROC in temperature spaces gives a much clearer picture of the diminishing lowermost cell and the slightly increasing uppermost cell. This suggests a large shift in baroclinic stability with changing stratification altering the eddy compensation in the channel.

Varying ΔT

The Eulerian mean overturning remains nearly unchanged, but we note a slight deviation when the top bottom temperature difference is doubled. Fig. 4.6 shows that the maxima of overturning remains at ≈ 2.25 Sv but the pattern of strongest forcing in the centre is disrupted slightly. Unlike, many of our experiments we also see and increase in mean kinetic energy for this run as well. This might arise from

the dramatic flattening in isotherms and increase in stratification see in this run. We will investigate further the impacts on the main circulation when we discuss the ACC in chapter 5.

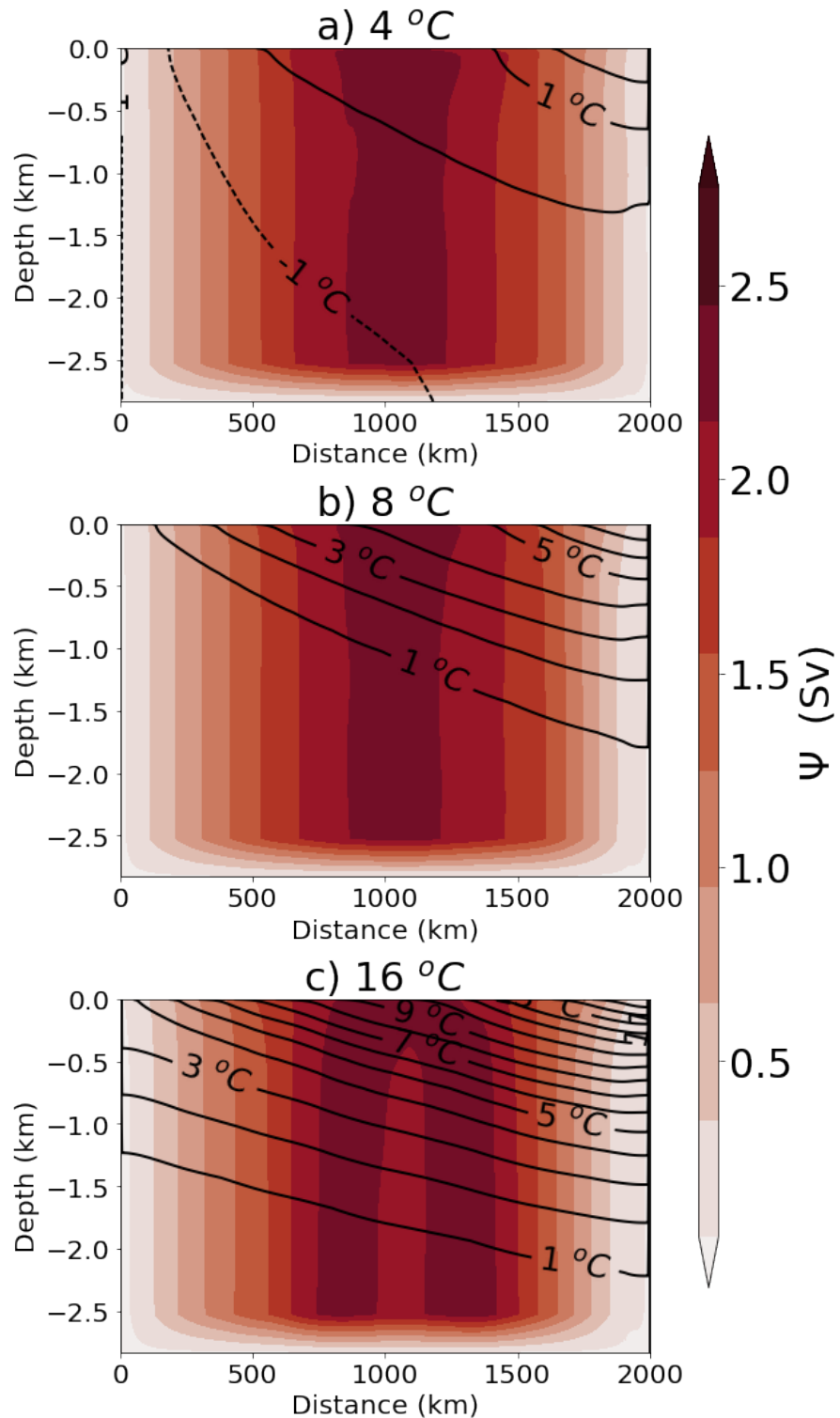


Figure 4.6: Eulerian overturning ($\bar{\Psi}$) for various values of ΔT . Isotherms in multiples of $1^{\circ}C$ are overlaid as solid black contours.

We also see large changes to the SO ROC in response to altering the stratification. This is best shown in temperature space in Fig. 4.7, a more condensed top to bottom temperature range gives rise to a stronger SO ROC and increasing the top to bottom temperature range gives the opposite effect weakening the SO ROC. Fig. 4.7.c forces flatter isopycnals and stratification at depth preventing the lower-most cell from forming (in the absence of topography). Like with increasing N in Fig. 4.5 increasing ΔT leads to shallower isopycnals and weaker ROC.

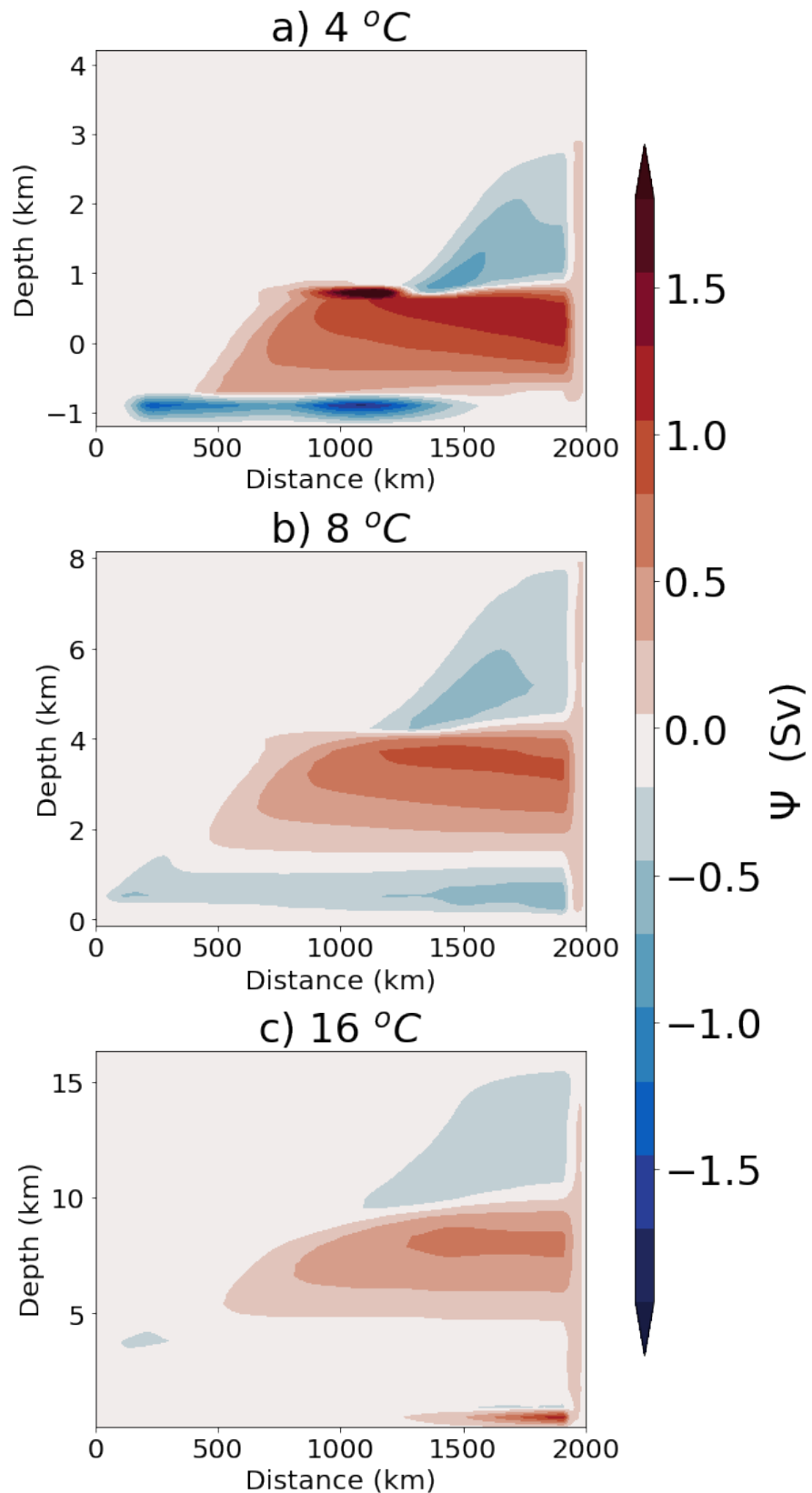


Figure 4.7: The isothermal stream function $\Psi_{res}(y, \theta)$. For various values of ΔT .

Heat Budget

Once again we evaluate the heat budget using equation Eq. (2.5):

$$\underbrace{\frac{\partial \bar{v}T}{\partial y} + \frac{\partial \bar{w}T}{\partial z} + \frac{\partial \bar{v}'T'S_T}{\partial z} + \frac{\partial \bar{v}'T'}{\partial y}}_{\text{Residual } (\nabla \cdot \bar{\mathbf{u}}_{\text{res}} T)} = \underbrace{\frac{\partial Q}{\partial z}}_{\text{air-sea fluxes}} - \underbrace{\frac{\partial (\bar{w}'T' - \bar{v}'T'S_T)}{\partial z}}_{\text{Diabatic eddies}} = \frac{\partial (Q - D)}{\partial z},$$

Plotting the RHS terms in black as the ROC heat divergence and the LHS in blue and red for the diabatic eddy heat flux divergence terms and the surface heat fluxes respectively. Fig. 4.8 shows a simple scenario of the heat flux divergences reducing with increasing N , with Fig. 4.8.d having half the maxima of Fig. 4.8.a.

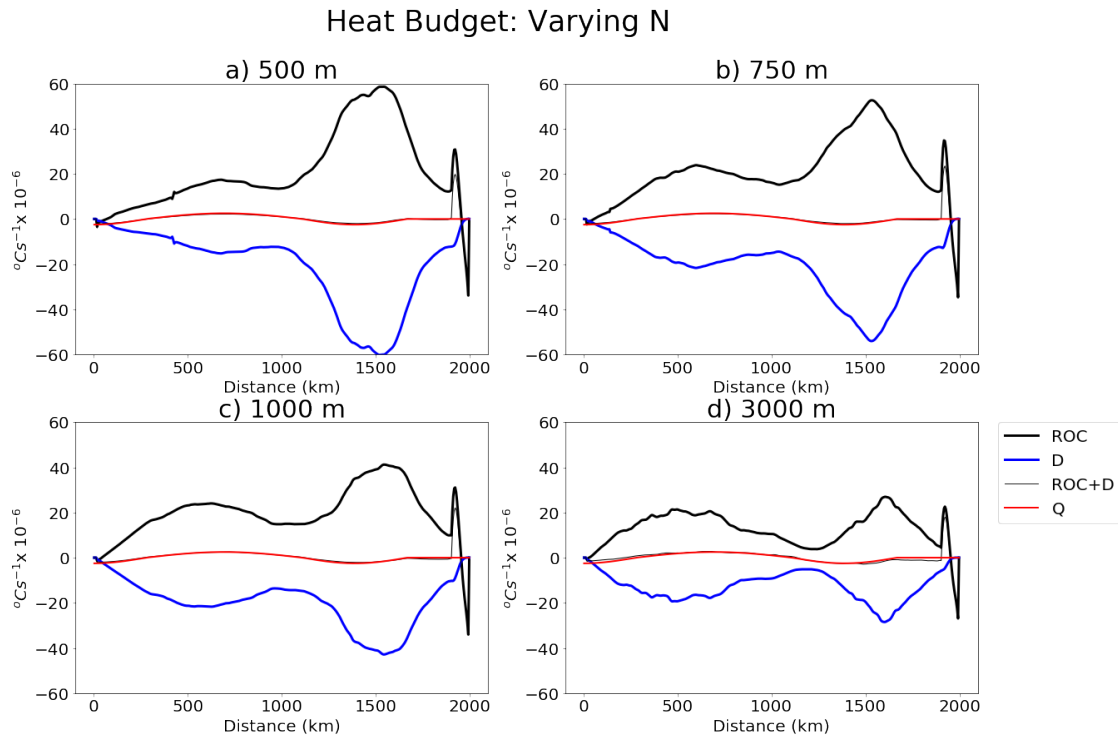


Figure 4.8: The components of the full depth buoyancy budget evaluated in as in Eq. 2.5 for altered sponge layer stratification varying with N . The advective transport component is show in black and diapycnal transport in blue, surface heat forcing in red and the total in thin black line.

This simple story is backed up by plotting the diabatic eddy heat flux divergence term in depth space. Fig. 4.9 shows the diabatic eddy heat flux divergence terms reducing in magnitude with increasing N . Showing the SO ROC can diminish not only through a spatial distribution change in the diabatic eddy heat flux diver-

gence but in a reduction of the fluxes in response to altered northern boundary stratification.

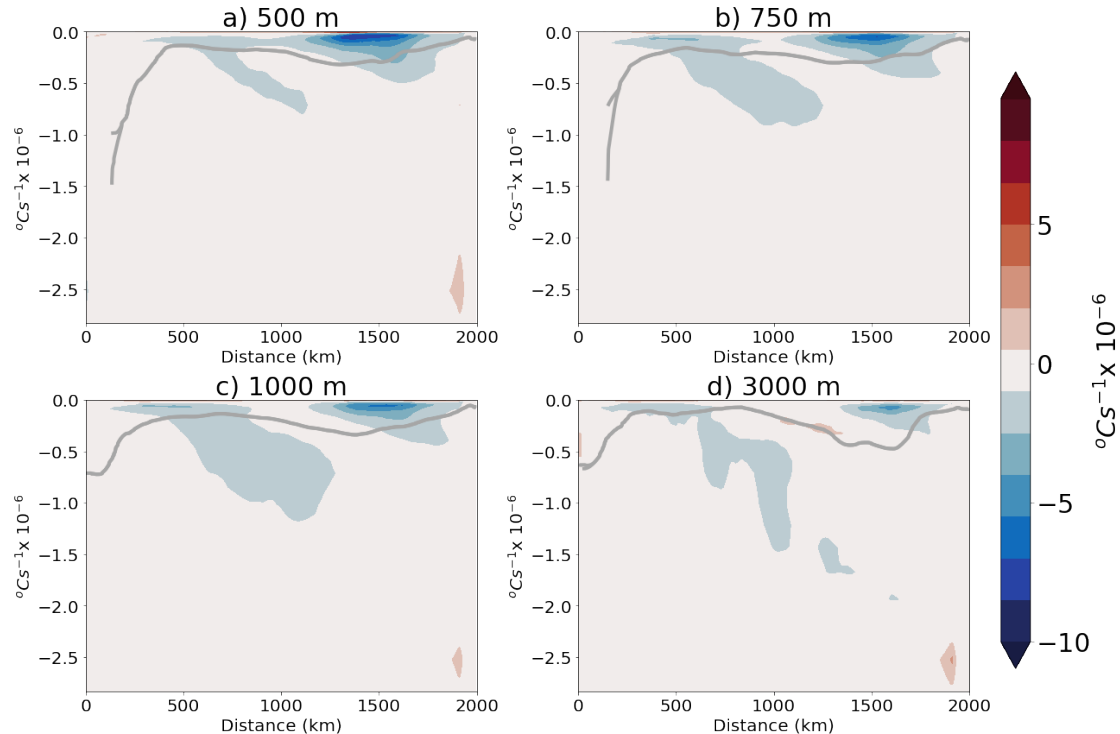


Figure 4.9: Zonal mean diapycnal eddy heat flux divergence for altered sponge layer stratification varying with N.

Varying ΔT

As with varying N altering the top to bottom temperature difference shows a simple scenario of the heat flux divergences increasing with increasing temperature difference ,with Fig. 4.10.a having a third of the maxima of Fig. 4.10.c. However when N is increase we see a reduction in the heat flux divergence magnitude leading to a reduction in SO ROC strength, which is the opposite to what we see in Fig. 4.10.

Heat Budget: ΔT

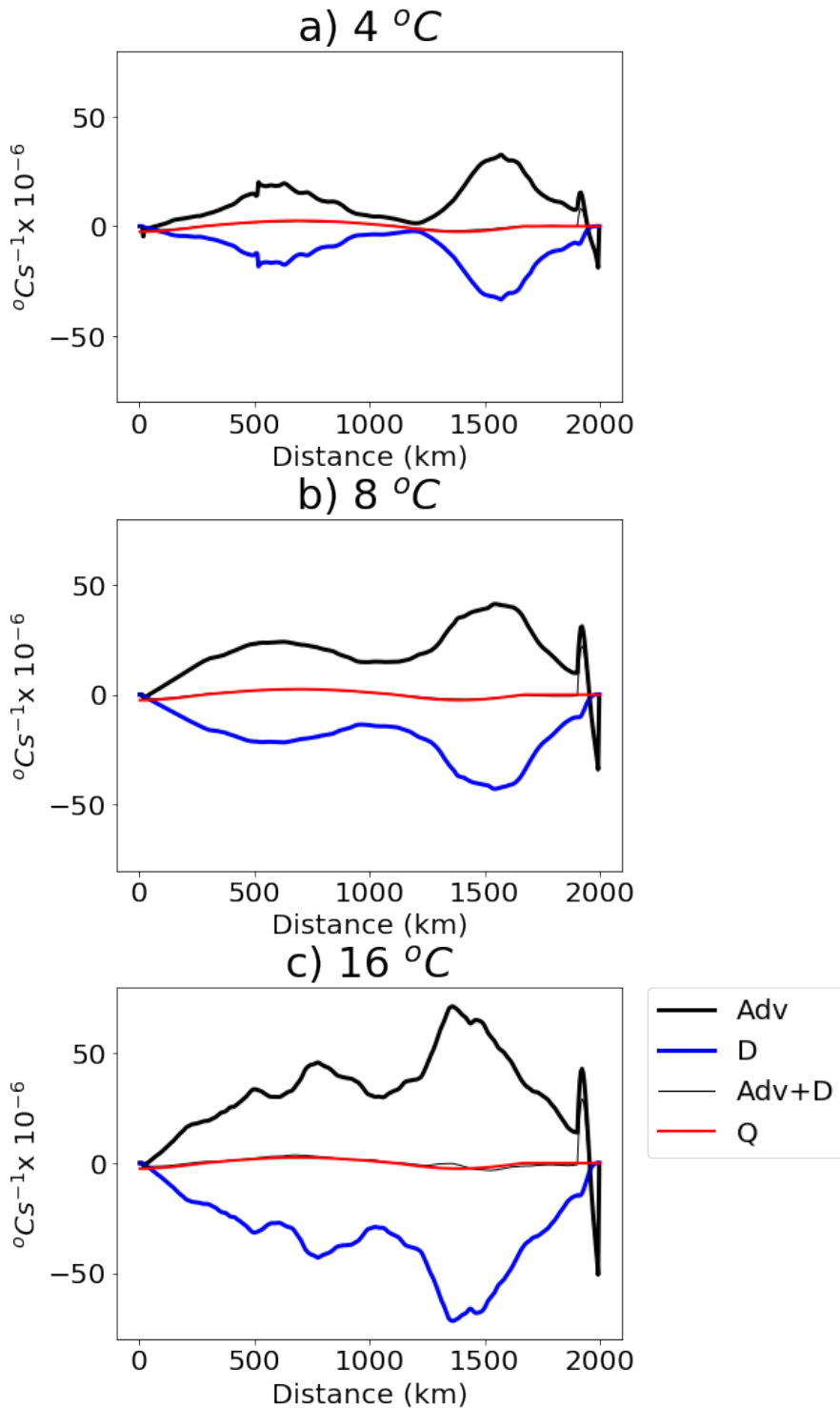


Figure 4.10: The components of the full depth buoyancy budget evaluated as in Eq. 2.5 for altered sponge layer top-to-bottom temperature difference (ΔT). The advective transport component is shown in black and diapycnal transport in blue, surface heat forcing in red and the total in thin black line.

We see a uniform increase in strength of diabatic eddy heat flux divergence when plotted in depth space in Fig. 4.11. Not only the maxima of heat flux divergence increase with increasing ΔT but we also see a much larger area of influence in Fig. 4.11.c . Indicating a deeper influence of diabatic eddies in redistributing heat, this suggests that not only are the magnitude of the diabatic eddy heat fluxes important but their extent of area over which they act.

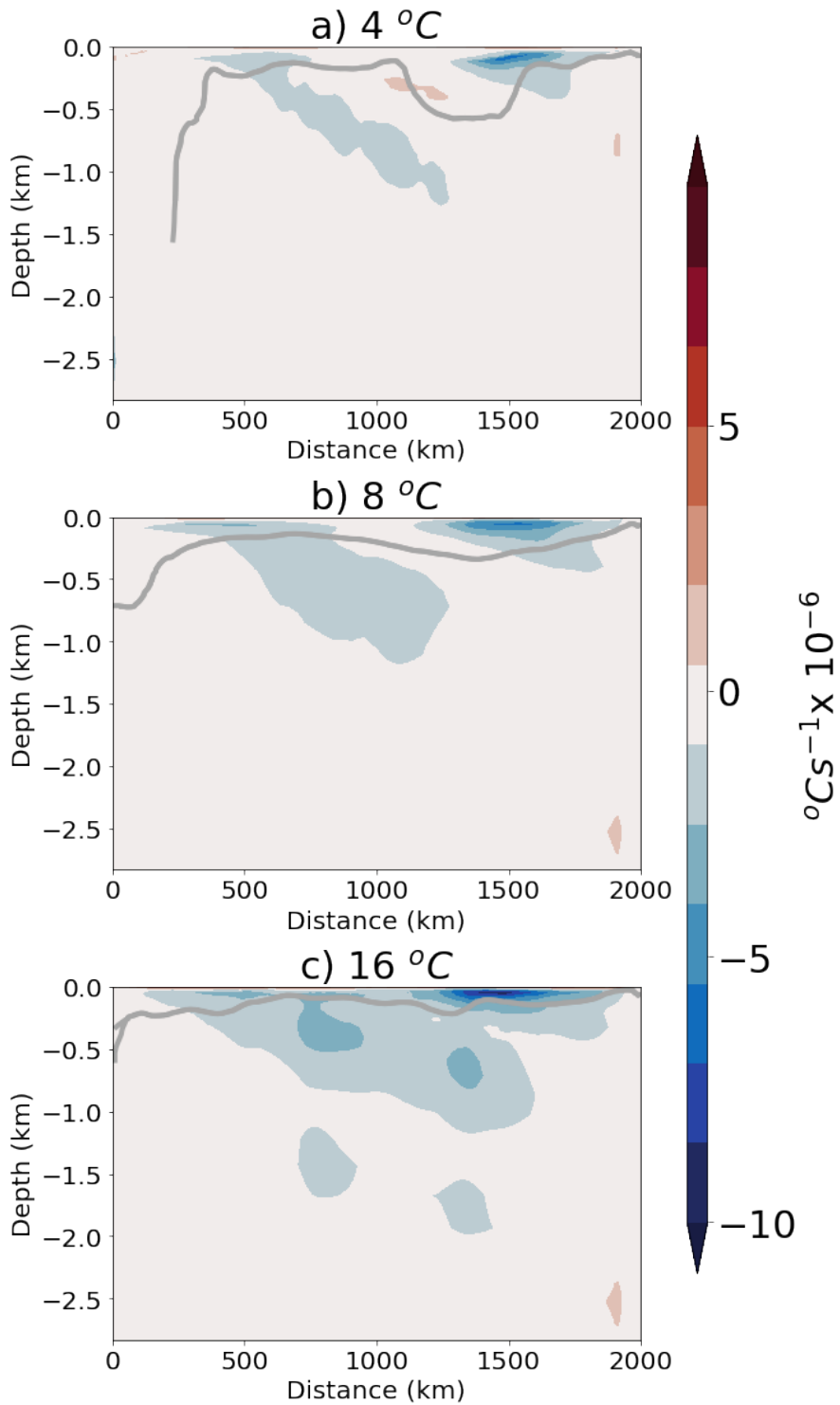


Figure 4.11: Zonal mean diabatic eddy heat flux divergence for altered sponge layer top-to-bottom temperature differences (ΔT).

4.0.5 Energetics

Varying N

As we might suspect due to the change in isopycnal slope and increasing stratification with increasing N. We see a steady decrease in EKE with increasing N in Fig. 4.12.

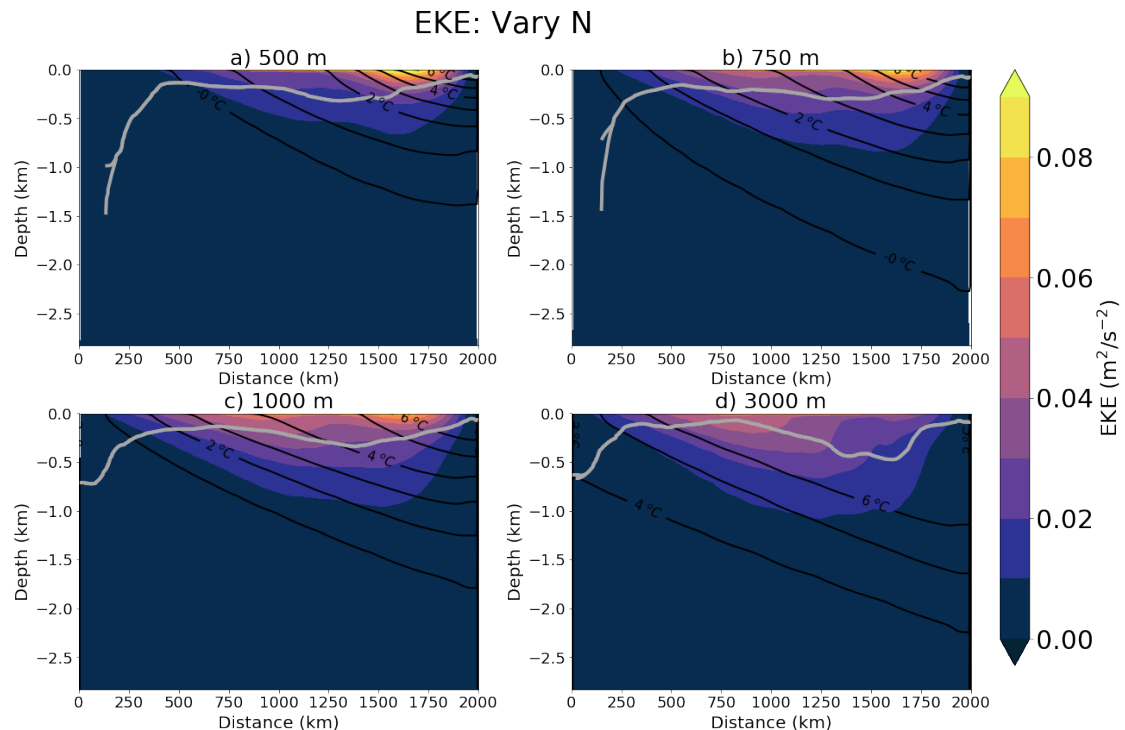


Figure 4.12: Zonal mean EKE, for altered sponge layer stratification varying with N.

This contributes to the decreasing diabatic eddy heat flux divergence and the decreasing SO ROC strength we see when increasing N. Although we note we see a very small increase in Mean Kinetic Energy (not shown here) leading to a smaller decrease in domain total Kinetic Energy.

Varying ΔT

The increasing diabatic eddy heat flux divergence also corresponds to a 5 fold increase in EKE with between $4^\circ C$ and $16^\circ C$. We note here we see a doubling in

the maximum Mean Kinetic Energy (not shown here) leading to a slightly larger increase in domain total Kinetic Energy than the increase from EKE alone.

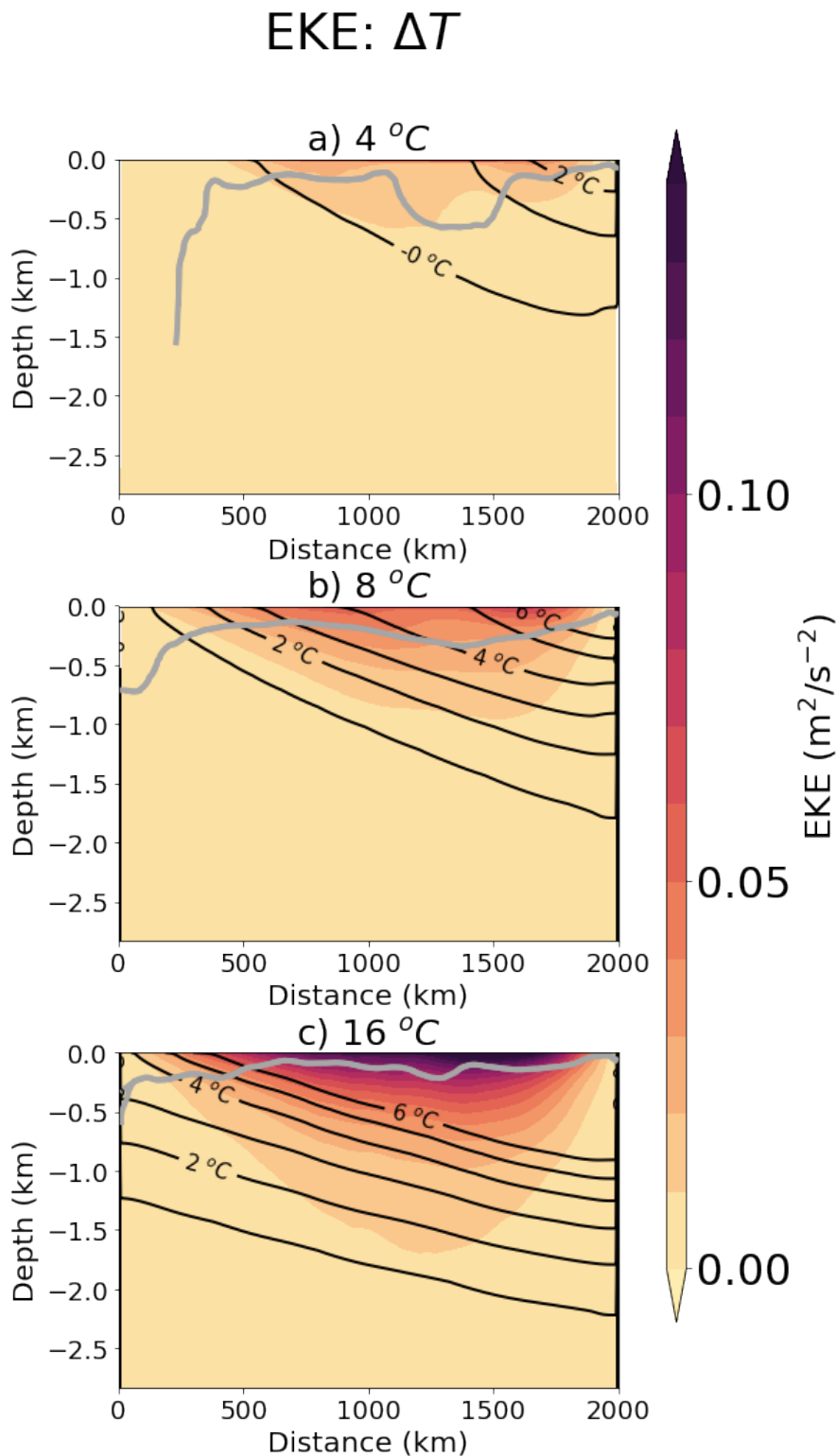


Figure 4.13: Zonal mean EKE altered sponge layer top-to-bottom temperature difference (ΔT).

4.0.6 Conclusions altered boundary conditions

Varying the northern boundary appears to have clear consequences for eddy energetics and the SO ROC, which could promise an interesting direction for further research, what stratification with short relaxation time scales could lead to a full collapse of the SO ROC? We saw in chapter 2 that you can not simply use the profile from the closed scenario with the same forcing. The systematic weakening of the SO ROC with increasing N suggests that there is a possible northern boundary stratification that could be combined with differing surface forcing to collapse the SO ROC without turning off the sponge layer, the diabatic heat fluxes seen in this chapter also suggest that perhaps the strong dipole and deep mixed layer seen in chapter 2 are not required with the right combination of stratification and surface forcing. This would mean differing combinations of surface heat and freshwater fluxes could moderate the SO ROC response changes in the northern hemisphere by altering the response in the diabatic eddy heat fluxes. The idea that stratification plays a role in setting the overturning in the Southern Ocean is not a new one, this has been discussed at great length in numerous studies such as *Ferreira et al.* (2005), where it is pointed out there must be a dependence on N^2 for eddy diffusivity to give eddy stresses in phase with surface winds and surface buoyancy gradient as rationalised in the mixing length hypothesis (*McWilliams and Danabasoglu*, 2002).

Chapter 5

Other considerations

One of the major considerations we have neglected thus far is the influence on topography and the response of the ACC. Although beyond the scope of this thesis to fully include the role of topography on moderating the SO ROC response to altered boundary conditions in a channel model, we can include additional runs to validate and questions our conclusions drawn thus far. In this chapter we show the results for experiments including topography and discuss how this differs from flat bottom runs in the previous chapters.

5.1 Including topography

In the real ocean, the wind stress applied to the surface of the ocean is balanced by bottom stresses and topography plays a leading order role in setting the spatial variability of the eddy field (?) as well as the efficiency of eddy dynamics *Abernathay and Cessi* (2014). The southern ocean has areas of rough topography notably the Kerguelen Plateau and the Macquarie Ridge play large roles in setting steering the ACC and enhancing EKE and eddy mixing. As topography plays an important role in southern ocean dynamics it is important to consider what qualitative impacts it may have in our idealised set up and results.

5.1.1 Set up

As the Southern Ocean is a region of important topographical interactions (*Abernathey and Cessi*, 2014) we checked whether these results also hold in the presence of topography. To investigate this we devised a further set of experiments. The model is once again based on the set up described in section 1.6 and we give a brief overview of the exact set up used here. To this end, we increased the domain size to 4000 km by 2000 km allowing for standing eddies. We also increased the domain depth to 4000 m, increasing the number of vertical grid boxes to 40. We then included a continental slope and 2 complex ridges as shown in Fig. 5.1, similar to that used in previous studies (*Hogg*, 2010). We use partial cells in the MITgcm to account for the topography.

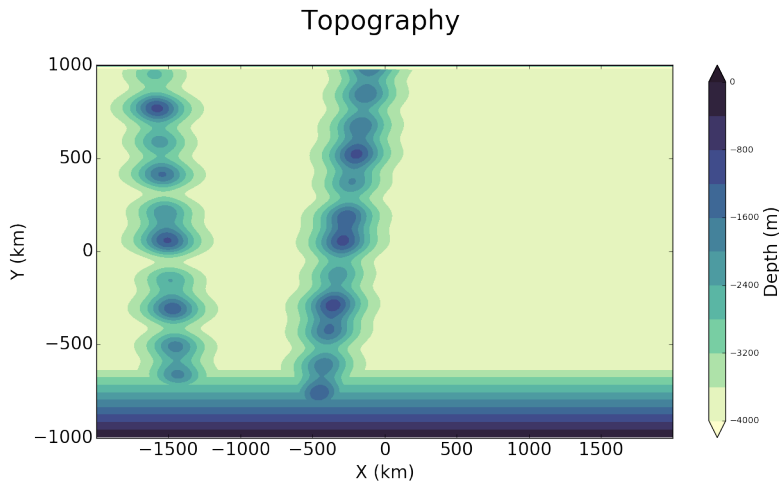


Figure 5.1: Topography included in non-flat bottom runs.

To reduce spurious diapycnal mixing advection scheme 7 was chosen (*Hill et al.*, 2012; *Ilcak et al.*, 2012) and turbulent kinetic energy (TKE) scheme (*Gaspar et al.*, 1990; *Madec and Delecluse*, 1998) was employed to parametrize sub grid mixing. Key model parameters are outlined in Table 5.1.

Table 5.1: Model Setup for fixed-flux runs with topography.

| Symbol | Description | Value |
|---------------|-------------------------------------|--------------------------|
| L_x, L_y, H | Domain | 4000 km, 2000 km, 4000 m |
| L_{sponge} | Length scale of sponge layer | 100 km |
| Q_0 | Surface heat flux magnitude maximum | 0-10 W m ⁻² |
| τ_0 | Max surface wind stress | 0.2 N m ⁻² |
| dx, dy | Horizontal grid spacing | 5 km |
| dz | Vertical grid spacing | 5-266 m |
| Adv Scheme | 7 th order centred | 7 |
| τ_R | Sponge relaxation time scale | 3-day and ∞ |

The surface heat and wind forcing remain unchanged from the fixed flux runs.

To test the effect of topography we ran 2 experiments for the 2 extreme relaxation timescales: 3 days and infinite (closed northern boundary). These simulations were run for 400 and 1000 years respectively.

5.1.2 Overturning

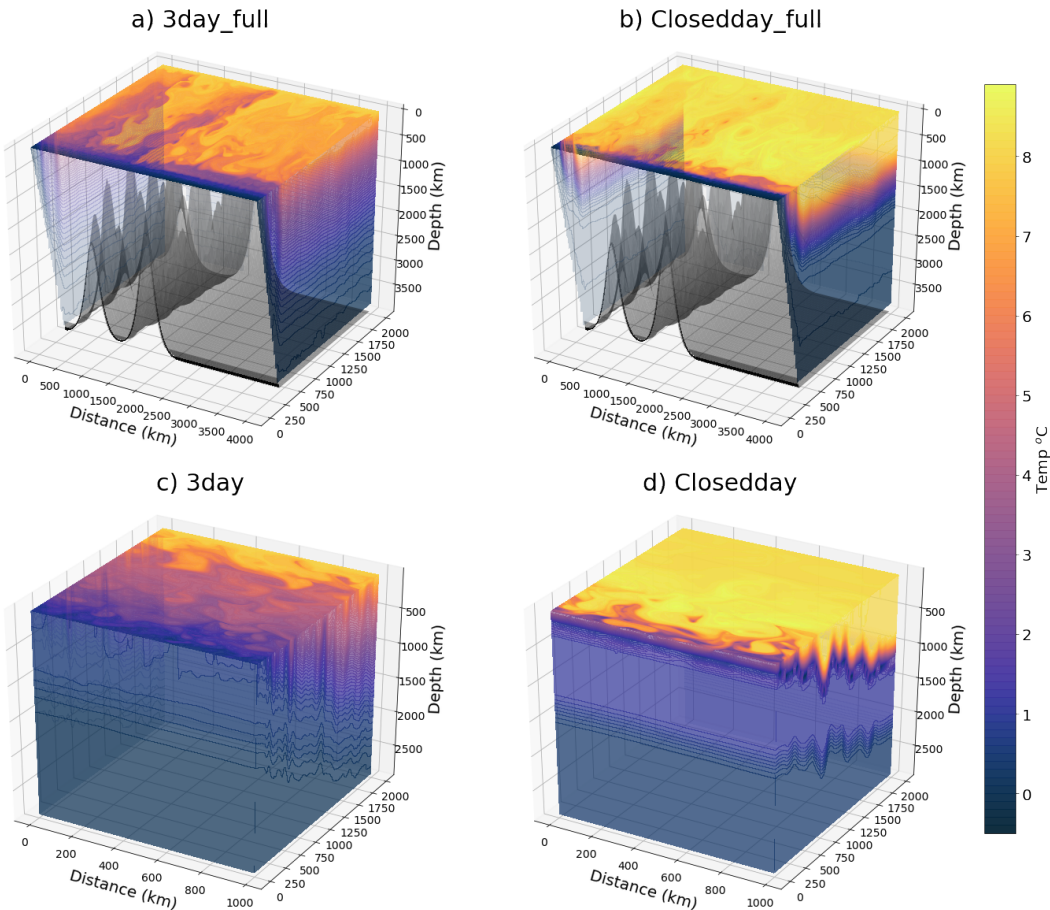


Figure 5.2: Instantaneous temperature field for a) and b) Topography runs. c) and d) flat bottom runs.

First we plot at the 3D instantaneous temperature field for both the flat runs and runs with topography (shown in grey) to highlight the main differences we see increased variability in in the topography runs Fig. 5.2.a-b and flatter isotherms. We still see a boundary layer form in the closed run. As with all runs we check the Eulerian mean overturning looks sensible and consistent with all other runs. Fig. 5.3 shows the Eulerian MOC with topography is around 6 times larger (15 Sv) than the flat bottom runs (2.25 Sv). This increase is as expected with the 4 times increase in channel length alongside a 25% increase in depth.

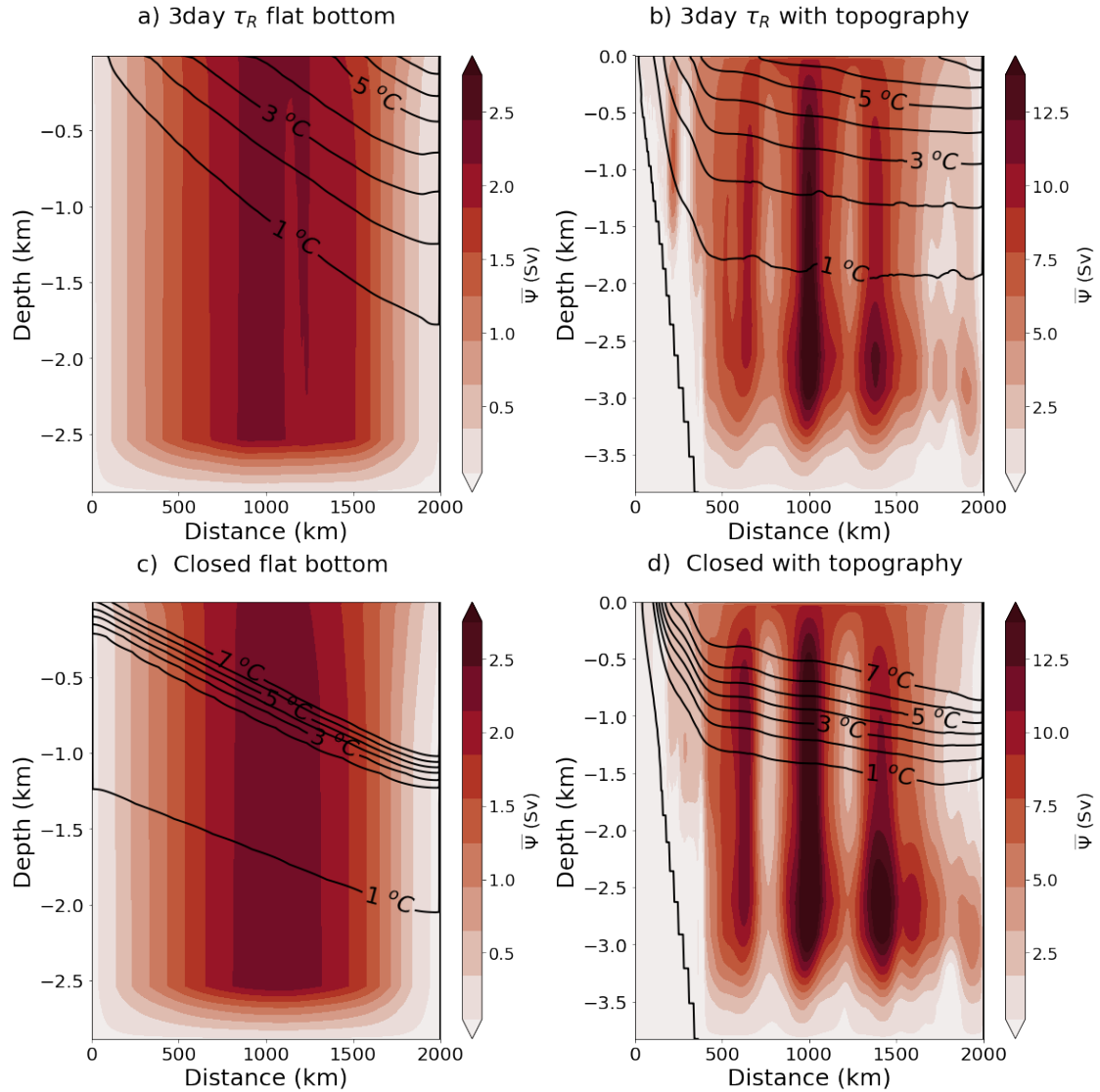


Figure 5.3: The Eulerian mean streamfunction ($\bar{\Psi}$) for Flat bottom runs a) and c) and for Topography runs b) and d).

We also see a different structure in the runs with topography Fig. 5.3, which is seen as a loped structure in b and d. This pattern is seen to be unchanged between averaging periods of 20 years to 100 years. Our ridges have some shallow peaks extending into the upper 1000m (as does the real southern ocean topography (??)) of the ocean and the lobes may be due to the locations of the peaks as the overturning circulation must be above the topography (*Viebahn and Eden, 2012*). As the "Deacon cell" (*Döös and Webb, 1994*) is a fictitious cell we will not focus on the structure of the Eulerian mean overturning but will consider interaction with the mean flow in other analysis.

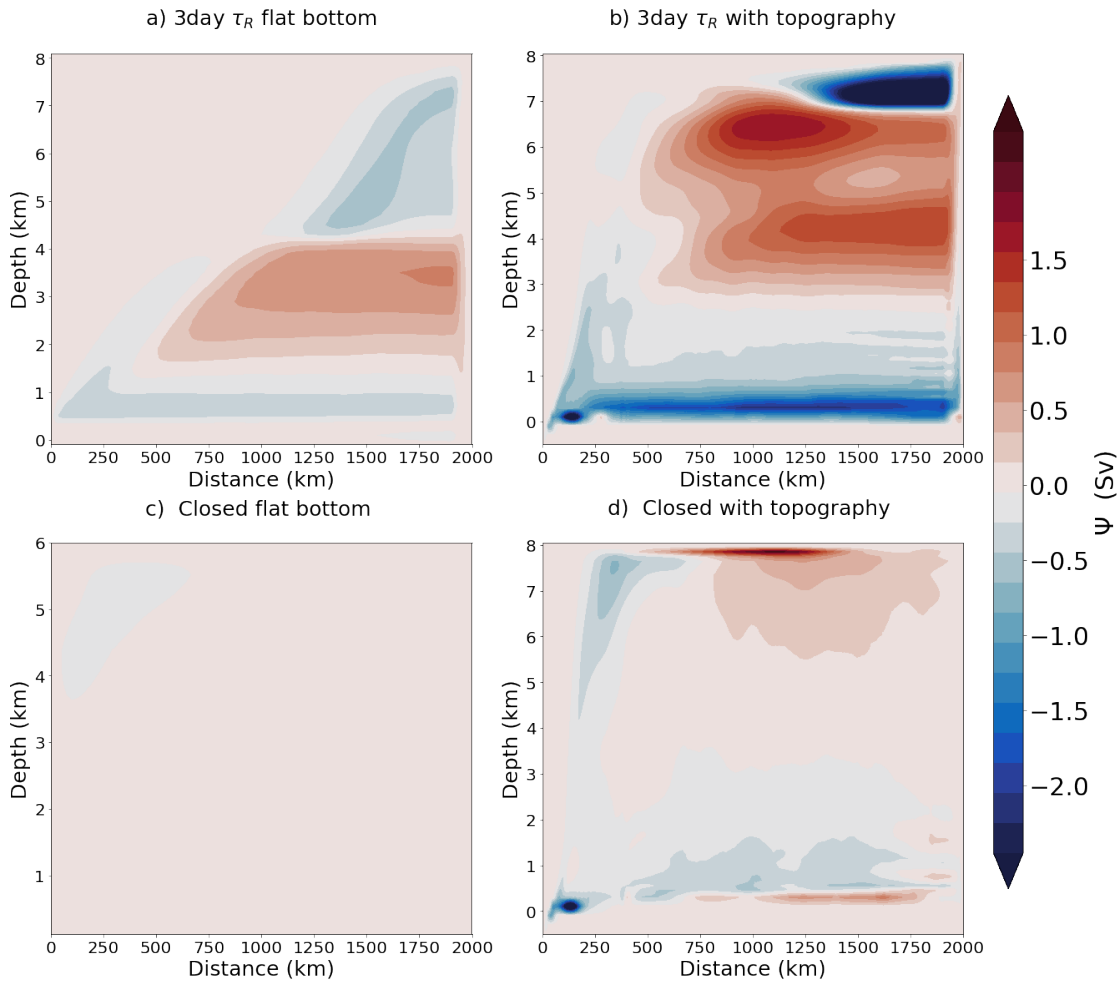


Figure 5.4: The isothermal stream function $\Psi_{res}(y, \theta)$ for relaxation time scales of 3 and infinite days for flat bottom a) and c) runs and topography runs b) and d).

As with the previous chapters we calculate an isothermal stream function to show the ROC. However for the topography runs we calculated the stream function over 82 discrete potential temperature layers, in order to account for areas with little temperature variation at depth. The isothermal stream function is shown in Fig. 5.4, showing a similar 3 cell ROC pattern aligned with isotherms. Fig. 5.5.b shows that the SO ROC remapped into depth in these runs closely matches the 3 cell circulation in the flat bottom runs which collapses ¹. The overturning strength is a factor of 5 stronger as expected with the longer channel. We discuss here the qualitative differences between the equivalent runs with flat bottoms. in

¹The full spin up of the closed boundary run would take 3000 years, which is computationally too expensive. However, we know from the flat bottom experiments that the intense surface wind driven cell will disappear after 1000 years.

Fig. 5.5.b demonstrating that the fundamental ideas of how the SO ROC responds to stratification changes in the north of the domain still hold in models including topography. It should be noted that the lowermost cell of the SO ROC is still unrealistic in this idealised set up, as it is driven by diabatic processes not included in the idealised model. Its disappearance in these runs even in the presence of topography is not further discussed.

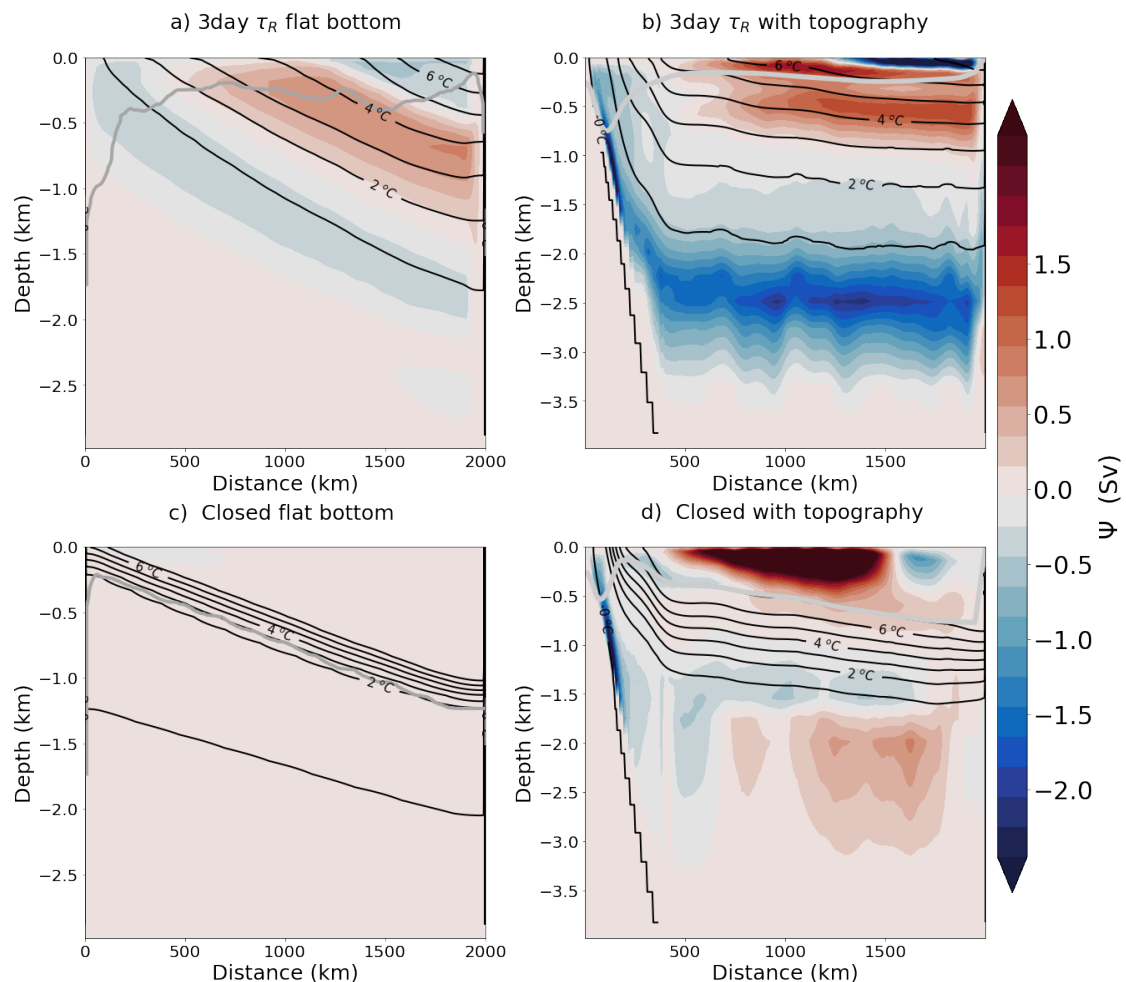


Figure 5.5: The isothermal stream function $\Psi_{res}(y, \theta)$ remapped onto depth coordinates, to give $\Psi_{res}(y, z)$ for relaxation time scales of 3 and infinite days for flat bottom a) and c) runs and topography runs b) and d). Isotherms in intervals of 1°C are overlaid as solid black contours. Above the surface heat forcing is displayed.

As well as the 3 cell SO ROC and its subsequent collapse we see that the same pattern of stratification change between the open and closed northern boundary case in the presence of topography. The sharp internal boundary layer that forms in the closed scenario appears much less sharp in the runs with the topography runs.

We also see a shallowing of the mixed layer depth in the presence of topography for both the open and closed scenarios. Shoaling from 1200 m at the northern boundary in Fig. 5.5.c to 500 m in Fig. 5.5.d.

5.1.3 Dynamics

Topography has a large influence on eddy dynamics with standing eddies playing a large role in eddy heat fluxes. However if we look at the depth profile of the eddy heat fluxes in Fig. 5.6 we see a reduction in magnitude between topography and no topography runs, but the same general pattern between open and closed northern boundaries. Notably we see a large deviation in the total heat flux between flat and topography runs with topography having larger downwards heat fluxes Fig. 5.6.b and d.

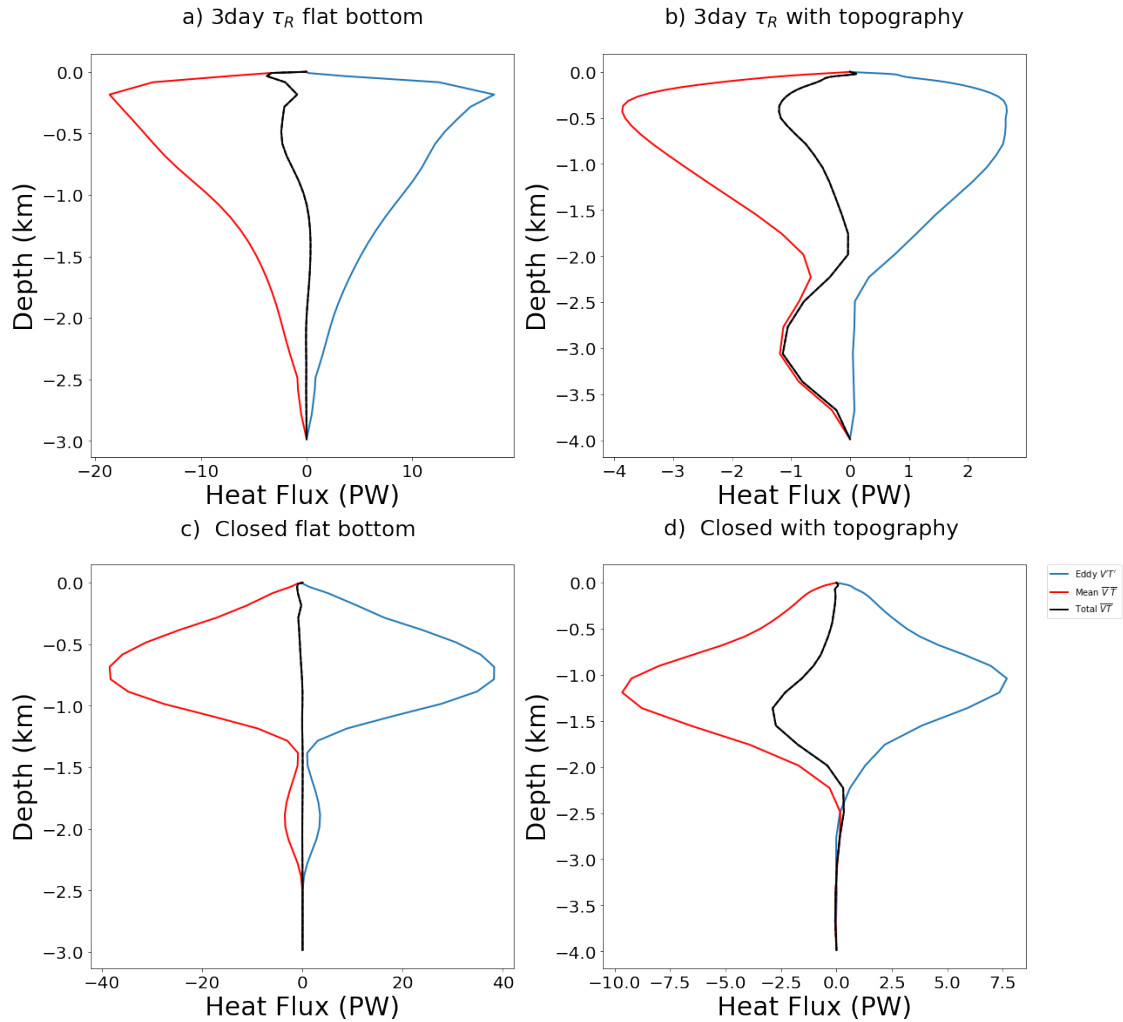


Figure 5.6: Vertical eddy heat flux (PW) for flat bottom runs a) and c) and topography runs b) and d). Mean vertical heat flux ($\bar{w}\bar{T}$) is show in red, Eddy($\bar{w}'\bar{T}'$) in blue and Total ($\bar{w}\bar{T}$).

We can see this in the diabatic eddy heat flux divergence terms. The vertically integrated values shown in Fig. 5.7 show the convergence in uniform bands in the Fig. 5.7.a and c however we see locally very enhance divergence and convergence around topography Fig. 5.7.b and d at over 100 times larger magnitude but confined to very short zonal areas except for over the continental shelf showing that although the net effect cancelling out the SO ROC still holds this is achieved around topography in strong dipole patterns.

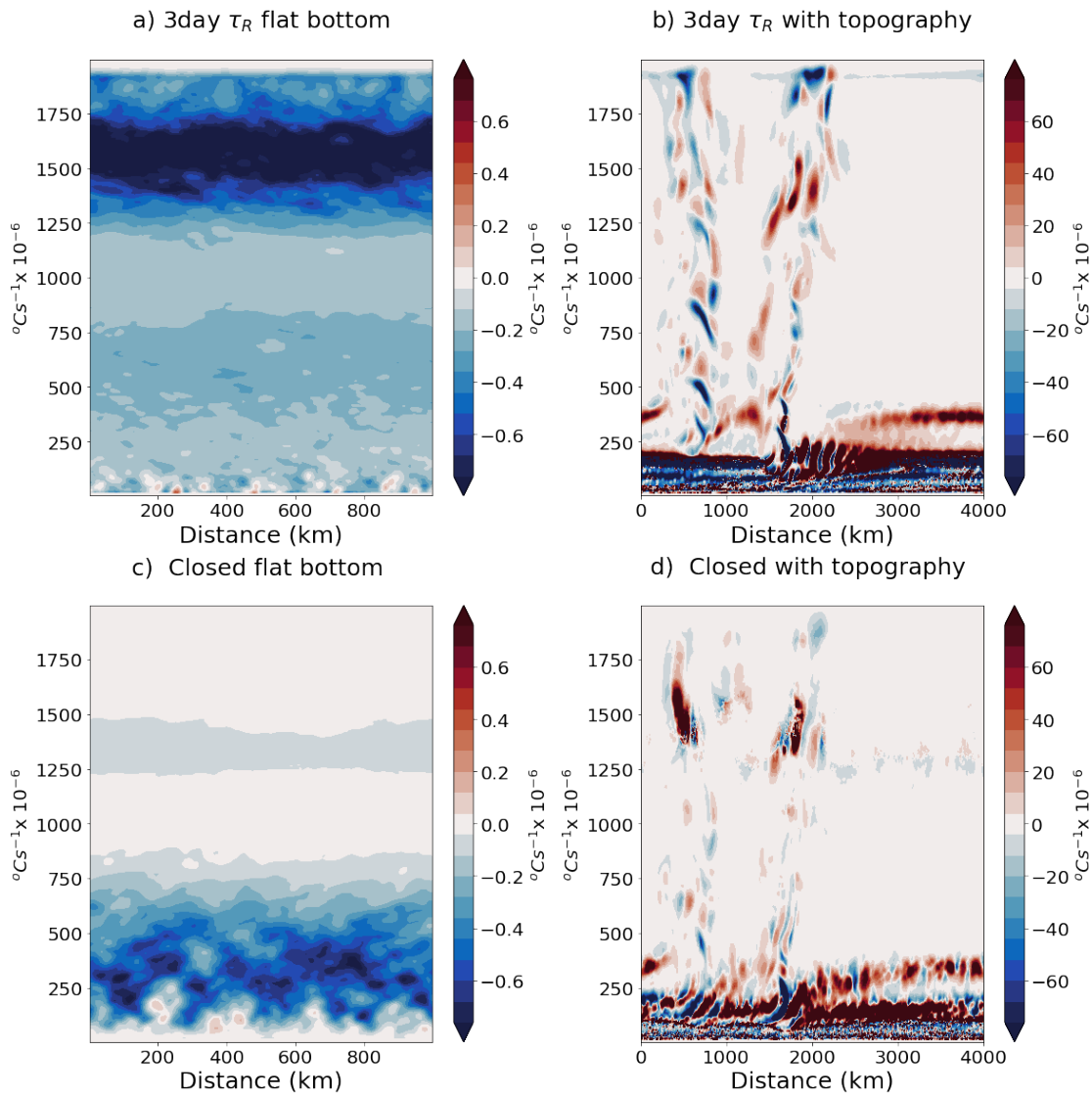


Figure 5.7: Vertical integrated diapycnal eddy heat flux divergence, for flat bottom runs a) and c) and topography runs b) and d).

Energetics

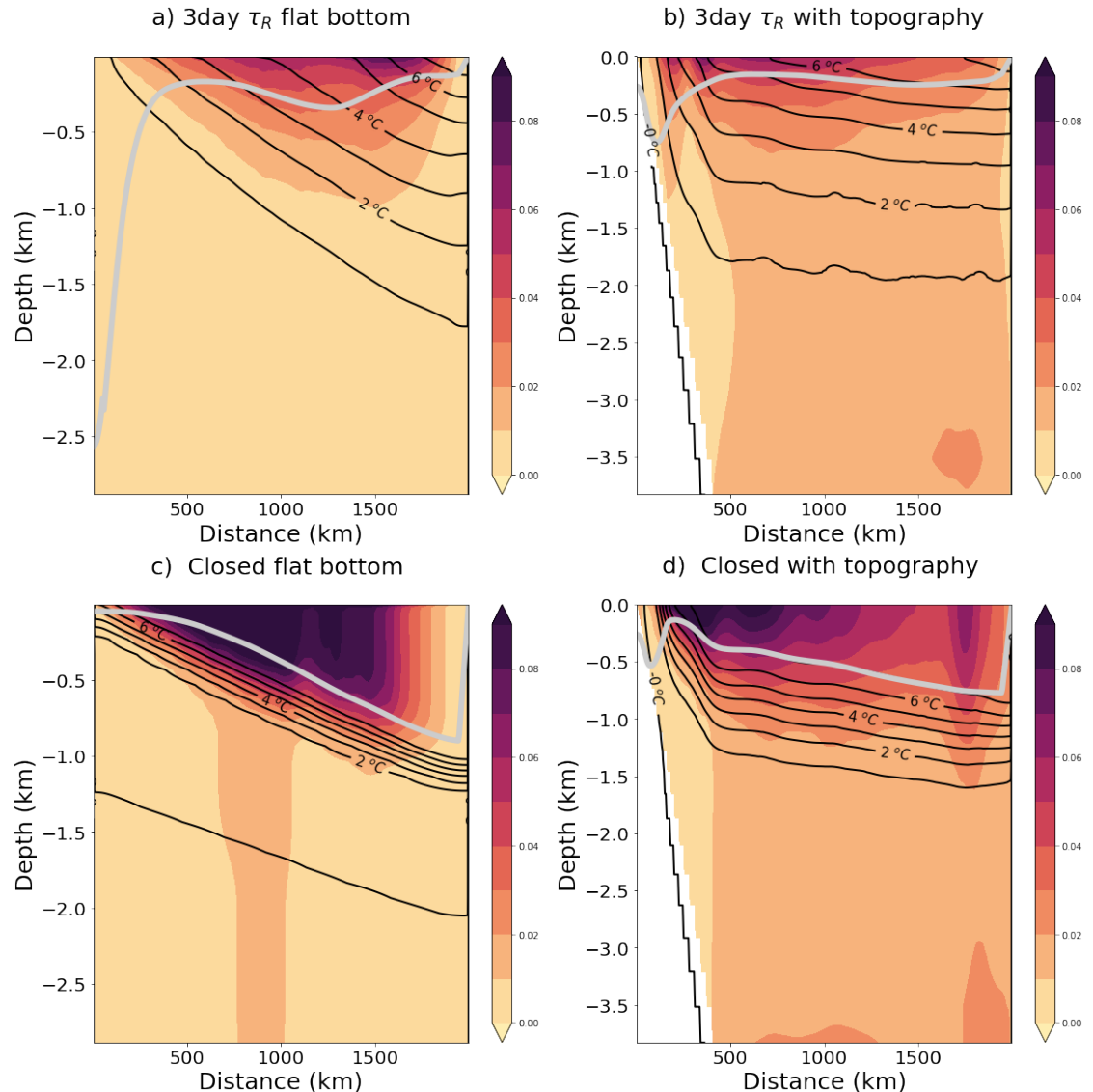


Figure 5.8: EKE $\frac{1}{2}(u^2 + v^2)$ sections for relaxation time scales of 3 and infinite days for flat bottom a) and c) runs and topography runs b) and d). Isotherms in intervals of 1°C are overlaid as solid black contours.

In presence of topography we see an similar magnitudes of EKE maxima (within 10%) to the flat bottom scenario but a much higher domain average (greater than twice flat bottom domain average).

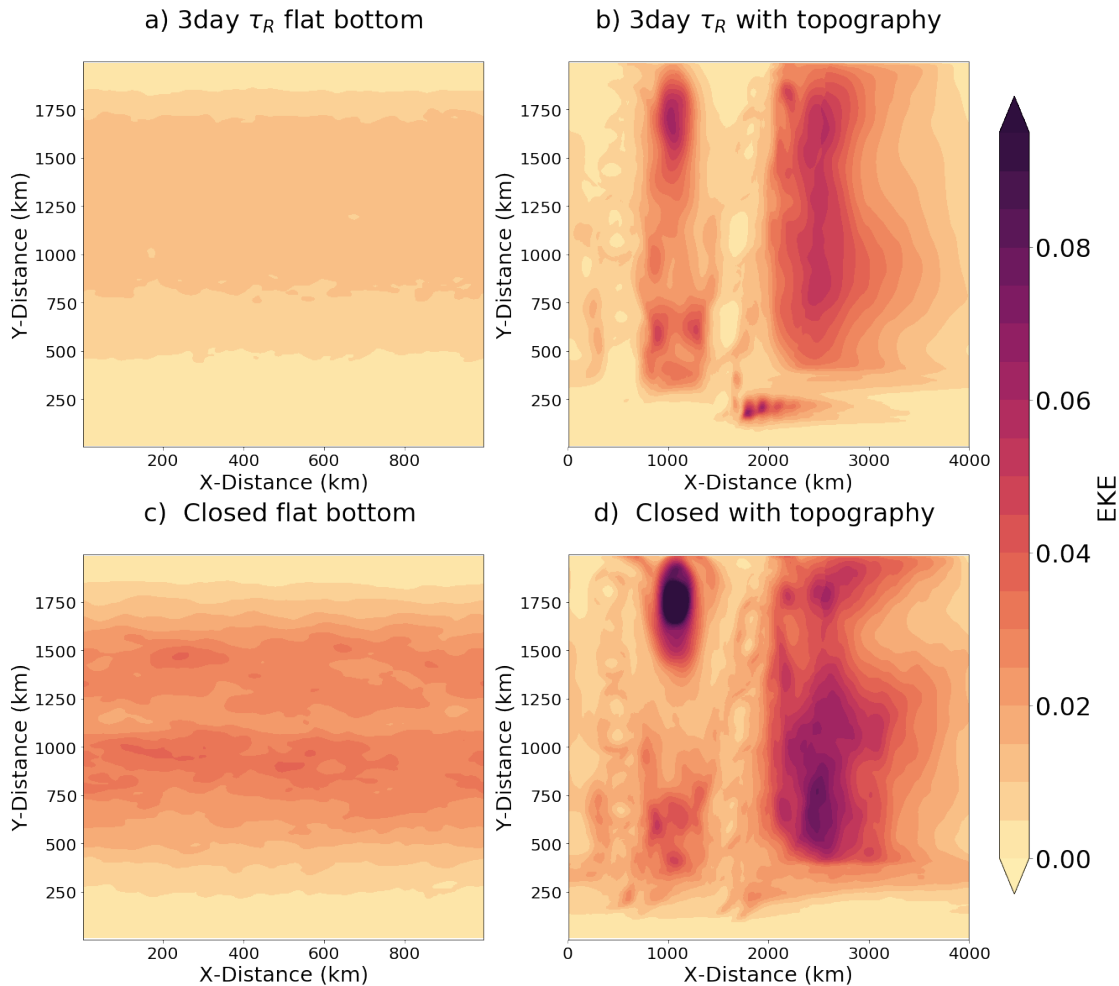


Figure 5.9: Vertically integrated EKE $\frac{1}{2}(u^2 + v^2)$ for relaxation time scales of 3 and infinite days for flat bottom a) and c) runs and topography runs b) and d).

As zonal means are not very appropriate in the presence of topography it is best to look at the vertically integrated EKE. As expected from satellite altimeter data EKE in the southern ocean is patchy with large enhancement downstream of topography (?).

5.2 ACC

Part of the unique dynamics as discussed in the introduction is the ACC like the SO ROC the ACC is driven by wind and buoyancy forcing. In our channel runs we have seen large changes in EKE and stratification and although wind forcing

is kept constant we are likely to see a response in the ACC. The ACC is set by a number of factors: Wind Stress (τ), Surface buoyancy forcing and remote forcing altering stratification the most basic way of calculating transport is:

$$T = \iint u dz dy \quad (5.1)$$

If you substitute thermal wind into Eq. (5.1), where thermal wind is given as:

$$u_z = \frac{u_z}{f \rho_0} \rho_y \quad (5.2)$$

Transport can be written:

$$T = \frac{g}{f \rho_0} \iint \rho_N - \rho_S dz^2 \quad (5.3)$$

Showing the role of stratification in setting ACC strength (?).

5.2.1 The ACC response to altered northern boundary conditions

We examine here what happens to the ACC when you alter the northern boundary condition with fixed surface fluxes. To illustrate this we have looked at the fixed surface heat flux and surface restoring runs to see how the closing of the northern boundary effects the ACC as well as the surface boundary condition.

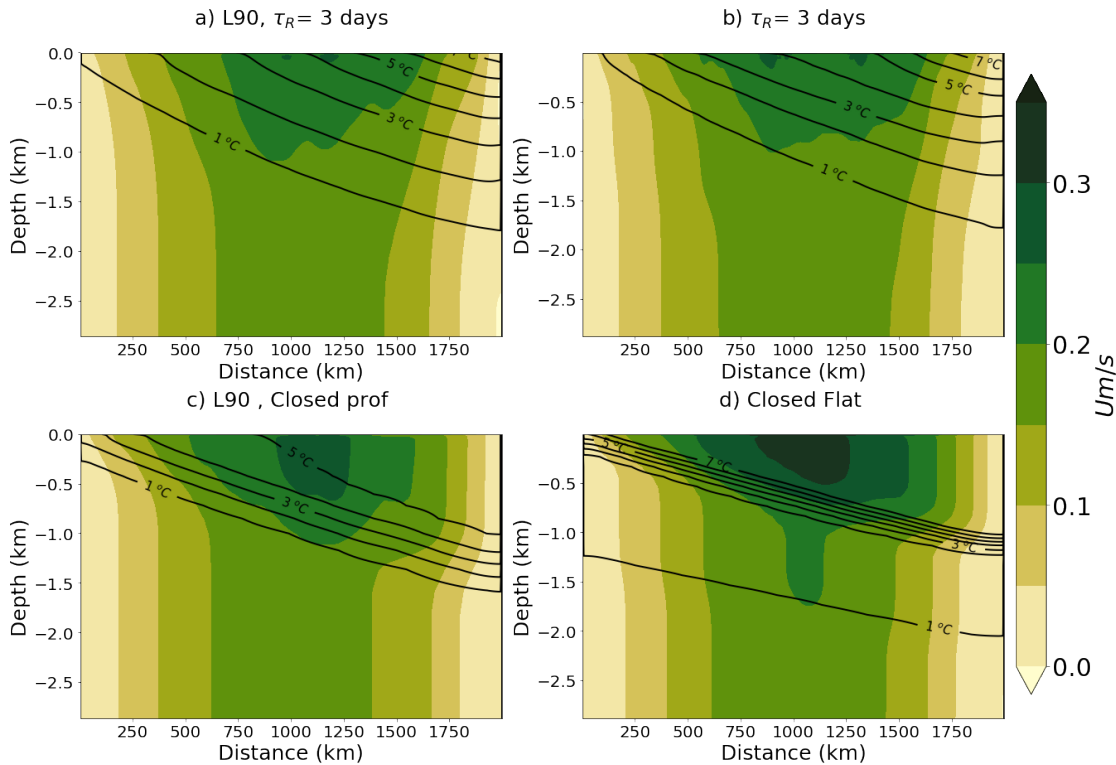


Figure 5.10: Zonal mean zonal velocity \bar{u} m/s for a) Surface restoring with strong sponge layer, b) fixed heat fluxes and strong sponge layer, c) Surface restoring with Closed northern boundary and d) fixed heat fluxes with a closed northern boundary.

From varying the relaxation timescale at the northern boundary the ACC varies drastically, particularly the baroclinic component. Fig. 5.10 show how little surface boundary conditions affect the zonal velocities. A very slight increase in velocity is noted with the marginally steeper isotherms in the fixed surface flux runs Fig. 5.10.b-d. For both surface heat forcing conditions we see the large effect that closing the northern boundary has on the zonal flow. When the northern boundary is closed a very large temperature (density) difference is achieved from the North of the ACC to the South with the sharp boundary layer leading the same difference across the ACC as the entire top to bottom temperature difference.

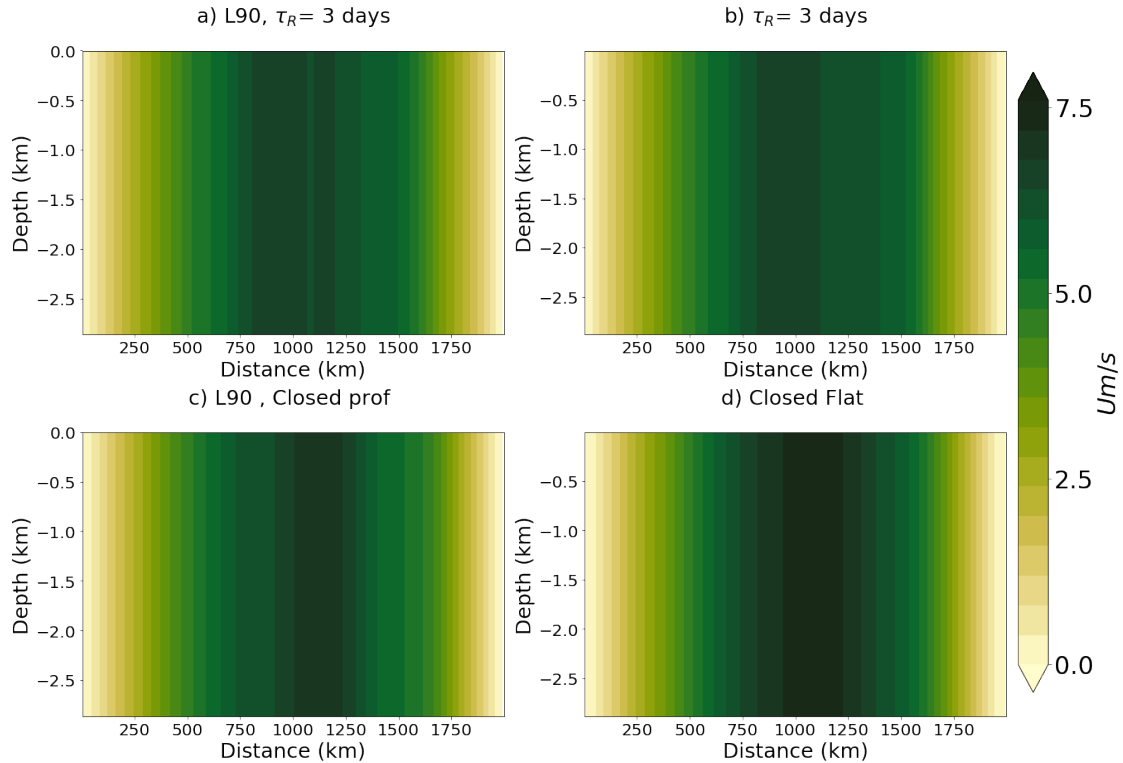


Figure 5.11: Zonal mean barotropic component of zonal velocity for a) Surface restoring with strong sponge layer, b) fixed heat fluxes and strong sponge layer, c) Surface restoring with Closed northern boundary and d) fixed heat fluxes with a closed northern boundary.

Breaking down into barotropic (Fig. 5.11) and baroclinic (Fig. 5.12) components we see that the surface heat forcing has little effect on the transport with a 3 day relaxation timescale. The major changes between open and closed northern boundary occurs in the baroclinic component although a slight increase in the barotropic component is noted. Interestingly the barotropic transport is more noticeably increased when the northern boundary is closed with fixed surface heat fluxes, this could suggest that the choice of surface heat forcing has an effect on degree of eddy saturation which corroborates the findings of *Zhai and Munday* (2014) who found shorter time scales of surface restoring increased eddy saturation.

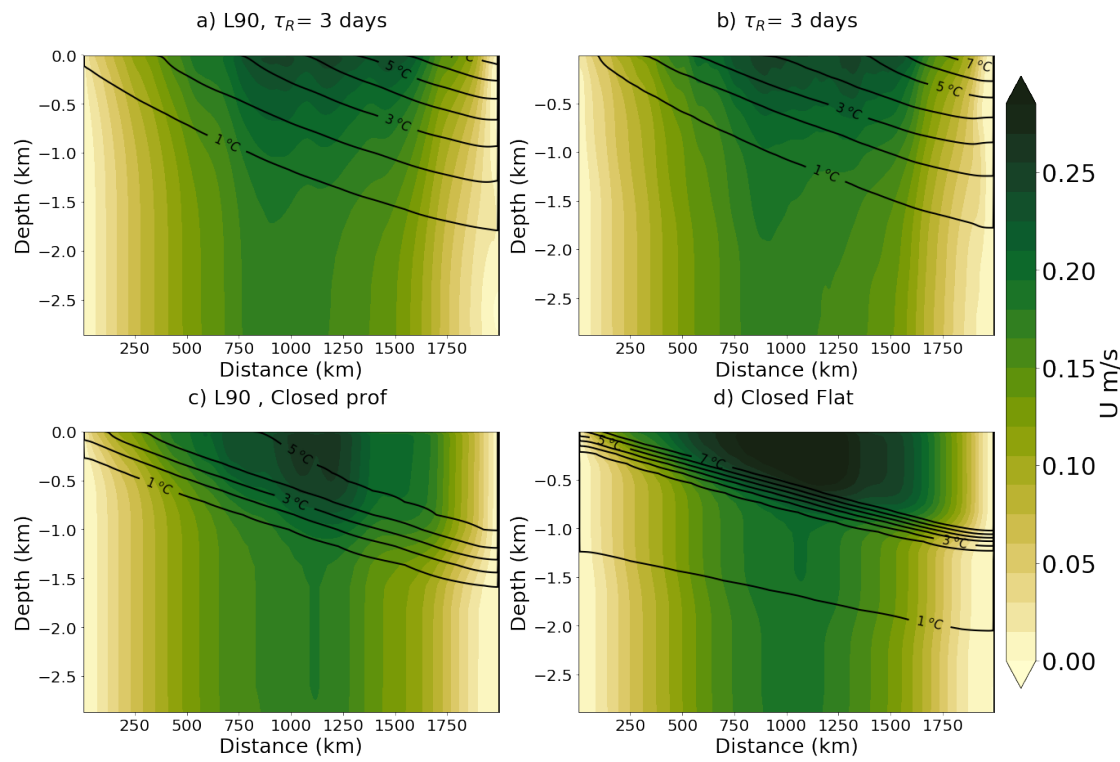


Figure 5.12: Zonal mean baroclinic component of zonal velocity for a) Surface restoring with strong sponge layer, b) fixed heat fluxes and strong sponge layer, c) Surface restoring with Closed northern boundary and d) fixed heat fluxes with a closed northern boundary.

When the northern boundary is closed we see a large increase in baroclinic transport, this increase is mostly seen in the surface mixed layer but we see this increase extend to depth.

Chapter 6

Discussion

6.0.1 Closing the Northern Boundary

Motivated by the notions of far field forcing of the Southern Ocean, we investigated what considerations would be required to understand the dynamics of how this would be achieved. We found the boundary conditions chosen have large impacts of the eddy dynamics of a channel model along side complications in TEM theory to understand the surface layer make this a complex problem. Here we have hinted at some of the processes that may be involved in altering the SO ROC in different climatic states, but more fundamentally we have shown the limitations of channel models when investigating idealised SO ROC theory.

When the northern boundary is closed the SO ROC upper cell, which can be thought of as an extension of the AMOC, disappears. In all cases when the northern boundary is closed the traditional 3 cell SO ROC ceases to exist, depending on the boundary condition we may see a diabatically driven surface cell such as seen in our surface restoring runs (Fig. 3.9), but this is distinct from the globally connected SO ROC. When diabatic forcing becomes stronger in the sponge layer, the upper cell in the SO gains amplitude and becomes comparable to the observed SO ROC (and AMOC). In this regime the diapycnal eddy heat flux divergence is always of first

order importance, counteracting the advective heat transport, leaving the surface heat forcing forcing as a smaller residual.

The vertical integral of the diapycnal eddy heat flux convergence decreases by an order of magnitude for weaker diabatic forcing in the sponge layer, although the eddy fluxes themselves increase by a factor of 2 to 3 between a closed basin and a configuration with strong restoring to a prescribed temperature stratification in the northern sponge layer. Using fixed fluxes these changes are reconciled by the establishment of a strong internal boundary layer with a large vertical temperature gradient. As a result, both heat transport divergence by a weak ROC confined to strong northward deepening mixed layer, and the diapycnal eddy heat flux divergence appear as dipoles of opposing signs due to our choice TEM definitions. For the diapycnal eddy fluxes heat convergence in the upper half of the internal boundary layer and heat divergence in the lower half occurs, while the heat transport divergence associated with the ROC in the mixed layer shows the opposite. Without diabatic forcing in a northern boundary sponge layer diabatic eddies cancel the effective surface buoyancy forcing, while the heat transport divergence by the ROC integrates to zero in the vertical. As a result, below the surface mixed layer the SO ROC completely collapses, because the connection to an adiabatic pole-to-pole circulation ceases to exist.

For fixed surface heat fluxes we have seen the SO ROC respond to changing northern boundary conditions via modulating the effective buoyancy forcing though diabatic eddies. Through out the thesis we have shown a selection of model runs performed particularly for the initial experiments varying the relaxation timescale. If we examine all the runs performed we can see a common factor between all these experiments, the northern boundary condition changes the background stratification. We can compare all these runs in terms of stratification by looking at Brunt Väisälä frequency N^2 . Here we plot the northern 100km integrated % increase in N^2 vs % decrease in domain integrated ROC strength for all experiments (varying stratification directly and indirectly though changing relaxation timescale). To see

the relationship we linearise the curve N^2 vs domain integrated SO ROC by taking the natural logarithm of the increase in N^2 and perform a linear regression to give a line of best fit shown in figure 6.1. Here we see an exponential decay with N^2 ¹. With fix surface fluxes it appears a very strong negative correlation with increased integrated N^2 and integrated SO ROC with R value of -0.95.

% decrease in ROC with increasing N^2

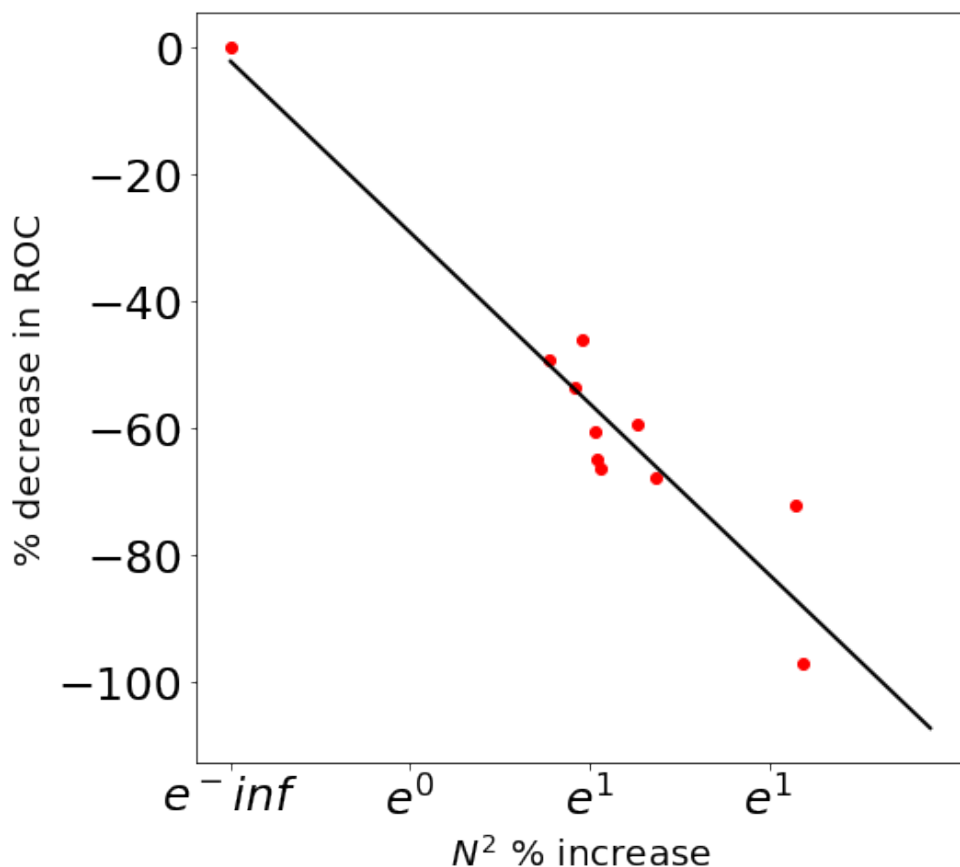


Figure 6.1: Linear regression line of best fit for % increase in integrated absolute ROC strength with natural logarithm of % increase in N^2 . $y = mx + c$, $m = -27$, $c = -2$, R value of -0.95 and a P value = 7×10^{-6} .

As we can see a clear trend of increasing integrated N^2 leading to decreasing integrated SO ROC and one of the major patterns we've seen with the collapsing SO ROC is increasing EKE that feeding into the increase of increased diabatic eddy heat fluxes. If we plot increase in domain integrated EKE that against increase

¹NB some models were never spun up and we do not have an even spread

in Northern Boundary integrated N^2 we see another strong correlation. Fig. 6.2 shows a 25 % increase in N^2 gives rise to a dramatic 400% increase in EKE.

% increase in EKE magnitude with increasing N^2

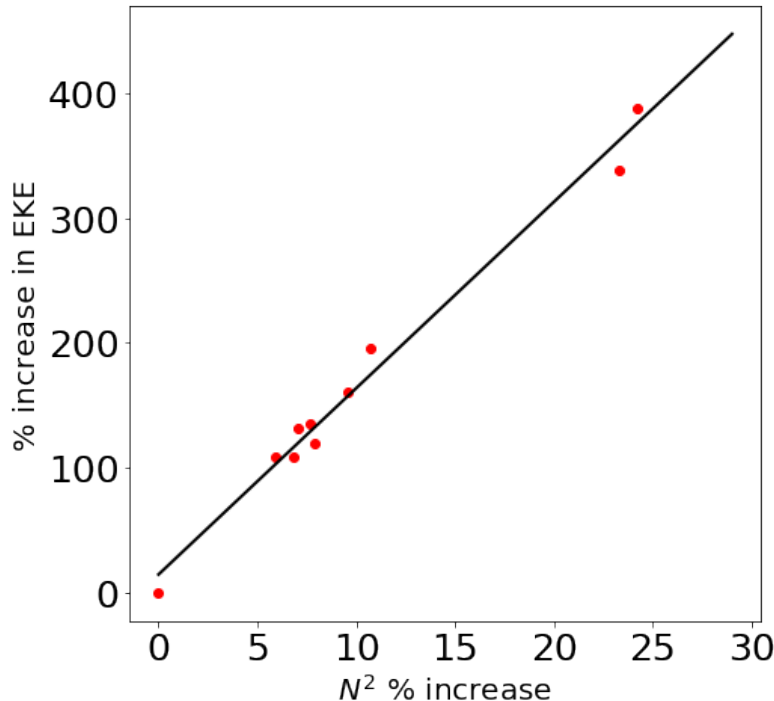


Figure 6.2: Linear regression line of best fit for % increase in EKE with % increase in N^2 . $y = mx + c$, $m = 15$, $c = 15$, $R = 0.99$, p value = 10^{-8}

This implies that the choice of northern boundary condition thus the alteration of domain background stratification influences the domain wide dynamics e.g. lower relaxation timescales or deeper thermocline lead to increased amounts of EKE and greater eddy compensation before altering the surface forcing.

6.1 The Surface Heat Forcing

Although we see that regardless of our choice in surface heat forcing we see a collapse in the SO ROC which can be weakly maintained even in absence of any surface heat forcing Fig. ?? by a the diabatic forcing of the sponge layer along. We see large changes in the dynamics when the surface heat forcing is surface

restoring, primarily in the surface mixed layer altering the diapycnal fluxes. When using a restoring boundary condition the main balance in the vertically integrated heat budget is somewhat different because no internal boundary layer develops and the northward deepening of the mixed layer is absent. The ROC is even more confined to the surface layer, and also in the case of a closed basin diabatic eddies and heat transport convergence by the ROC dominate the surface forcing. The role of the changing surface heat forcing mimics salinity driven (fixed fluxes) vs temperature driven (restoring) dynamics and this plays a role in setting the Southern Ocean dynamics in these differing regimes. For most of the worlds ocean buoyancy variations are dominated by temperature variations (variations in atmospheric temperature) most accurately represented by a restoring condition. The Southern Ocean, however, differs from this and is dominated by freshwater fluxes (?) which is more accurately represented by fixed-flux surface conditions² although in reality the ocean is like likely to be best represented through a mixture of these boundary conditions (*Stewart et al.*, 2014). The choice of surface heat forcing alters some fundamental dynamics of the Southern Ocean from the depth of the mixed layer (forcing a shallowing), isopycnal slope, EKE and domain wide stratification. From our results we can see the choice of correctly matching the surface restoring profile and the Northern boundary condition has very large implications on the dynamics as well. Using surface restoring versus fix-fluxes has been shown as large control on degree of eddy compensation in ocean models (*Gent*, 2015). Due to these factors we can not find any such promising relation between the Northern Boundary stratification and SO ROC strength or EKE strength as we could see in the fixed flux cases. This should serve as strong consideration when setting up channel models to investigate SO theory.

²Very poorly constrained, so fixed-flux is simply more adequate (*Jansen and Nadeau*, 2016)

6.2 Effects of Topography

When considering the the Southern Ocean it is important to consider the effects of topography as it affects the ACC generating stationary meanders ?, alters the distribution of EKE (*Thompson and Sallee*, 2012). We briefly ran some experiments to assess the possible implications of topography on the SO ROC response to altering the Northern boundary conditions. We see although the topography alters the distribution of EKE and alters some of the dynamics of the channel we still see the same 3 cell SO ROC collapsing when the northern boundary is closed only existing as an intense diabatically driven surface cell and like with the flat bottom fixed surface fluxes we see the generation of a deep mixed layer when the northern boundary is closed and a large increase in EKE associated with a diminished SO ROC. *Rosso et al.* (2015) suggests that the role of topography may be further underestimated as a forward cascade of energy may lead to large influences on submesocale scales influencing diabatic eddies in the mixed layer.

6.3 Summary and Future Work

The original motivation for this work was to investigate far field forcing of the Southern ocean, we showed in all cases for our channel model the upper cell SO ROC collapses when diabatic forcing in the northern sponge-layer is absent. These results underscore the interhemispheric link between the SO ROC and the northern hemisphere AMOC. Such links were previously demonstrated in *Gnanadesikan and Hallberg* (2000) and *Wolfe and Cessi* (2011). More fundamentally however these results showed the limitations and considerations required when setting up a regional model of the Southern Ocean. Here, by altering the northern boundary condition we showed how the SO ROC adjusts to changes in stratification at the northern end of the SO. It should be stressed that the representation of the far-field forcing, i.e. NADW formation, by a sponge layer with a prescribed e-folding strat-

ification is crude and should be tested against other ways of closing the SO ROC. Nevertheless, the absence of far-field forcing implies a disconnect between the SO ROC and the AMOC, and our results imply that in this case the upper cell of the SO ROC cannot be maintained. This result is independent of how the far field forcing is represented. What we do see is that the choice of northern boundary condition and surface forcing greatly alter the dynamics of the Southern Ocean from EKE to eddy saturation and ultimately how the collapse of the SO ROC is achieved is altered by the very sensitive set up of the channel model.

The crucial role of diabatic eddy heat fluxes in the adjustment process to such changes highlights the need for a carefully designed diabatic eddy representation in the surface mixed layer of the ocean, which should also depend on the atmospheric state and forcing. Our results also imply that diabatic eddy fluxes can be essential in closing the heat budget and that coarse resolution ocean (and hence climate) models that do not represent mesoscale eddies without parameterizing the diabatic eddy fluxes cannot adequately close the heat budget and simulate the response to changing heat fluxes. We chose here to evaluate to the diabatic eddy heat fluxes as the diapycnal heat flux divergence in the heat budget to account for the variation between runs altering the effectiveness of various approximations in the mixed layer. The diapycnal eddy heat flux divergence strongly responds to changes in the northern boundary condition, becoming larger (increasing by 250% in amplitude) when the stratification at the northern boundary is better able to freely evolve and is less constrained by the circulation and diabatic processes in the sponge layer. The resulting changes in diabatic forcing lead to a dramatic increase in surface mixed layer depth, which leads to enhanced baroclinic instability and larger EKE and EPE. This result is qualitatively robust to the surface boundary condition, but when surface restoring is applied instead of a flux formulation, a much smaller increase in diabatic fluxes occurs and the EKE is more constrained. Nevertheless, the role of diabatic eddy fluxes in the vertically integrated heat budget is equally large for both surface boundary conditions. It appears that the diabatic eddy heat

flux divergence is sensitive to both the strength of the surface heat flux and the diabatic forcing in the sponge layer, but also to the surface boundary condition for temperature (buoyancy).

Our channel model is very idealised, the next steps in understanding the role of diabatic eddies would involve the implementation of a more appropriate framework as well as perhaps moving to a less idealised set. The original theory we worked from uses buoyancy budgets not simply temperature alone to evaluate the SO ROC, in the cold temperatures of the Southern Ocean salinity plays a large role in setting the density of the ocean . Changing to a non linear Equation of state varying with Salinity and Temperature may lead to a more clear understanding of the role of surface forcing, with large discrepancies between fixed surface heat fluxes and surface restoring here suggesting differences between salinity driven and temperature driven changes, however the true surface forcing is likely to be a combinations. That leads us to the next improvement for future work, coupling to an atmosphere as these large changes in mixed layer heat flux divergence would have large implications for air-sea interactions that maybe better described by directly interacting with an atmosphere which would have a response to the changing conditions in the Southern Ocean creating feedbacks that may enhance the diabatic buoyancy forcing or dampen it. Alongside a coupled atmosphere we would also need to consider the role of sea ice on altering the surface buoyancy forcing with studies such as ? suggesting that sea ice can play a large role on the forcing of the Deep Ocean.

In chapter 5 we saw the effects of both the surface condition and the northern boundary condition had on eddy saturation suggesting closing the northern boundary reduced saturation as well as moving to a surface restoring boundary condition. The surface restoring is already known to have effects on setting the eddy saturation of a channel model, with stronger restoring giving stronger saturation (*Zhai and Munday, 2014*). Closing the northern boundary however increases eddy compensation and surface restoring reduces compensation. Mean models designed to

investigate the impact of wind forcing may have been strongly influenced by the model set up leading to the disparity in findings over the years.

In the introduction and in chapter 2 we introduced a the discussion of what parts of TEM theory from *Marshall and Radko* (2003) and the original *Andrews and McIntyre* (1976) is truly valid in the surface mixed which must be approached with approximations of varying limitations (*Plumb and Ferrari*, 2005). Part of the limitation is that we calculate the residual overturning stream function as an isopycnal streamfunction which deviates from the real residual streamfunction the most in the surface layers, this deviation is reduced by increasing the number of temperature layers the stream function is calculated over, however this is very computationally expensive. In atmospheric sciences *Pauluis et al.* (2011) developed a statistical transformed Eulerian mean (STEM) which when applied to the ocean does not break down at the surface (*Wolfe*, 2014). STEM assumes that velocity and tracer fields can be represented by random processes possessing the same moments as the modelled field, this also makes for easier implementation which in light of the requirements for future development of TEM theory requiring more realistic set ups to fully understand the dynamics could be a tool to do so in a less computationally demanding manner.

There is still a lot more we need to understand about the Southern Ocean dynamics to fully comprehend all the feedbacks that may determine the SO ROC response to altered climates. The theory we have discussed here about the role diabatic eddies might play in that in turn high lighted the challenges in setting up experiments to test Southern Ocean theory as we demonstrate how the boundary conditions and forcing chosen may affect the SO ROC and eddy dynamics before even beginning to alter a chosen parameter.

type=symbolslist

Acronyms

AABW Antarctic Bottom Water.

AAIW Antarctic Intermediate Water.

ACC Antarctic Circumpolar Current.

AMOC Atlantic Meridional Overturning Circulation.

AOGCM Atmosphere-Ocean Coupled Global Climate Model.

CDW Circumpolar Deep Water.

CFL CourantFriedrichsLewy.

EKE Eddy Kinetic Energy.

EKE Eddy Potential Energy.

Fortran Formula Translating System.

GCM General Circulation Model.

GPE Gravitational Potential Energy.

GS Gulf Stream.

ITCZ Inter Tropical Convergence Zone.

KE Kinetic Energy.

KPP K-profile parameterization.

LCDW Lower Circumpolar Deep Water.

LHS Left Hand Side.

MITgcm Massachusetts Institute of Technology General Circulation Model.

MOC Meridional Overturning Circulation.

NADW North Atlantic Deep Water.

NCEPNCAR National Centers for Environmental Prediction-National Centre for Atmospheric Research.

NERC Natural Environment Research Council.

netCDF Network Common Data Form.

NOC National Oceanography Centre.

PF Polar Front.

POP Parallel Ocean Programme.

PV Potential Vorticity.

QG Quasi-Geostrophic.

RHS Right Hand Side.

RMOC Residual Meridional Overturning Circulation.

ROC Residual Overturning Circulation.

SAF Southern Antarctic Front.

SAM Southern Annular Mode.

SAMW Sub Antarctic Mode Water.

SOMOC Southern Ocean Meridional Overturning Circulation.

SOROC Southern Ocean Residual Overturning Circulation.

SSH Sea Surface Height.

SSHA Sea Surface Height Anomaly.

SSSA Sea Surface Salinity Anomaly.

SST Sea Surface Temperature.

SSTA Sea Surface Temperature Anomaly.

STF Subtropical Front.

TEM Transformed Eulerian Mean.

TIW Tropical Instability Wave.

TKE Turbulent Kinetic Energy.

TNA Tropical North Atlantic.

U Zonal Velocity in m/s.

UCDW Upper Circumpolar Deep Water.

V Meridional Velocity in m/s.

Symbolslist

| Symbol | Description | Unit |
|----------|--|--------------------------------|
| C_p | Specific heat capacity. (Sea water = 3985 $\text{JKg}^{-1}\text{K}^{-1}$) | $\text{JKg}^{-1}\text{K}^{-1}$ |
| D | Material derivative | |
| Ek | Ekman number | |
| F | Function (variables) | |
| J | Jacobian | |
| K | Eddy transfer coefficient | |
| L | Length | m |
| N^2 | Brunt Väisälä frequency | |
| P_b | Bottom Pressure | N/m^2 |
| Q | Heat Flux | w/m^2 |
| Ro | Rossby number | |
| S_p | Isopycnal slope | |
| Ω | | |
| Φ | | |
| Ψ | Stream function | m^3/s |
| β | Coriolis ratio | |
| χ | | |
| η_b | Sea Surface Height | m |
| η | Bottom topography | m |

| Symbol | Description | Unit |
|------------------------|--|-------------------|
| κ | Eddy diffusivity constant | |
| \mathcal{B} | buoyancy forcing | |
| \mathcal{G} | Green's function ? | |
| $\nabla \times \tau_s$ | Wind Stress Curl | |
| π | Geometrical value | |
| ρ | Density, ₀ denotes reference density. | kg/m ² |
| τ_s | Wind Stress | |
| θ | Potential temperature | ° C |
| a | denotes ageostrophic | |
| b | buoyancy | |
| f | coriolis frequency | |
| hml | Mixed layer Depth | m |
| q | vorticity | |
| \mathbf{u} | Velocity vector (x,y,z,t), $u =$ zonal, $v =$ meridional, $w =$ vertical | m/s |

Glossary

adiabatic .

baroclinic .

Barotropic .

Brunt Väisälä frequency Largest temporal frequency that internal waves can have.

Diabatic .

e-folding A factor of $1/e$, space scale for change of $1/e$ if exponential decay is assumed.

geostrophic .

Incompressibility incompressibility.

Isotherm Surface of equal temperature.

ψ Stream function (m^2s^{-1}).

ψ_{res} Residual overturning stream function (m^2s^{-1}).

psu The Practical Salinity Scale defines salinity in terms of the conductivity ratio of a sample to that of a solution of 32.4356 g of KCl at 15°C in a 1 kg solution. A sample of seawater at 15°C with a conductivity equal to this KCl solution has a salinity of exactly 35 practical salinity units (psu).

ρ Density of sea water (1030 kg m^{-3}).

Rossby radius The scale for mesoscale eddies to form baroclinic instability. $L_d = \frac{NH}{f}$, where N is the buoyancy frequency, H is thickness and f is the coriolis frequency..

Southern Ocean Region of ocean around Antarctica, although not defined as a subregion of the world ocean by the International Hydrographic Organization, it represents a region of differing dynamics separate from the Atlantic, Pacific and Indian oceans (*Tomczak and Godfrey, 2003*)..

Sverdrups 10^6 m/s^2 .

Bibliography

- Abernathay, R., and P. Cessi, Topographic Enhancement of Eddy Efficiency in Baroclinic Equilibration, *J. Phys. Ocean.*, 44(8), 2107–2126, 2014.
- Abernathay, R., J. Marshall, and D. Ferreira, The Dependence of Southern Ocean Meridional Overturning on Wind Stress, *J. Phys. Oceanogr.*, 41(12), 2261–2278, 2011.
- Abernathay, R., D. Ferreira, and A. Klocker, Diagnostics of isopycnal mixing in a circumpolar channel, *Ocean Model.*, 72, 1–16, 2013.
- Adcroft, A. J., C. Hill, and J. Marshall, Representation of Topography by Shaved Cells in a Height Coordinate Ocean Model, *Mon. Weather Rev.*, 125(9), 2293–2315, 1997.
- Adcroft, A. J., C. Hill, J. M. Campin, J. Marshall, and P. Heimbach, Overview of the Formulation and Numerics of the MIT GCM, *Proc. ECMWF Semin. Ser. Numer. Methods Recent Dev. Numer. methods Atmos. Ocean Model.*, pp. 139–149, 2004.
- Allison, L. C., H. L. Johnson, D. P. Marshall, and D. R. Munday, Where do winds drive the antarctic circumpolar current?, *Geophys. Res. Lett.*, 37(12), 1–5, 2010.
- Andrews, D. G., and M. E. McIntyre, Planetary Waves in Horizontal and Vertical Shear: The Generalized Eliassen-Palm Relation and the Mean Zonal Acceleration, 1976.
- Boccaletti, G., R. Ferrari, and B. Fox-Kemper, Mixed Layer Instabilities and Re-stratification, *J. Phys. Oceanogr.*, 37, 2228–2250, 2007.
- Böning, C. W., A. Dispert, M. Visbeck, S. R. Rintoul, and F. U. Schwarzkopf, The response of the Antarctic Circumpolar Current to recent climate change, *Nat. Geosci.*, 1(12), 864–869, 2008.
- Campin, J. M., A. Adcroft, C. Hill, and J. Marshall, Conservation of properties in a free-surface model, *Ocean Model.*, 6(3-4), 221–244, 2004.
- Cerovečki, I., R. A. Plumb, and W. Heres, Eddy transport and mixing in a wind- and buoyancy-driven jet on the sphere, *J. Phys. Oceanogr.*, 39(5), 1133–1149, 2009.

- Cerovečki, I., L. D. Talley, and M. R. Mazloff, A comparison of southern ocean air-sea buoyancy flux from an ocean state estimate with five other products, *J. Clim.*, 24(24), 6283–6306, 2011.
- Cessi, P., W. R. Young, and J. A. J. Polton, Control of large-scale heat transport by small-scale mixing, *J. Phys. Oceanogr.*, 36(10), 1877–1894, 2006.
- Chang, J., et al., *Methods in computational physics. Vol._17: General circulation models of the atmosphere.*, 1977.
- Collins, S. N., R. S. James, P. Ray, K. Chen, A. Lassman, and J. Brownlee, Grids in Numerical Weather and Climate Models, in *Clim. Chang. Reg. Responses*, edited by Y. Zhang and P. Ray, chap. 04, InTech, Rijeka, 2013.
- Cox, M., and K. Bryan, A numerical model of the ventilated thermocline, 1984.
- Daru, V., and C. Tenaud, High order one-step monotonicity-preserving schemes for unsteady compressible flow calculations, *J. Comput. Phys.*, 193, 563–594, 2004.
- de Szoeke, R. A., and M. D. Levine, The advective flux of heat by mean geostrophic motions in the Southern Ocean, *Deep Sea Res. Part A. Oceanogr. Res. Pap.*, 28(10), 1057–1085, 1981.
- Döös, K., and D. Webb, The Deacon cell and the other meridional cells of the Southern Ocean, *J. Phys. Oceanogr.*, 1994.
- Farneti, R., and T. L. Delworth, The role of mesoscale eddies in the remote oceanic response to altered Southern Hemisphere winds, *J. Phys. Oceanogr.*, 40(10), 2348–2354, 2010.
- Ferreira, D., J. Marshall, and P. Heimbach, Estimating Eddy Stresses by Fitting Dynamics to Observations Using a Residual-Mean Ocean Circulation Model and Its Adjoint, *J. Phys. Oceanogr.*, 35, 1891–1910, 2005.
- Ferreira, D., J. Marshall, C. M. Bitz, S. Solomon, and A. Plumb, Antarctic ocean and sea ice response to ozone depletion: A two-time-scale problem, *J. Clim.*, 28(3), 1206–1226, 2015.
- Gaspar, P., Y. Grégoris, and J. Lefevre, A simple eddy kinetic energy model for simulations of the oceanic vertical mixing., *J. Geophys. Res.*, 95(C9), 179–193, 1990.
- Gent, P. R., The Gent-McWilliams parameterization: 20/20 hindsight, *Ocean Model.*, 39(1-2), 2–9, 2011.
- Gent, P. R., Effects of Southern Hemisphere Wind Changes on the Meridional Overturning Circulation in Ocean Models, *Ann. Rev Mar Sci.*, pp. 1–34, 2015.
- Gill, A., Atmospheric-ocean dynamics, *Int. Geophys. Ser.*, 30, 662, 1982.
- Gill, A., J. Green, and A. Simmons, Energy partition in the large-scale ocean circulation and the production of mid-ocean eddies, *Deep Sea Res. Part A. Oceanogr. Res. Pap.*, 21, 499–528, 1974.

- Gnanadesikan, a., A Simple Predictive Model for the Structure of the Oceanic Pycnocline, *Science* (80-.), 283(5410), 2077–2079, 1999.
- Gnanadesikan, A., and R. W. Hallberg, On the Relationship of the Circumpolar Current to Southern Hemisphere Winds in Coarse-Resolution Ocean Models, *J. Phys. Oceanogr.*, 30, 2013–2034, 2000.
- Griffies, S. M., C. W. Böning, F. O. Bryan, E. P. Chassignet, R. Gerdes, H. Hasumi, A. Hirst, A.-M. Tréguier, and D. Webb, Developments in ocean climate modeling, *Ocean Model.*, 2(3), 123–192, 2000.
- Hallberg, R. W., and A. Gnanadesikan, The role of eddies in determining the structure and response of the wind-driven Southern Hemisphere overturning: Results from the Modeling Eddies in the Southern Ocean (MESO) project, *J. Phys. Oceanogr.*, 36(12), 2232–2252, 2006.
- Haney, R. L., Surface Thermal Boundary Condition for Ocean Circulation Models, 1971.
- Hausmann, U., A. Czaja, and J. Marshall, Estimates of air-sea feedbacks on sea surface temperature anomalies in the Southern Ocean, *J. Clim.*, 29(2), 439–454, 2016.
- Held, I. M., and T. Schneider, The Surface Branch of the Zonally Averaged Mass Transport Circulation in the Troposphere, *J. Atmos. Sci.*, 56(11), 1688–1697, 1999.
- Hidaka, K., and M. Tsuchiya, On the antarctic circumpolar current, *J. Mar. Res.*, 12(2), 214, 1953.
- Hill, C., D. Ferreira, J.-M. Campin, J. Marshall, R. Abernathey, and N. Barrier, Controlling spurious diapycnal mixing in eddy-resolving height-coordinate ocean models—Insights from virtual deliberate tracer release experiments, *Ocean Model.*, 45, 14–26, 2012.
- Hogg, A. M., An Antarctic Circumpolar Current driven by surface buoyancy forcing, *Geophys. Res. Lett.*, 37(23), 2010.
- Hogg, A. M., M. P. Meredith, D. P. Chambers, E. P. Abrahamsen, C. W. Hughes, and A. K. Morrison, Recent trends in the Southern Ocean eddy field, *J. Geophys. Res. C Ocean.*, 120(1), 257–267, 2015.
- Ilcak, M., A. J. Adcroft, S. M. Griffies, and R. W. Hallberg, Spurious dianeutral mixing and the role of momentum closure, *Ocean Model.*, 4546, 37–58, 2012.
- Jansen, M. F., and L.-P. Nadeau, The Effect of Southern Ocean Surface Buoyancy Loss on the Deep Ocean Circulation and Stratification, *J. Phys. Oceanogr.*, pp. JPO-D-16-0084.1, 2016.
- Jansen, M. F., A. J. Adcroft, R. Hallberg, and I. M. Held, Parameterization of eddy fluxes based on a mesoscale energy budget, *Ocean Model.*, 92, 28–41, 2015.

- Johnson, G. C., and H. L. Bryden, On the size of the Antarctic Circumpolar Current, *Deep Sea Res. Part A. Oceanogr. Res. Pap.*, 36(1), 39–53, 1989.
- Karsten, R., H. Jones, and J. Marshall, The role of eddy transfer in setting the stratification and transport of a circumpolar current, *J. Phys. Oceanogr.*, 32(1), 39–54, 2002.
- Kazantsev, E., Optimal boundary conditions for ORCA-2 model, *Ocean Dyn.*, 63(8), 943–959, 2013.
- Kuo, A., R. A. Plumb, and J. Marshall, Transformed Eulerian-mean theory. Part II: Potential vorticity homogenization and the equilibrium of a wind-and buoyancy-driven zonal flow, *J. Phys. Oceanogr.*, 35(2), 175–187, 2005.
- Large, W. G., and S. G. Yeager, The global climatology of an interannually varying air - Sea flux data set, *Clim. Dyn.*, 33(2-3), 341–364, 2009.
- Large, W. G., J. C. Mcwilliams, and S. C. Doney, Oceanic Vertical Mixing - a Review and a Model with a Nonlocal Boundary-Layer Parameterization, *Rev. Geophys.*, 32(94), 363–403, 1994.
- Le Quéré, C., et al., Saturation of the Southern Ocean CO₂ sink due to recent climate change, *Science (80-.)*, 316(5832), 1735–1738, 2007.
- Legg, S., and J. C. McWilliams, Convective Modifications of a Geostrophic Eddy Field*, *J. Phys. Oceanogr.*, 31(4), 874–891, 2001.
- Lorenz, E. N., Energy and numerical weather prediction, *Tellus*, 12(4), 364–373, 1960.
- Madec, G., and P. Delecluse, Institut Pierre Simon Laplace Ocean General Circulation Model Reference Manual, *Tech. rep.*, 1998.
- Marshall, D. P., Subduction of water masses in an eddying ocean, *J. Mar. Res.*, 55(2), 201–222, 1997.
- Marshall, J., and T. Radko, Residual-mean solutions for the Antarctic Circumpolar Current and its associated overturning circulation, *J. Phys. Oceanogr.*, 33(11), 2341–2354, 2003.
- Marshall, J., and K. Speer, Closure of the meridional overturning circulation through Southern Ocean upwelling, *Nat. Geosci.*, 5, 171–180, 2012.
- Marshall, J., C. Hill, L. Perelman, and A. J. Adcroft, Hydrostatic, quasi-hydrostatic, and nonhydrostatic ocean modeling, *J. Geophys. Res. Ocean.*, 102(C3), 5733–5752, 1997.
- McWilliams, J. C., and G. Danabasoglu, Eulerian and Eddy-Induced Meridional Overturning Circulations in the Tropics, *J. Phys. Oceanogr.*, 32, 2054–2071, 2002.
- Meredith, M. P., and A. M. Hogg, Circumpolar response of Southern Ocean eddy activity to a change in the Southern Annular Mode, *Geophys. Res. Lett.*, 33(16), 2006.

- Meredith, M. P., A. C. Naveira Garabato, A. M. Hogg, and R. Farneti, Sensitivity of the overturning circulation in the Southern Ocean to decadal changes in wind forcing, *J. Clim.*, 25(1), 99–110, 2012.
- Mignone, B. K., A. Gnanadesikan, J. L. Sarmiento, and R. D. Slater, Central role of Southern Hemisphere winds and eddies in modulating the oceanic uptake of anthropogenic carbon, *Geophys. Res. Lett.*, 33(1), 2006.
- Moore, GWK and Renfrew, I., An Assessment of the Surface Turbulent Heat Fluxes from the NCEP NCAR Reanalysis over the Western Boundary Currents, *J. Clim.*, pp. 2020–2037, 2002.
- Morrison, A. K., and A. McC. Hogg, On the relationship between Southern Ocean overturning and ACC transport, *J. Phys. Oceanogr.*, 43(1), 140–148, 2013.
- Munk, W. H., and E. Palmén, Note on the Dynamics of the Antarctic Circumpolar Current1, *Tellus*, 3(1), 53–55, 1951.
- Nikurashin, M., and G. Vallis, A Theory of the Interhemispheric Meridional Overturning Circulation and Associated Stratification, *J. Phys. Oceanogr.*, 42, 1652–1667, 2012.
- Pauluis, O., T. Shaw, and F. Laliberté, A Statistical Generalization of the Transformed Eulerian-Mean Circulation for an Arbitrary Vertical Coordinate System, *J. Atmos. Sci.*, 68(8), 1766–1783, 2011.
- Plumb, R., and R. Ferrari, Transformed Eulerian-mean theory. Part I: Non-quasigeostrophic theory for eddies on a zonal-mean flow, *J. Phys. Oceanogr.*, pp. 165–174, 2005.
- Rintoul, S. R., et al., *The Southern Ocean observing system: initial science and implementation strategy*, Scientific Committee on Antarctic Research, 2012.
- Rosso, I., A. M. Hogg, A. E. Kiss, and B. Gayen, Topographic influence on submeso-scale dynamics in the Southern Ocean, *Geophys. Res. Lett.*, 42, 1139–1147, 2015.
- Saenz, J. A., A. M. Hogg, G. O. Hughes, and R. W. Griffiths, Mechanical power input from buoyancy and wind to the circulation in an ocean model, *Geophys. Res. Lett.*, 39(13), 2012.
- Sallée, J.-B., K. Speer, S. Rintoul, and S. Wijffels, Southern Ocean Thermocline Ventilation, *J. Phys. Oceanogr.*, 40, 509–529, 2010.
- Shakespeare, C. J., and A. Hogg, An analytical model of the response of the meridional overturning circulation to changes in wind and buoyancy forcing, *J. Phys. Oceanogr.*, 42(8), 1270–1287, 2012.
- Speer, K., S. R. Rintoul, and B. Sloyan, The Diabatic Deacon Cell*, *J. Phys. Oceanogr.*, 30(12), 3212–3222, 2000.
- Stewart, A. L., R. Ferrari, and A. F. Thompson, On the Importance of Surface Forcing in Conceptual Models of the Deep Ocean, *J. Phys. Oceanogr.*, 44(3), 891–899, 2014.

- Thompson, A. F., and J.-B. Sallee, Jets and topography: jet transitions and the impact on transport in the Antarctic Circumpolar Current, *J. Phys. Oceanogr.*, 42, 956–972, 2012.
- Thompson, D. W. J., and S. Solomon, Interpretation of recent Southern Hemisphere climate change, *Science (80-.).*, 296(5569), 895–899, 2002.
- Toggweiler, J. R., and J. L. Russell, Ocean circulation in a warming climate., *Nature*, 451(17), 286–288, 2008.
- Tomczak, M., and J. S. Godfrey, The Atlantic Ocean, *Reg. Oceanogr. an Introd.*, pp. 229–252, 2003.
- Tréguier, A.-M., I. M. Held, and V. D. Larichev, Parameterization of quasigeostrophic eddies in primitive equation ocean models, *J. Phys. Oceanogr.*, 27(4), 567–580, 1997.
- Tréguier, A.-M., M. H. England, S. R. Rintoul, G. Madec, J. Le Sommer, J.-M. Molines, and Others, Southern Ocean overturning across streamlines in an eddying simulation of the Antarctic Circumpolar Current, *Ocean Sci. Discuss.*, 4(4), 653–698, 2007.
- Viebahn, J., and C. Eden, Standing eddies in the meridional overturning circulation, *J. Phys. Oceanogr.*, 42(9), 1486–1508, 2012.
- Visbeck, M., J. Marshall, T. Haine, and M. Spall, Specification of Eddy Transfer Coefficients in Coarse-Resolution Ocean Circulation Models*, *J. Phys. Oceanogr.*, 27(3), 381–402, 1997.
- von Storch, J.-S., C. Eden, I. Fast, H. Haak, D. Hernández-Deckers, E. Maier-Reimer, J. Marotzke, and D. Stammer, An estimate of Lorenz energy cycle for the world ocean based on the 1/10 degree STORM/NCEP simulation, *J. Phys. Oceanogr.*, 42(1992), 120821111920,009, 2012.
- Whitworth, T., and R. G. Peterson, Volume transport of the Antarctic Circumpolar Current from bottom pressure measurements, *J. Phys. Oceanogr.*, 15(6), 810–816, 1985.
- Wolfe, C. L., Approximations to the ocean’s residual circulation in arbitrary tracer coordinates, *Ocean Model.*, 75(0), 20–35, 2014.
- Wolfe, C. L., and P. Cessi, Overturning circulation in an eddy-resolving model: The effect of the pole-to-pole temperature gradient, *J. Phys. Oceanogr.*, 39, 125–142, 2009.
- Wolfe, C. L., and P. Cessi, The adiabatic pole-to-pole overturning circulation, *J. Phys. Oceanogr.*, pp. 1795–1810, 2011.
- Wolfe, C. L., P. Cessi, J. L. McClean, and M. E. Maltrud, Vertical heat transport in eddying ocean models, *Geophys. Res. Lett.*, 35(23), L23,605, 2008.
- Wunsch, C., and R. Ferrari, Vertical Mixing, Energy, and the General Circulation of the Oceans, *Annu. Rev. Fluid Mech.*, 36(1), 281–314, 2004.

- Zhai, X., and D. R. Munday, Sensitivity of Southern Ocean overturning to wind stress changes: Role of surface restoring time scales, *Ocean Model.*, 84, 12–25, 2014.

Appendices

A Advection assumptions on model grid

Here we demonstrate, by using a one dimensional example of Eq. 2.7, that this equation is not valid on the model grid. In our model runs, we used the MITgcm advection scheme 7 (*Daru and Tenaud*, 2004) with modifications from Adcroft and Campin, (MITgcm support mailing list communications 2010). This is a one step monotonicity-preserving 7th order scheme. Referring to *Adcroft et al.* (2004) and MITgcm model code (*Marshall*, 1997), for a 1-D advection problem in the y-direction for a tracer Q the discrete fluxes become:

$$\begin{aligned} \frac{\partial Q}{\partial t} + v \frac{\partial Q}{\partial y} = & \\ & \frac{1}{\Delta t} (Q_j^{n+1} - Q_j^n) + \frac{v}{\Delta y} \left(Q_j^n + \frac{1}{2}(1-C)(Q_{j+1}^n - Q_j^n) - \right. \\ & \frac{1}{6}(1-C^2)(Q_{j+1}^n - 2Q_j^n + Q_{j-1}^n) - Q_{j-1}^n - \\ & \frac{1}{2}(1-C)(Q_j^n - Q_{j-1}^n) + \\ & \left. \frac{1}{6}(1-C^2)(Q_j^n - 2Q_{-j}^n + Q_{j-2}^n) \right) + O^4 \end{aligned} \quad (1)$$

where C is the Courant number $\left(\frac{u\Delta t}{\Delta x}\right)$. Monotonicity-preserving flux limiters not described here are also applied. This 1-D treatment can be generalized to 3-D by removing the local divergence flow separately in each dimension. Using the identity:

$$v \frac{\partial Q}{\partial y} = \frac{\partial v Q}{\partial y} - Q \frac{\partial v}{\partial y}, \quad (2)$$

and applying Eq. 2 on a C-grid (Fig. 1.4) we can demonstrate Eq. 2.7 does not hold on the model grid.

$$\begin{aligned}
& \frac{\partial Q}{\partial t} + v \frac{\partial Q}{\partial y} + = \\
& \frac{1}{\Delta t} (Q_j^{n+1} - Q_j^n) + \frac{\left(\frac{v_{j-\frac{1}{2}} + v_{j+\frac{1}{2}}}{2} \right)}{\Delta y} (Q_j^n + \\
& \frac{1}{2}(1-C)(Q_{j+1}^n Q_j^n) - \frac{1}{6}(1-C^2)Q_{j+1}^n - \\
& 2Q_j^n + Q_{j-1}^n) - Q_{j-1}^n - \frac{1}{2}(1-C)(Q_j^n - \\
& Q_{j-1}^n) + \frac{1}{6}(1-C^2)(Q_j^n - 2Q_{j-1}^n + \\
& Q_{j-2}^n) + O^4
\end{aligned} \tag{3}$$

whereas, when velocity is taken back inside the divergence term:

$$\begin{aligned}
& \frac{\partial vQ}{\partial t} + \frac{\partial vQ}{\partial y} + = \\
& \frac{1}{\Delta t} \left(\left(v_{j-\frac{1}{2}} \left(\frac{Q_j + Q_{j-1}}{2} \right) \right)^{n+1} - \left(v_{j-\frac{1}{2}} \left(\frac{Q_j + Q_{j-1}}{2} \right) \right)^n \right) + \\
& \frac{1}{\Delta y} \left(\left(\frac{Q_j + Q_{j-1}}{2} \right) v_{j-\frac{1}{2}}^n + \right. \\
& \frac{1}{2}(1-C) \left(\left(\frac{Q_j + Q_{j+1}}{2} \right) v_{j+\frac{1}{2}}^n - \right. \\
& \left. \left(\frac{Q_j + Q_{j-1}}{2} \right) v_{j-\frac{1}{2}}^n \right) - \frac{1}{6}(1-C^2) \left(\frac{Q_j + Q_{j+1}}{2} \right) v_{j+\frac{1}{2}}^n - \\
& 2 \left(\frac{Q_j + Q_{j-1}}{2} \right) v_{j-\frac{1}{2}}^n + \left(\frac{Q_{j-1} + Q_{j-2}}{2} \right) v_{j-\frac{3}{2}}^n - \\
& \left. \left(\frac{Q_{j-1} + Q_{j-2}}{2} \right) v_{j-\frac{3}{2}}^n - \frac{1}{2}(1-C) \left(\left(\frac{Q_j + Q_{j-1}}{2} \right) v_{j-\frac{1}{2}}^n - \right. \right. \\
& \left. \left(v_{j-\frac{3}{2}}^n \right) + \frac{1}{6}(1-C^2) \left(\left(\frac{Q_j + Q_{j-1}}{2} \right) v_{j-\frac{1}{2}}^n - 2 \left(\frac{Q_{j-1} + Q_{j-2}}{2} \right) v_{j-\frac{3}{2}}^n + \right. \right. \\
& \left. \left. \left(\frac{Q_{j-2} + Q_{j-3}}{2} \right) v_{j-\frac{5}{2}}^n \right) + O^4
\end{aligned} \tag{4}$$

One can see by comparing Eq. 3 and Eq. 4 that they are not equivalent. Terms of 2nd and higher order differ, indicating Eq. 2.7 can not be used when evaluating discretized numerical models.

B Eaxmple datafile

To give a full overview of the parameters used in the standard model set up below is an example data input file with the run time model flags and in italics a brief explanation.

& PARM01

tRef=Reference Profile, *This the reference temperature used in things like linear EOS, set as the sponge profile*

viscosity

viscAh=12.000000, *Laplacian viscosity coefficient (m^2/s) Set so that horizontal Reynolds number is 0, this scales with resolution of one less than the order (so linearly here) - basically it is to ensure that the velocity is not too fast that a wave can pass through a cell in less than one time step with the scaling relation $A_h < \frac{L^2}{4\Delta t}$ (Courant-Freidrichs-Lowy Constraint on viscosity). Griffies et al. (2000) notes that it actually scales to one less power.*

viscAz=0.000300, *vertical eddy coefficient. default*

viscA4=9.0E8, *Bi-harmonic viscosity coefficient (m^4/s) With the relation $A_4 <= \frac{L^4}{32\Delta t}$. Allows a less viscous yet numerically stable simulation than harmonic (laplacian) as eddy viscosities can be focuses on the dynamics at the grid scale as large motions would be 'resolved'.*

viscA4GridMax=0.500 *Maximum grid dependent biharmonic viscosity*

viscAhGridMax=0.500 *Maximum lateral grid dependent eddy viscosity*

Diffusion

diffKhT=0.000000, *Laplacian diffusion of heat laterally (m^2/s) the boundary condition on this operator is $\frac{\partial}{\partial x} = \frac{\partial}{\partial y} = 0$ on all boundaries. Default.*

diffKzT=0.000000, *Laplacian diffusion of salt vertically can be set implicitly by setting implicitDiffusion to .TRUE. Default.*

diffKhS=0.000000, *Laplacian diffusion of salt laterally (m^2/s) same applies as for T. Default.*

diffKzS=0.000000, *Laplacian diffusion of salt vertically (m^2/s) same applies as for S. Default.*

Advection Scheme

tempAdvScheme=7, *The seventh-order one-step method with monotonicit-preserving limiter (OS7MP) (Daru and Tenaud, 2004) and minimises numerical diffusion (Ilcak et al., 2012; Shakespeare and Hogg, 2012)*

Timestepping

StaggerTimeStep=.TRUE., *The stagger baroclinic time stepping rather than synchronous time stepping. The thermodynamics solver is delayed from half a time step, allowing the use of the most recent velocities to compute the advection terms*

saltStepping=.FALSE., *Salinity equation off.*

equation of state

eosType='LINEAR', *Sets linear EOS, buoyancyRelation is automatically set to OCEANIC. For the nonlinear case, you need to generate a le of polynomial coefficients called POLY3.COEFFS. To do this, use the program utils/knudsen2/knudsen2.f instead of tAlpha and sBeta*

tAlpha=2.0E-4, *thermal expansion coefficient in K⁻¹ for EOS. Default.*

sBeta =0., *salt is passive here (ppt⁻¹)*

Boundary conditions

no_slip_sides=.TRUE., *Free slip or no slip. Free slip give zero stress on boundaries (more convenient to code). No slip defines the normal gradient of a tangential flow such that the flow is zero on the boundary by adding an additional source term in cells next to the boundary*

no_slip_bottom=.TRUE.,

bottomDragLinear=1.1E-03, *linear bottom-drag coefficient (m/s)*

bottomDragQuadratic=0.000000E+00, *quadratic bottom-drag coeff. Default.*

physical parameters

f0=-1.E-4, *Coriolis parameter (s⁻¹), f = 2ωsinφ Here this is set to the negative reference value and as beta is non zero f0 is the value of f at the southern edge of the domain.*

beta=1E-11, $\frac{\partial f}{\partial y}$ (m⁻¹s⁻¹)

gravity=9.81,

exact volume conservation

exactConserv=.TRUE.,

C-V scheme for Coriolis term

useCDscheme=.FALSE.,

partial cells for smooth topography

HfacMin=0.05, *Limit partial cells to 50m thickness*

file I/O parameters

```

readBinaryPrec=64,double precision

useSingleCpuIO=.TRUE.,

debugLevel=1,

# Default surface conditions

rigidLid=.FALSE.,

implicitFreeSurface=.TRUE.,these lines suppress the rigid lid formulation of
the surface pressure inverter and activate the implicit free surface form of the pres-
sure inverter.

&

& PARM02

cg2dMaxIters=500,Upper limit on 2d con. grad iterations, default is 150.

cg2dTTargetResidual=1.E-9, default is 1.E-7

cg3dMaxIters=40,Sets the maximum number of iterations the three-dimensional,
conjugate gradient solver

cg3dTTargetResidual=1.E-9,

&

& PARM03

deltaT=450,time steps scales with resolution

# 7.5 minute time step -> 69120 time steps/year

nIter0=0,Start at..

nTimeSteps=1382400,20 years

cAdjFreq = -1.,Convective adjustment interval (s), the frequency at which the
adjustment algorithm is called to a non-zero value, a negative value sets to tracer
time step

abEps=0.1,Adams-Bashforth stabilizing parameter, required as staggerTimeStep
is set to TRUE

# Permanent restart/checkpoint file interval ( s )

# Try 10 year interval (two per run)

pChkptFreq=311040000.00,Checkpoint file interval (s)

dumpFreq=0.0,Model state write out interval (s)

monitorFreq=0.0,Monitor output interval (s)

```

dumpInitAndLast=.TRUE.,

pickupStrictlyMatch=.FALSE.,

&

& PARM04

usingCartesianGrid=.TRUE., *Uses cartesian co-ordinate system with uniform grid space via dXspacing or dYspacing or by vectors DelX or DelY in (m)*

usingSphericalPolarGrid=.FALSE.,

delXfile='delX', *Can be set as a 1D array file or as gridlines * spacing i.e 300*5E3 300 grid lines at 5km spacing*

delYfile='delY',

delZfile='delZ'

&

& PARM05

surfQfile='Qsurface'

bathyFile='topog'

zonalWindFile='Wind',

meridWindFile=,

hydrogThetaFile='T.init',

&